



Optical Interconnects For Trapped-Ion Quantum Transmitters

By
Mojtaba Ghadimi

Master of Science in Physics

SUBMITTED IN FULFILMENT OF
THE REQUIREMENTS OF THE DEGREE OF
DOCTOR OF PHILOSOPHY

Principal Supervisor:

Dr. Mirko Lobino

Dr. Erik W. Streed

Associate Supervisor:

Prof. David Kielpinski

School of Natural Sciences,
Griffith University,
Australia.

September 11, 2016

© Copyright 2017
by
Mojtaba Ghadimi

This work has not previously been submitted for a degree or diploma in any university. To the best of my knowledge and belief, the thesis contains no material previously published or written by another person except where due reference is made in the thesis itself.

Mojtaba Ghadimi

Acknowledgments

This thesis is the last part of my formal studies in physics. A journey with its ups and downs that gave me the opportunity to meet and work along with many incredible people. I would like to thank all the teachers and professors that guided me through this journey and made me familiar with the amazing world of physics. A special thanks to my supervisors Professor David Kielpinski, Dr. Erik Streed and Dr. Mirko Lobino that always had the time for me to help me in my research and fulfilling this degree.

I would like to thank Ben Norton that patiently helped me in my transition to experimental physics and a special thanks to Valdis Blums that worked alongside me for more than two years. With him I had the absolute joy of working as a team to overcome difficulties of the project.

I would also like to thank my parents and my brother that have never stopped supporting me and gave me the opportunity to continue my studies knowing that they are always there to help me.

Last but not least, I would like to thank my wife Shahrzad that supported me in the decision to return back to science, even if that meant that she had to live far from her parents and start a whole new life.

Abstract

This thesis describes the use of diffractive mirrors for efficient collection of photons from an ion in a modern surface Paul trap. Ion light collection is one of the important steps of most of the quantum computing and communication protocols using trapped ions and has a direct effect on the performance of these protocols. This is the first demonstration of an integrated-optic for a surface ion trap and a step towards realizing scalable quantum computing and communication using trapped ions. These mirrors are monolithically integrated onto the ground electrode of the trap. The fabrication of the mirrors has been accomplished by patterning diffraction rings on the silicon dioxide substrate of the trap chip and then coating it with aluminium to form a diffractive mirror integrated onto the electrode. We verified that the altered trap is still functional and demonstrated that these mirrors substantially increase the efficiency of free space ion light collection and ion light single mode fibre coupling. The mirror design is aberration free and we demonstrated this by obtaining near Diffraction-limited images of an ion. To measure the collection efficiency of the diffractive mirrors, we performed a single photon generation protocol based on an optical pumping scheme and one chapter of this thesis describes the implementation of this scheme.

Contents

Acknowledgments	iii
Abstract	iv
Contents	iv
List of Figures	ix
1 Introduction	2
2 Integrated Diffractive Mirror Trap	7
2.1 Paul RF Trap	7
2.2 GTRI Microwave I Trap	12
2.2.1 DC Electrodes Voltage Control and Shuttling	15
2.2.2 RF Electrodes and RF Voltage Generation	19
2.3 Diffractive Mirrors	20
2.3.1 Theory of Diffractive Mirrors	22
2.3.2 Design of the Diffractive Mirrors	24
2.3.3 Fabrication of the Diffractive Mirrors	28
2.3.4 Characterisation of the Diffractive Mirrors	33
2.4 Atom Source	40
2.5 Vacuum System	41
3 Laser Systems, Cooling and Ionisation	43
3.1 Scattering Rate and Saturation Intensity	43
3.2 Yb Atomic Transitions	44
3.3 Ionisation	45
3.4 Laser Cooling	47
3.5 External Cavity Diode Laser	49
3.6 Optical Isolator	51
3.7 370 nm Diode Laser	52
3.7.1 Lock-in Amplifier	54

3.7.2	370 nm Laser Frequency Stablisation	55
3.8	399 nm Diode Laser	60
3.8.1	399 nm Diode Laser Frequency Stablisation	60
3.9	935 nm Diode Laser	63
3.10	Beam Combiner	64
4	Imaging and Optical System	66
4.1	Imaging Using External Bulk Optics	66
4.2	Diffraction-limited Imaging (Theory)	70
4.3	Imaging Using Microfabricated Collimators	73
4.3.1	Gaussian Beam Propagation Simulation	75
4.4	Near Diffraction-limited Image	77
5	Single Photon Generation	82
5.1	Atomic Transitions, Absorption and Emission Patterns	82
5.2	Single Photon Generation Protocol	85
5.3	Automatic Control Of The Lasers and The Detectors Using LabVIEW FPGA	87
5.4	Experimental Setup	90
5.5	Characterisation Of The Time Scales and Delays	94
5.6	Measuring Single Photons 2nd Order Correlation $g^{(2)}$	95
6	Efficient Fluorescence Collection With Diffractive Mirrors	98
6.1	Ion Fluorescence Collection	98
6.1.1	Experimental Setup	99
6.1.2	Theoretical Estimation Of Collection Efficiency	101
6.1.3	Measuring Collection Efficiency	102
6.2	Single Mode Fibre Coupling of the Ion Fluorescence	104
6.2.1	Experimental Setup	104
6.2.2	Theoretical Estimation Of Fibre Coupling Efficiency	106
6.2.3	Measuring Single Mode Fibre Coupling Efficiency	108
7	Conclusion	110
7.1	Future Work	110
A	Gaussian overlap calculation	113
B	Ion Size MATLAB Routine	115
C	Calculating M^2 MATLAB Routine	117
D	Gaussian Beam Propagation Simulation MATLAB Routine	122

E Coupling Efficiency Estimation MATLAB Routine	128
References	131

List of Figures

2.1	A four rod conventional Paul trap. Two RF electrodes labelled 1 and 3 and two segmented DC electrodes labelled 2 and 4 that are grounded in the middle and held at a positive potential at the end segments (Left) and RF electric field (Right) (Field image after [1])	8
2.2	Stability diagram for different values of a and q . The area in the middle is stable but the areas on top and bottom are unstable regions. (Fig. after [2])	10
2.3	Microscope image of the Integrated Diffractive Mirror Trap (Left). Middle ground electrode is $80 \mu m$ wide and RF electrodes are $30 \mu m$ wide. Segmented parts at the top and the bottom of the image are control DC electrodes. Right image is a schematic of RF electric field that creates a RF node on top of the trap. (Field image after [3])	11
2.4	Rotated coordinate system for RF potential. (Fig. from GTRI Microwave I Trap manual[4])	12
2.5	A schematic of the $11 \times 11 mm^2$ silicon chip of the trap (a) and the active trapping region (b), showing RF and DC trapping electrodes, capacitive RF filters, the loading slot, and the on-chip microwave waveguides. (Fig. from GTRI Microwave I trap manual[4])	13
2.6	Trap components including a packaged device with top screen removed for clarity (a), a photograph of the wirebond interface (b), and a photograph of a fully installed device with microwave connections (c). (Fig. from GTRI Microwave I Trap manual[4])	14
2.7	A cross section showing internal layers of the Microwave I Chip (the vertical direction is scaled by 10x for visual clarity). (Fig. from GTRI Microwave I Trap manual[4])	15
2.8	Dimensions and electrode IDs of the trapping region for a Microwave I trap. The z coordinates along the length of the trap correspond to the ion positions relative to the loading position. (Fig. from GTRI Microwave I Trap manual[4])	16

2.9	Screenshot of the LabVIEW program interface for controlling DC electrodes for shuttling and applying compensation fields. At the top part, the program displays the voltages that are currently being applied to the electrodes. Below that section, the user can enter a destination in the "Where to go um" field and a speed in "m-sec um" and start shuttling using the button "Start Shuttle / Update setting" to the left of those. The input fields at the bottom allows user to choose a file for each waveform and select between constant weight or position dependent weight. Left inputs are used to save two pre-sets for loading and shuttling and apply them when needed.	18
2.10	Schematic of the helical resonator used for RF input of the trap. Capacitive divider is used to sample the output voltage.	20
2.11	A diffractive mirror with 2π cycles. Red arrows are incoming beams at the centre and at the offaxis distance r . Blue arrows are reflected beams that both go to the focal point.	24
2.12	Microscope image of the integrated diffractive mirror trap taken by GTRI and layout of the array of the optics.	25
2.13	Left: Schematic of the design sizes for the 4-level grating structures. Right: Simulated diffraction efficiency as a function of the incidence angle of light. (Figure courtesy of David Kielpinski)	26
2.14	Complete layout of a single wafer, incorporating defence against both ion height errors and lateral offset errors.(figure courtesy of David Kielpinski) .	27
2.15	Representative image of the substrate prepared by GTRI to send to Fraunhofer Institute (details in text) (image courtesy of David Kielpinski)	28
2.16	Cross section as delivered by FHHI after diffractive mirror fabrication (mirror features are not to scale) (details in text) (image courtesy of David Kielpinski)	29
2.17	Small diffractive mirror features before (left) and after (right) metal deposition taken by GTRI.	30
2.18	a. The wafer after plasma etch b. Diffractive mirrors with oxide protection layer (details in text) (image courtesy of David Kielpinski)	30
2.19	a. DC/RF metal deposition and etch b. Top metal deposition and etch c. Final device cross section (details in text) (image courtesy of David Kielpinski)	31
2.20	Binary (left) and hybrid (right) diffractive mirrors after completed ion trap fabrication. (image taken by GTRI)	31
2.21	Full Binary DOE on a completed ion trap (Image taken by GTRI)	32
2.22	Dark field image of DOE's on a completed ion trap. (image courtesy of GTRI)	32
2.23	Ion transport image over the self-imager taken by GTRI	33

2.24 (a) Ion and image alignment when micromotion nulled. (b) Applied lateral electric field pushes the ion to the right, with a corresponding movement of the image to the left. (image taken by GTRI)	34
2.25 a. With the lens aperture closed, the depth-of-field is large enough that the central obscuration of the objective is visible as a dark inner region. The bright horizontal bands are patterns on the trap surface. b. Rough diagram of light collection from IDM with the reflective objective. The collimating optic collection efficiency data were taken such that the light would both be collected by the lens and pass through the iris when the iris was closed. (image courtesy of GTRI)	35
2.26 a. Direct imaging (iris full open) and b. Collimated light imaging (iris closed to minimum) of the ion. (image courtesy of GTRI)	35
2.27 PMT counts vs. ion position over the collimating optic for the lens aperture (iris) fully open and for the aperture at minimum (closed). The dashed lines are guides for the eye, showing the photon counts for the direct light from the ion, as extrapolated from the measurements in left wing of the plot. Both measurements have had position dependent backgrounds (measured separately without an ion) subtracted out. (graph by GTRI)	36
2.28 Schematic of bulk collection optics. The first lens collects and collimates the ion fluorescence and the second lens focuses the collected fluorescence onto the camera chip.	37
2.29 A single ion trapped in the IDM trap loading region. Imaging was performed using the bulk-lens objective. The diffractive mirrors were not used to obtain this image.	38
2.30 Comparison between bulk-lens and diffractive mirror imaging for a single ion in the IDM trap. Both images are taken under identical camera integration conditions and are background-subtracted to remove the scattered light. Left: bulk-lens image. Right: diffractive mirror image obtained with the loading zone collimator. The fluorescence collection efficiency is estimated as 4%. The loading zone collimator is cut in the middle to create the loading hole and this has been deformed the mirror and has increased the aberration.	39
2.31 Image of a single ion using the loading-zone diffractive mirror. The image was obtained by moving the ion several microns along the trap axis relative to the image in Fig. 2.30. The apparent duplication of the image is consistent with aberrations of the imaging system.	40
2.32 A schematic of the vacuum chamber which consists of the main octagonal part and branches for titanium sublimation pump, ion pump, ion gauge, oven connection Microwave feedthrough, DB25 connections and RF input. (Image taken from [7])	41

3.1	Relevant energy levels for neutral and ionised Yb. Left: Neutral Yb energy levels from [5]. Right: Yb^+ energy levels and branching ratios from [6]. Spontaneous decay times from $^2P_{1/2}$, $^2D_{3/2}$ and $^3D[3/2]_{1/2}$ states are 8.1ns, 53ms and 37.9ns respectively.	45
3.2	Loading ratio of ^{174}Yb for different frequency shifts and saturation parameter. Higher frequency shift increases the load ratio of ^{174}Yb but higher saturation parameter decreases this ratio.	47
3.3	A schematic of external cavity diode laser components	50
3.4	Schematic representation of 935 nm laser ECDL gains vs. wavelength. . . .	51
3.5	A Faraday optical isolator. The input polariser, P1, is set to maximum transmission. The Faraday medium rotates the polarisation by 45° and the output polariser, P2, set to the same angle, transmits the light. For a back-reflection the same process rotates the polarisation in the same direction and this makes the direction of the polarisation perpendicular to the axis of the input polariser, P1. Therefore the polariser rejects the light.	52
3.6	A schematic of 370 nm laser system. An external cavity diode laser generates a narrow linewidth laser near wavelength of 370 nm. Half-waveplates and polarising beam splitters are used to split the power for different components. These components include a wavemeter, polarisation spectroscopy system, Fabry-Perot cavity and two outputs with different frequencies for the ion trap.	54
3.7	A schematic of the 370nm laser locking system. The fast lock section uses a signal from a Fabry-Perot cavity to stabilise the frequency. The slower signal that comes from an atomic reference is used to stabilise the Fabry-Perot cavity length.	56
3.8	Saturation spectroscopy system that uses a high intensity counter-propagating beam to eliminate the Doppler broadening of the spectroscopy signal. . . .	57
3.9	A schematic of polarisation spectroscopy for 370nm laser. By using a pump beam with circular polarisation and a probe beam with linear polarisation that goes to a dual photodiode. A narrow zero crossing signal is generated.	58
3.10	Plot of polarisation spectroscopy and Fabry-Perot trace. The blue signal is the polarisation spectroscopy and the green signal is a Fabry-Perot trace. The free spectral range of the Fabry-Perot peaks is 1.25GHz. (graph courtesy of Valdis Blumes [7])	60

3.11 Schematic for 399nm-laser polarisation spectroscopy. The first beam through the hollow cathode discharge lamp is a circularly polarised pump beam. After the discharge lamp the beam is split into two and a weaker linearly polarised probe beam is sent back through the hollow cathode discharge lamp. The probe beam is then sent to the dual photodiode. The laser frequency is modulated at 20kHz and a lock-in amplifier is used to amplify the signal.	61
3.12 a. In a frequency dependent signal, change in signal is proportional to change in frequency times the derivative of the signal with respect to the frequency. b. The lock-in amplifier only amplifies the modulated signal which is proportional to derivative of the signal, therefore its output is positive where derivative is positive and vice versa.	62
3.13 399nm laser spectroscopy trace for neutral Yb. (graph courtesy of Valdis Blums)	63
3.14 Beam combiner setup for lasers in use. The two 370nm laser are combined using a polarising beam splitter and then 399nm and 935nm lasers are added using diachronic mirrors. A fast steering mirror and a lens mounted on a translator is used for adjusting the position and angle of the beam that goes to the vacuum chamber.	65
4.1 A schematic of the lens configuration in the bulk imaging mode (image is not to scale). The ion is located $60 \mu m$ above the chip. The objective lens with focal length of $60 mm$ is positioned $60 mm$ away from the ion. This lens collimates the ion fluorescence. The collimated beam is focused on the camera using a second lens located $260 mm$ away from the objective lens (vacuum chamber window omitted for clarity).	67
4.2 An image of the chip and a trapped ion located at the loading zone captured using bulk imaging system. Ion is located at the middle of the loading zone. The oval shaped scatter around the ion is the reflection of laser from the edge of the loading zone. DC electrodes are visible on both sides of the ion.	69
4.3 Three images from the ion and its image created by the self-imager diffractive optic for different ion positions. This optic forms an image from the ion on itself. Left: the ion is located before the self-imager. Middle: the ion is located on top of the self imager, images are almost overlapped and this shows that we have small lateral mismatch between optics fabrication and electrodes fabrication. Right: the ion located after the self-imager optic	69
4.4 Graph of intensity of the diffraction pattern for a circular aperture. First minima happen at $\pm \frac{1.22\lambda}{D}$, where λ is wavelength and D is the diameter of the aperture.	70

4.5 Numerical aperture (NA) of an optical system is a dimensionless number that characterizes the range of angles over which the system can accept or emit light. It is equal to $n \sin(\alpha)$, where n is the index of refraction of the medium and α is half of the acceptance angle.	71
4.6 $1/e^2$ intensity radius of a Gaussian beam. w_0 and θ are the radius and the angle of the far-field divergence of the ideal zero order Gaussian beam and w_{0R} and θ_R are the radius and the angle of the far-field divergence of the mixed mode beam.	72
4.7 An example of measuring M^2 by fitting equation 4.7 to the spot sizes around the focus point for the optical configuration shown in Fig. 4.10. The blue circles are the measured radii and the solid line is the fitted function. In this case M^2 is 1.36 which suggests that our beam is slightly aberrated.	73
4.8 Imaging using integrated collimating mirrors. The collimated light can be focused on the screen using a second lens. This method can be used if the distance between the mirror and the axillary lens is less than Rayleigh range of the beam which is 8.7 mm for one axis and 5.1 mm for the other axis. In our system the distance between the mirror and the first lens is 60 mm. This distance is much greater than the Rayleigh range of the beam and beam is diverging when it reaches the lens. Gaussian beam simulation must be used to predict the evolution of the beam and to design an optical system to image the light collected with the mirrors.	74
4.9 Numerical aperture (NA) of the mirror for the z axis. The distance from the ion to the mirror is 59.6 μm and the half side of the mirror along the z axis is $127 \div 2 = 63.5 \mu m$. Therefore $NA = \sin(\theta) = 0.73$	75
4.10 Gaussian beam propagation simulation (appendix D) for one of the settings we used for beam transfer. Blue curve shows the size of the beam in the x direction and red curve shows the size of the beam for z direction. Vertical black lines are lenses with f their focal lengths and z their distances from the diffractive mirror. r , zr and w labels, next to the focal length label, are radius of curvature, Rayleigh range and beam size respectively. Vertical blue and red lines show the focus points and for each axis the beam size, focus position and magnification is shown with respective color next to them. On the left side of the output graph, the program displays the diffraction limited size at ion position for each axis.	77
4.11 Near diffraction limited image of an $^{174}\text{Yb}^+$ ion obtained using integrated diffractive mirror and comparison with diffraction limited size. Solid angle coverage is 13.3% and exposure time is 1 second. Ion image size measured to be $338(1.6) \text{ nm} \times 268(1.2) \text{ nm}$ FWHM diameter.	78

4.12	The ion height for the different positions of the ion on the chip. When at the middle of the loading zone the ion height is $52 \mu\text{m}$. Ion height gradually increases by moving away from the loading point and becomes $58.6 \mu\text{m}$ outside of the loading zone. (graph after GTRI)	80
5.1	Relevant transitions for the single photon generation protocol. The 370 nm σ^- laser can only excite $^2S_{1/2} m_j = +1/2$ to $^2P_{1/2} m_j = -1/2$ transition. The excited ion may emit a σ -photon, with probability of $2/3$, and return back to $m_j = +1/2$ ground state or it may emit a π -photon, with probability of $1/3$, and decay into $m_j = -1/2$ state. This is a dark state for σ^- laser and the ion does not interact with the laser while in this state. For the σ^+ laser, after excitation, the ion will undergo the same type of decaying and emission as the case for σ^- laser. The only difference is that it can only excite $m_j = -1/2$ ground state but not $m_j = +1/2$ ground state.	83
5.2	Emission patterns of the π and σ polarised photons. Left: For the π -photons the maximum probability of emission is perpendicular to the magnetic field. No π -photon is emitted along the magnetic field direction. Right: The probability of emission of σ -photons along the magnetic field is twice the probability perpendicular to the magnetic field. Both polarisations are linear, if they are emitted perpendicular to the magnetic field. In this direction polarisation of the π -photons is along the magnetic field and polarisation of the σ -photons is perpendicular to the magnetic field.	84
5.3	a. Single photon generation protocol. 370 nm σ^- and σ^+ lasers are on for 500 ns to generate a continuous excitation cycle to cool the ion. Then only the σ^- laser remains on for another 500 ns to prepare the ion in the $m_j = -1/2$ ground state. For 1000 ns both lasers remain off to separate the preparation process from generation process. Detection is turned on 750 ns after the preparation and remains on for 1000 ns . 1000 ns after preparation, σ^+ generation laser is turned on and remains on for 250 ns . This generates two σ -photons on average and finally the ion emits a π -photon and goes to the dark state. By filtering the σ -photons using a polariser, only one photon is collected during the generation step. b. Relevant transitions for single photon generation protocol. (for details on transitions see section 5.1 and Fig. 5.2)	86

5.4	FPGA control program's user interface screenshot. In the default mode, the program shows counts/s for each detector with "DIO 14 Idle Counts(/s)" and "DIO 14 Idle Counts(/s)" outputs and applies the default values to the digital and analogue outputs. These default values are entered using vertical array inputs on the left side of the interface. The user can also choose to repeat a sequence of events and change the values of outputs during time. The time length of each element is entered in "Element Clock Cycles" field and the corresponding value of digital and analogue outputs can be entered under each element cell in the inputs provided for each output port. After pressing "Start Sequence" the program repeats the commands for the number of times given in "Number of Repetitions". During the execution of the sequence, the DIO14 and DIO15 outputs display the live accumulation of number of detections for each time element.	89
5.5	Schematics of the electronic setup for the single photon generation protocol. FPGA card controls the lasers and detection. To turn the lasers on and off, we use FPGA digital outputs to send a TTL signal to the AOM drivers. To turn the detection on and off, we use RF switches between PMTs and the time-tagger box.	91
5.6	Optical set-up for the collection of the single photons. a. The optical set-up used to transfer, collimate and resize the beam to send it to the single photon analyser set-up. The first two lenses are used in the bulk imaging set-up (4.1). We leave this set-up untouched and use a $f=250\text{ mm}$ lens to collimate the light. The next two lenses ($f=75\text{ mm}$ and $f=125\text{ mm}$) act as a telescope to resize the beam. This last telescope is not necessary for this experiment and is used for mode matching for the fibre coupling experiment. b. Single photon analyser set-up. The polariser is mounted on a rotational mount to set its axis to the direction of the polarisation of the π photons and filter the σ -photons. Using a non-polarising 50-50 beam splitter, the π -photons are split and sent to the two photo multiplier tubes (PMTs). A time-tagger device analyses the statistical regime of photon emission (see section 5.6).	93
5.7	Number of photons generated in each step after time t after turning on the generation laser. The data is taken by repeating the sequence for one minute and then normalising the data to one at infinity. the blue fitted graph shows that the exponential time scale of the generation is $0.21\mu\text{s}$. This is equivalent to the average generation of 0.69π photons in 250 ns of generation.	95

5.8 Second order correlation $g^{(2)}$ for the single photon generation protocol. The red graph and the red axis show the raw counts. To calculate $g^{(2)}(0)$ we integrated all the counts in each peak to calculate unnormalised $G^{(2)}(\tau)$ and using an exponential decaying fit estimated $G^{(2)}(\infty)$. We used $G^{(2)}(\infty)$ as the normalising factor and calculated $g^{(2)}$ for different delays. These values are shown with the black dots. $g^{(2)}(0)$ is 0.12(2).	97
6.1 The optical set-up for the demonstration of the collection efficiency of the 4th collimator on the γ chip. The focal length of this collimator is $59.6 \mu m$. This collimator collects and collimates the light from the ion. Because of the short Rayleigh range of 8.7 and 5.1 mm (see section 4.3), this beam becomes divergent before exiting the vacuum chamber. The first 2 lenses are the lenses that are used for external bulk optics imaging. This part focuses the beam 172 mm after the second lens. A $f = 250 mm$ lens is used to collimate the light again. A final telescope consisting of a $f = 75mm$ and $f = 125mm$ resizes the beam and sends that to a PMT. In principle this complex optical set-up is not necessary for this experiment. The only reason that we used this set-up was that we wanted to use the same optical system for this experiment and the single mode fibre coupling experiment. The iris is used to decrease the counts to 50% and reduce the polarisation blurring effect. The polariser is mounted on a rotational mount and its axis is set to the direction of the magnetic field to let through the π photons and filter unwanted σ photons. This is necessary for the single photon generation protocol (see section 5.2).	101
6.2 Optical set-up used for coupling ion fluorescence into the single mode fibre. The optical set-up collimates the ion light and resizes the beam to match it with the mode size of the fibre. An aspheric lens couples the light into the single mode fibre.	104
6.3 Theoretical simulation of single mode coupling efficiency. Mode size matching efficiency, effect of mode quality M^2 and total coupling efficiency is plotted for different magnifications.	108
6.4 The fibre coupling stage used to couple ion light. A Thorlabs(TM) MAX313D 3-axis stage is used to mount the Thorlabs(TM) PM-S350-HP fibre and Thorlabs(TM) C671TME-A lens with focal length of 4.02 mm.	109
7.1 A schematic of parallel integrated optics architecture. One array of planar waveguide circuits are used to deliver excitation light to the ions and the other array collects the fluorescence. Mode matching is achieved by the design of the integrated diffractive mirrors. (image from [8])	112

CHAPTER 1

Introduction

In the early 1900s when quantum mechanics emerged, there was no implication that it might enter the realm of practical technologies [9]. It is only for a few decades that people started realising that this theory can be used to open ways for new technologies. Lasers were one of the technologies that used an entirely quantum effect, stimulated emission. When in 1961 Maiman experimentally demonstrated the first laser[10], people called it a solution that is looking for a problem and today it is omnipresent everywhere from manufacturing sectors to our DVD-drives.

In 1982 Richard Feynman developed the idea of quantum computing when he discovered that simulating quantum systems using classical resources is an intractable problem[11]. By this time experimental physicist had already started working on controlling individual quantum systems, like single atoms, for about a decade[12] but the main interest in the field arose after Shor's paper in 1994 on discrete logarithms and factoring [13]. This algorithm is particularly important because the most widely used cryptographic systems on the internet, RSA, is based on intractability of factoring a large number with classical computers. Shor showed that this quantum factoring algorithm has a polynomial complexity in the input number size ($O[\log(N)^2 \log(\log(N)) \log(\log(\log(N)))]$) while the complexity of the best known classical solution is sub-exponential ($O[e^{1.9\log(N)^{1/3} \log(\log(N))^{2/3}}]$). An estimate shows that this can reduce the time needed for factoring a 400-digit number from the age of the universe with current best supercomputers to about a minute with a quantum computer with the same clock rate[14].

Quantum physics doesn't only provide a solution to break the RSA encryption, it also provides a replacement. Quantum key distribution protocols like BB84 [15] enable us to share a secret key with a provably secure method, guaranteed by the laws of quantum mechanics.

To realise a quantum computing or communication protocol, one needs to be able to decouple a quantum system from the environment to prevent decoherence and at the same time have sufficient control over its evolution. There are many candidate qubits (quantum bits) for physical realisation of quantum computers; atoms, photons[16], charge in superconductors[17] and quantum dots[18] are among the platforms that have been used for quantum information processing. Photons are the most favourable option for quantum

networking and have very long decoherence times, however when it comes to interaction and entanglement, practical implementation is challenging[19].

In 2000 DiVincenzo proposed a list of requirements that is needed for physical implementation of a quantum computer[20]:

1. Having a scalable well characterised qubit.
2. The ability to initialise a state.
3. Having long decoherence times.
4. Having a universal set of quantum gates
5. The ability to measure each qubit

He also proposed two extra conditions for quantum communication:

1. The ability to interconvert stationary and flying qubits.
2. The ability to faithfully transmit qubits between two locations.

Trapped atoms in ultra-high vacuum meet all the DiVincenzo conditions for quantum computing. The longest decoherence time demonstrated using atomic qubits is 50 seconds[21] which is orders of magnitude longer than the typical fast pulsed gates times which range from $1 - 10\mu s$ [22]. All the basic operations including qubit state preparation[23, 24], manipulation[25, 24] and readout[24, 26] have already been demonstrated and gate errors down to the order of 10^{-4} has been realised[27]. Despite the fact that the gate errors are getting smaller, it is impossible to make them zero. Therefore we need an error correction scheme to compensate for the errors. It has been shown that the current single state error levels are sufficient for the implementation of these error correction schemes[28].

In 2004 Chiaverini *et al.* demonstrated an error correction scheme with one primary ion and two ancilla ions and showed that it is robust against spin flips[29]. There is also a proposal for error correction in trapped ion quantum computing that uses 5 ancilla ions and only needs global entangling operations[30].

Researchers have been able to demonstrate full quantum algorithms with trapped ions. Debnath *et al.* have demonstrated a programmable quantum computer module with 5 ion qubits[31] and Monz *et al.* demonstrated the first scalable Shor algorithm[32]. Grover's quantum search algorithm has also been demonstrated with trapped ions[33]. In 2007 Moehring *et al.* demonstrated the remote entanglement of two distant ions[34]. This has applications in quantum communication and distributed quantum computation.

Having demonstrated all the fundamental quantum gates with ions, scaling the number of qubits is now the main technological obstacle. The most widely used multi-qubit gate in

trapped ion quantum computing are the Cirac-Zoller[35] and Molmer-Sorenson[36] gates. These methods exploit the collective vibrational modes of the ions, arranged like a 1D crystal in a trap, as a quantum data bus to transfer the entanglement. These schemes are expected to be limited to tens of ions due to decoherence effects[37, 38]. The maximum number of ions entangled with this scheme is 14[39]. There are two main roadmaps to scale the number of qubits in ion based quantum computers.

One approach is the modular architecture which consists of multiple registers of ions [40]. In each register, ions interact locally through common motional modes. The limit on the number of ions in each register is imposed by decoherence effects[37, 38]. Entanglement between ions in different registers is completed via a probabilistic photonic interface[41].

Second proposition is using a quantum charge-coupled device[42]. In this device it is possible to shuttle ions to different regions of the trap. These regions are dedicated to different functions such as memory, interaction or sympathetic cooling. Sophisticated ion trap technologies that currently exist, enable us to trap multiple ions and transport them individually[43, 44]. Successful transport of ions around different areas and through junctions has been demonstrated by different groups[45, 46, 47].

Two categories of optical interconnects are used in trapped ion quantum computing and communication: laser addressing optics and photon collection optics. Laser addressing of individual ions is needed for different tasks including laser cooling, gate operations and state readout. The normal method of laser addressing is through using external bulk optics [48, 49]. Recently an integrated scalable scheme has been demonstrated for addressing of an ion qubit by researchers at MIT's Lincoln Laboratory [50]. Using lithography they fabricated nanophotonic waveguides that routes laser light and focuses that on an ion using focusing grating couplers. These waveguides are fully integrated into the substrate of a surface-electrode ion trap chip.

Photon collection optics are used in many operations including reading the state of a qubit. The reading process is accomplished through exciting the ion using specific laser frequency and polarisation. Depending on the qubit state ion may start fluorescing or may not interact with laser. By detecting this fluorescence on a photon detector, one can measure the state of the qubit. The speed and reliability of the readout is directly proportional to the percentage of the fluorescence collected. Coupling ion fluorescence into a single mode fibre is also important for applications such as remote entanglement[34] and quantum communication.

Conventionally the ion light is collected using bulk refractive optics placed outside of vacuum chamber. These optical components normally do not operate at high numerical aperture(NA) and therefore do not collect high percentage of ion light. To cover high NAs, these optics must have large diameters and this prevents them from being a candidate for collection of light from high number of individual ions. Typical collection for these methods is between one to two percent of the total ion light. Most of the proof of the principle

experiments in trapped ion quantum computing have been accomplished using these type of optical systems[51].

Using high finesse cavities is one of the methods to efficiently collect ion light[52, 53, 54]. Because the collected light is already in one optical mode, most of it can be coupled into a single mode fibre without the need for aberration correction. The drawback for this method is that micro fabrication and alignment of the cavity is extremely hard and it changes the properties of atomic transitions.

Bulk metallic spherical mirrors are one of the successful methods of ion fluorescence collection. Collection efficiency of 25% has been reported using these mirrors[55]. The problem with this method is that the collected light is hugely aberrated and without sophisticated aberration correction schemes it is not possible to efficiently couple that light into a single mode fibre. Single mode fibre coupling is necessary for many important applications like remote ion entanglement and quantum networking using ions. To cover high percentage of the total solid angle around the ion researches developed the Stylus ion trap[56] that uses a metallic parabolic mirror to cover 80% of the solid angle. The problem with this technology is that it limits the laser access and is not integrable into modern surface trap. Micro spherical mirrors are also used in a surface ion trap and reported to improve the normal light collection by 1.9 times[57], but they suffer from the same aberration problem.

Collecting ion light into multi-mode fibre is another method of fluorescence collection. This method is good for ion state readout but not for many other applications that need single-mode fibre coupling. Efficiency of 2.1% has been reported in a surface ion trap by collecting ion light directly into a multi-mode fibre [58], while micro-fabricated diffractive lenses achieved coupling of 0.388% [59]. In an end-cap, trap collection of 6% into two multi-mode fibres was reported [60].

In our group diffractive lenses were used for ion light collection[61], near diffraction limited imaging[62], and imaging the shadow of a single atom[63]. In that project diffractive rings were patterned on a fused silica substrate to form a flat Fresnel lens with diameter of 5 mm and focal length of 3 mm. The lens was installed on a needle Paul trap in a vacuum chamber and a collection efficiency of 4.2% was demonstrated.

In this project we designed and fabricated diffractive optics integrated into a surface Paul trap that can efficiently collect light and couple it into a single mode fibre. High resolution imaging was also demonstrated with these optics. To fabricate these optics, the oxide substrate of the middle ground electrode of the chip was patterned using e-beam lithography. The patterned area was subsequently metallised with aluminium to form the mirrors. The size of these mirrors is $80 \times 127 \mu m$ and their focal length is about $60 \mu m$. Using these mirrors we demonstrated 5.8(8)% ion fluorescence collection efficiency. The advantage of this scheme is that the design is scalable and it is monolithically integrated into the trap and regardless of its very small dimensions, it is capable of collecting a

considerable amount of light.

In the process of measuring the mirror collection efficiency we developed and used an on-demand single photon generation protocol and observed $g^{(2)}$ of 0.12(2). This shows that our generation scheme works in single photon regime and we can generate a known amount of photons. Comparing the number of detected photons with the number of generated photons, we calculated the mirror collection efficiency.

Using this mirror, we captured a near diffraction limited image of an ion. The image is 0.6% larger than the diffraction limit along the smaller side of the mirror and 4% larger along the larger side of the mirror. M^2 of this image is 1.36(9) and 1.54(9) for the two axes.

Free space light collection is important for ion state readout but other applications in quantum information processing using ions require single-mode fibre coupling. This includes probabilistic entangling quantum gates[64], quantum teleportation[51], Bell inequality violation[65], remote entanglement[34], ion light interference[66] and ion photon entanglement[67]. Single mode fibre coupling is also especially important for modular architectures and all the operations that need remote ion-ion entanglement[34]. The best ion light single-mode fibre coupling efficiency reported is 1.4%[68]. For π -photons, we demonstrated coupling efficiency of 71(5)% into single mode fibre. This is equivalent to collecting 4.1(6)% of the total π -photons into the single-mode fibre. This is achieved using no corrective optics for aberration and the fluorescence beam was just size-matched to the fibre mode.

In this thesis I describe the design and fabrication of integrated diffractive mirrors implemented on a surface ion trap and explain the demonstration of its efficiency in light collection, imaging, and single-mode fibre coupling. Chapter 2 covers theoretical and practical aspects of trapping an ion and shuttling it to different regions of the trap. It also covers the design and fabrication process of integrated diffractive mirror. Chapter 3 describes the lasers we used for cooling and single photon generation. Chapter 3 explains imaging of the ion using external bulk optics for trapping and shuttling and diffraction limited imaging with integrated diffractive mirrors. Chapter 4 explains the single photon generation protocol that was used for demonstration of mirror collection efficiency. Chapter 5 covers the demonstration of free space ion light collection efficiency and single mode fibre coupling efficiency of the mirrors. Finally the conclusion chapter discusses possible improvements and future projects.

CHAPTER 2

Integrated Diffractive Mirror Trap

Long decoherence time is one of the important requirements for a qubit to be a practical candidate for quantum computing. To be able to prevent decoherence , we keep the ion in a vacuum chamber. To minimise thermal relaxation, this ion cannot be in contact with any material in the vacuum chamber. Because of the electric charge of the ion it is possible to use electric or magnetic fields to trap the ion. The easiest configuration that comes to mind is using a static confining electric field that is confining in every direction but this is impossible due to Gauss's law. Gauss's law states that: the total of the electric flux out of a closed surface is equal to the charge enclosed divided by the permittivity.

$$\oint_S \vec{E} \cdot d\vec{A} = \frac{q}{\epsilon} \quad (2.1)$$

Where \vec{E} is the electric field, $d\vec{A}$ is a surface element on a closed surface, q is the electric charge inside the closed surface and ϵ is the medium's permittivity. This means that if we have an electric field that is pointing towards a certain point in every direction, there must be a electric charge inside that volume (other than the one that we want to trap) to make it possible.

There are two common solutions for this problem: Penning traps and Paul RF traps. In a Penning trap a uniform magnetic field, applied along the z axis, forces the electric charge to rotate with the cyclotron frequency in the xy plane[69]. Adding an inhomogeneous electric quadrupole field confines the ion in 3 dimensions. In our experiment we use a Paul RF trap in an ultra-high vacuum chamber. This trap does not use magnetic field for trapping. Instead it uses a DC field in combination with an alternating RF field to confine the ion.

2.1 Paul RF Trap

Paul RF traps use an alternating electric field (RF field) to confine an ion. Depending on configuration it can confine an ion in 3 dimensions but in some configurations it confines the ion in two dimensions and needs an extra DC field to confine the ion in the third dimension. Fig. 2.1 shows a conventional layout of a linear Paul trap. This trap consists

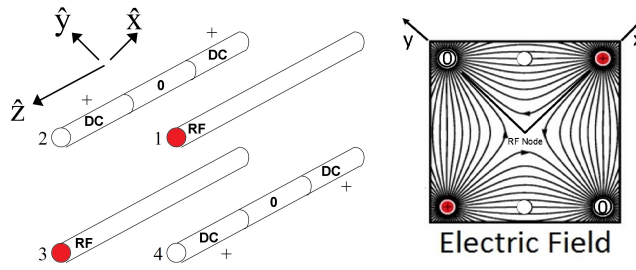


Figure 2.1: A four rod conventional Paul trap. Two RF electrodes labelled 1 and 3 and two segmented DC electrodes labelled 2 and 4 that are grounded in the middle and held at a positive potential at the end segments (Left) and RF electric field (Right) (Field image after [1])

of two parallel rods connected to an RF potential (electrodes with the red dots) and two segmented DC rods that are grounded in the middle but have positive voltage at the end parts. Right side of the Fig. 2.1 shows the RF field created by this setup during the period that RF potential is positive. When the RF potential switches to negative, we have the same pattern but with the reverse electric fields. The direction of the electric field shows that when the RF potential is positive, the field is confining along the x axis and it is outward along the y axis. When the sign of RF potential changes, the field becomes confining along the y direction and outward along the x direction. Solving the equation of motion shows that -for some given RF frequencies and amplitudes- this field confines the ion at the RF node.

Given an RF voltage on red electrodes $V_0 \cos(\Omega t)$ (Ω is the RF drive frequency) and DC voltages on the end parts U_0 , the quadrupole potential is [70] :

$$\phi(\vec{x}, \vec{y}, \vec{z}, t) = \frac{\kappa_{RF} V_0 \cos \Omega t}{2r_0^2} (x^2 - y^2) + \frac{\kappa_{DC} U_0}{r_0^2} \left(z^2 - \frac{\epsilon_{DC} x^2 + (1 - \epsilon_{DC}) y^2}{2} \right) \quad (2.2)$$

Where r_0 is the distance between RF electrodes and κ_{RF} , κ_{DC} and ϵ_{DC} are dimensionless geometric factors. In reality the potential will have higher order quadrupole terms but as long as the ion displacement from the RF node is much smaller than the distance between the RF electrodes, the potential above is a good approximation.

The equation of motion for a particle in an electric potential is:

$$m \frac{d^2 \vec{r}}{dt^2} = -Q \vec{\nabla} \phi(x, y, z, t) \quad (2.3)$$

Inserting the potential from the equation 2.2 and rearranging and separating the variables we arrive at the equation below for the x direction:

$$\frac{d^2x}{d\xi^2} + (a - 2q\cos 2\xi)x = 0 \quad (2.4)$$

Where:

$$\xi = \Omega t / 2 \quad (2.5)$$

$$a = \frac{4eU_0\epsilon_{DC}\kappa_{DC}}{m\Omega^2 r_0^2} \quad (2.6)$$

$$q = \frac{2e\kappa_{RF}V_0}{m\Omega^2 r_0^2} \quad (2.7)$$

This form of differential equation is called a Mathieu equation. This form is common in many problems like solving wave motion in periodic media. For this type of periodic equations we can apply Floquet's theorem and use answers with the periodic form below to find the solutions:

$$x(\xi) \propto e^{\pm i\beta\xi} f(\xi) \quad (2.8)$$

With $f(\xi + \pi) = f(\xi)$. In trapping ions, we work in a regime where $\beta = \beta(a, q)$ is real. In this regime the ion motion is stable for $|a| < q^2 \ll 1$ [2]. Expanding for small values of a and q we find:

$$x(\xi) \approx x_0 e^{i\beta(\xi - \xi_0)} \left(1 + \frac{q \sin(2\xi)}{2} \right) \quad (2.9)$$

$$\beta \approx \left(a + \frac{1}{2}q^2 \right)^{1/2} \quad (2.10)$$

where ξ_0 is a constant phase. This solution can be interpreted as a periodic motion with angular frequency $\beta\Omega$ that is being modulated by the periodic term in the brackets with angular frequency Ω . The first term is called secular motion and the second term is called micromotion.

In reality stray electric fields will be present at the trapping site. This can happen for example if insulating parts of the trap become charged. This field applies a constant force that displaces the ion from the center of the trap. For a Doppler cooled ion this displacement is usually small enough to ignore the spatial variation of the RF field therefore the ion will have the same secular motion. On the other hand the change in the micromotion term is large. If we add the electric force imposed on ion by the stray electric field to equation 2.3, the solution of the equation will be:

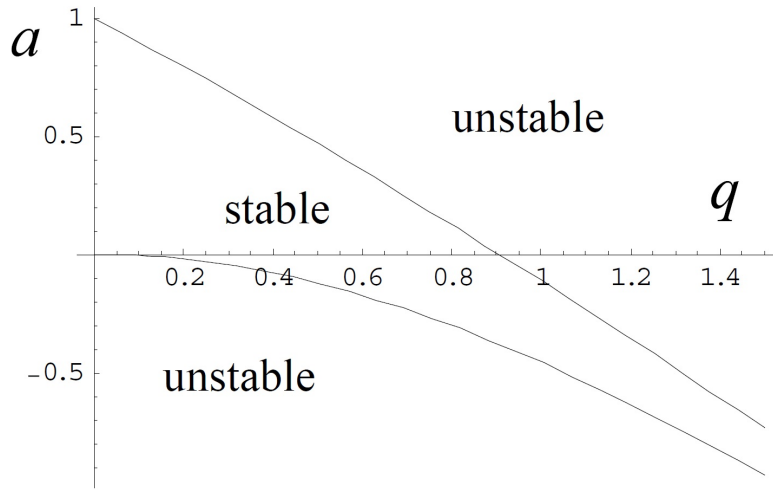


Figure 2.2: Stability diagram for different values of a and q . The area in the middle is stable but the areas on top and bottom are unstable regions. (Fig. after [2])

$$x(\xi) \approx x_0 e^{i\beta(\xi-\xi_0)} + x_1 \left(1 + \frac{q \sin(2\xi)}{2} \right) \quad (2.11)$$

Where $x_1 = 4QE/m\omega^2$ is the displacement, Q is the electric charge of the ion and E is the electric field. The amplitude of a Doppler cooled ion is usually less than 100 nm therefore even a electric field as small as 100 V/m can significantly increase this amplitude. Depending on the trap depth (determined by RF drive amplitude and frequency), the electric field may eject the ion from the trapping potential. To prevent the loss of an ion and keeping it as cool as possible, traps have DC electrodes that can generate fields to cancel the stray fields in every direction. In some traps, these DC electrodes are also used to move the ion along the 1D RF node.

Fig. 2.2 shows the stability condition for different values of a and q . In atomic ion trapping typically $q \approx 0.1$ is used, and q rarely goes over 0.3.

In our surface Paul trap shown in Fig. 2.3 the DC and RF electrodes are all in the same plane. As it is shown in the left side of the figure, the trap has two flat RF electrodes and one ground electrode between them that stretches along the trap. The width of the RF electrodes are $30 \mu m$ and the width of the ground electrode is $80 \mu m$. This creates an RF node $58.6 \mu m$ above the surface (As shown in the right side of the Fig. 2.3). Even though the field is asymmetric, near the RF node, to first order, it can be approximated by the quadratic potential discussed above. This RF field confines the ion in the xy plane. In the z direction an ion can be confined by using DC electrodes shown at the top and bottom of the microscope image. For this trap, Poisson's equation is used to find the voltages needed

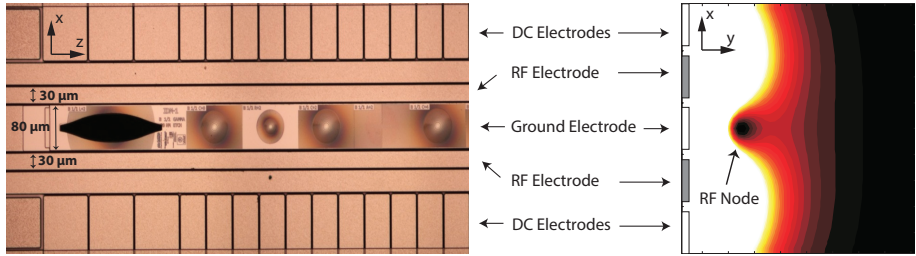


Figure 2.3: Microscope image of the Integrated Diffractive Mirror Trap (Left). Middle ground electrode is $80 \mu m$ wide and RF electrodes are $30 \mu m$ wide. Segmented parts at the top and the bottom of the image are control DC electrodes. Right image is a schematic of RF electric field that creates a RF node on top of the trap. (Field image after [3])

to create a confining harmonic potential along the z axis. If we gradually move the center of this field to another position, a confined ion will be shuttled to that position. Other than confining and shuttling, DC electrodes can provide a constant electric field along x , y or z axis to cancel stray electric fields. There are also two long DC electrodes, parallel to the RF electrodes, that can create an asymmetry that is used to slightly rotate the RF axis (Fig. 2.4) to make cooling possible for a laser beam parallel to the surface of the trap (for detailed discussion of the cooling process refer to 3.4).

Trap secular frequencies depend on both RF and DC potentials but we can ignore DC potentials to calculate an approximate value for the trap frequencies for directions perpendicular to the RF axis (refer to the trap manual provided by GTRI [4]). Neglecting DC potentials, the approximate quadrupole RF potential is:

$$\phi = \frac{V_0 \cos(\Omega_{RF} t)}{2} \frac{x^2 - y^2}{R^2} \quad (2.12)$$

Where x and y are the radial coordinates aligned with the RF quadrupole, V_0 is the RF amplitude, Ω_{RF} is the RF angular frequency, and R is a geometric factor of the trap. For this trap R is $133 \mu m$ inside the loading zone and $142 \mu m$ outside the loading zone. For the potential above the radial angular secular frequency is degenerate and is equal to:

$$\omega = \frac{QV_0}{\sqrt{2}\Omega_{RF}mR^2} \quad (2.13)$$

Where Q is the ion charge and m is the ion mass. To increase the secular frequency it is possible to increase the RF amplitude but this value is limited by RF breakdown voltage for the $4 \mu m$ gap between the RF electrodes and the ground electrode. For the the RF frequencies that we use ($26 - 29 MHz$), this break down voltage is $250 V$. We keep this voltage below $200 V$ in our normal operations.

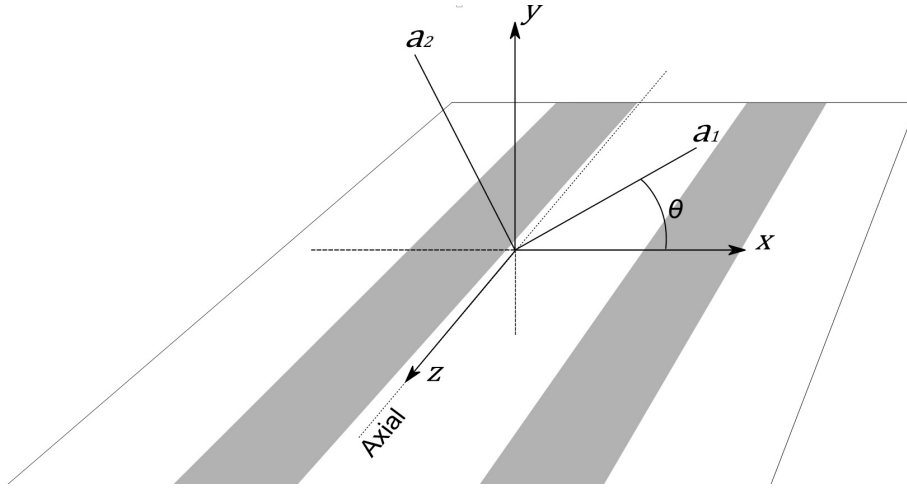


Figure 2.4: Rotated coordinate system for RF potential. (Fig. from GTRI Microwave I Trap manual[4])

2.2 GTRI Microwave I Trap

The ion trap that is used in this project is a modified version of the GTRI(Georgia Tech Research Institute) Microwave I ion trap. We modified the trap by adding diffractive mirrors to the middle ground electrode. This modification does not have an effect on the trapping functionality of the chip. In this section we explain the unmodified trap and the diffractive mirrors are discussed in section 2.3. The GTRI Microwave I ion trap is specificity designed for quantum information processing tasks. It is a flat surface trap and the ion sits $58.6 \mu m$ above the surface.

This chip trap includes two waveguides (Fig. 2.6b) along the trap axis that produce a polarisation-tunable standing microwave field for global addressing of $^{171}Yb^+$ hyperfine qubits. Two Corning Gilbert A010-L34-02 GPO microwave connectors shown in Fig. 2.6c are the inputs for these waveguides. These input are connected to SMA microwave vacuum feedthroughs via Accu-Glass in-vacuum coaxial lines. Using these inputs a $12.6 GHz$ microwave field can be supplied to drive the $^{171}Yb^+$ hyperfine transitions. These hyperfine levels are used to encode a qubit.

In this trap photoelectrons, generated by UV laser hitting the metal parts of the trap, can easily charge the exposed insulating substrate between the electrodes. Electric potentials created by this effect can be so large that can make it impossible to counter them with DC electrodes. This can create large micromotions that can eject the ion from the trap. To reduce this effect the trap has an integrated grounded shield outside the active region (Fig. 2.6c). This part consist of a flat metal part on the sides and a metallic mesh on top of the trapping area to provide optical access. Existence of this shield also simplifies the fields created by control electrodes. This shield is placed a few millimetres

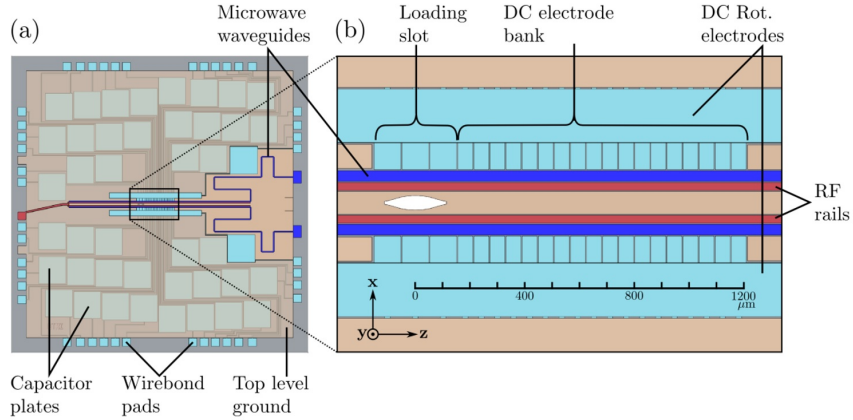


Figure 2.5: A schematic of the $11 \times 11 \text{ mm}^2$ silicon chip of the trap (a) and the active trapping region (b), showing RF and DC trapping electrodes, capacitive RF filters, the loading slot, and the on-chip microwave waveguides. (Fig. from GTRI Microwave I trap manual[4])

above the chip surface to allow laser access parallel to the surface. Because this shield is shorted to the trap ground, it cannot be used as a DC electrode or driven by a RF voltage for trap frequency measurements.

The trap has built-in capacitors around the trapping area (Fig. 2.5a) to reduce RF pickup on the control electrodes. Along the trap axis there are 21 pairs of DC electrodes to enable shuttling. It has two large control electrodes along the entire trap axis, for radial micromotion nulling and rotation of principal motional axes. These long electrodes can also be connected to an oscillating source to perform mode frequency measurements. In this test the oscillating voltage creates an oscillating field at the ion and this excites motion when the frequency is tuned close to resonance with a normal trap mode. In this chip, light access to the ion is along the axial direction and along both of the 45° diagonals. In our setup, we do not have a window along the axial direction and can only use the two 45° diagonals.

The chip carrier, which the trap is mounted on, has 98 pins on the bottom part (many of them are unused or redundant) and sits on a socket which is connected to a number of in-vacuum DC cables and through them to four Accu-Glass 100220 DB25 vacuum feed-troughs. The pins must be shielded from the neutral atom oven (section 2.4) to prevent Yb deposition and shorting.

This trap is designed to work in ultra-high vacuum. Operating at atmospheric pressure can lead to sparking between the electrodes and destroying the trap. This is because the border between the electrodes is narrow ($2\text{-}9 \mu\text{m}$) and therefore the RF breakdown voltage is only 1 V operating at atmospheric pressure, while it is 250 V in ultra-high vacuum. If voltages higher than breakdown voltage is applied, localised discharges start and if

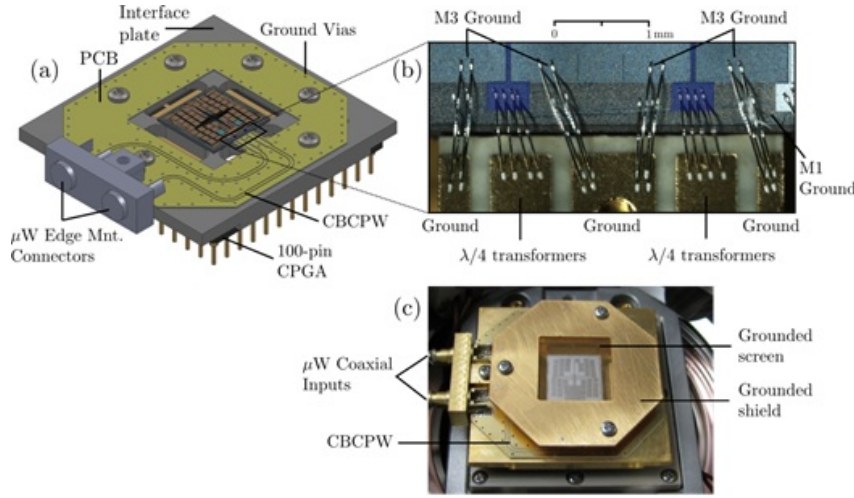


Figure 2.6: Trap components including a packaged device with top screen removed for clarity (a), a photograph of the wirebond interface (b), and a photograph of a fully installed device with microwave connections (c). (Fig. from GTRI Microwave I Trap manual[4])

operated for long hours, erode the RF electrode. This happened in this project due to inaccuracy of RF voltage pick-off that we used to monitor RF voltage and we had to replace the trap with a new one.

The chip area is approximately 1.1 cm^2 and it is $500 \mu\text{m}$ thick. It is made of five alternate aluminium and silicon dioxide layers on top of a Si substrate (Fig. 2.7). The bottom metal layer, M1, is $1 \mu\text{m}$ thick and shields RF field from high-loss Si substrate. On top of M1 there is a $10 \mu\text{m}$ Silicon dioxide layer which creates a substrate for the second metal layer M2. Capacitors are in this layer. On top of M2 there is a $1-2 \mu\text{m}$ silicon dioxide layer and on top of that is the third metal layer M3 with the thickness of $1 \mu\text{m}$. This layer is grounded and restricts the portion of the DC electrodes that influences the ion.

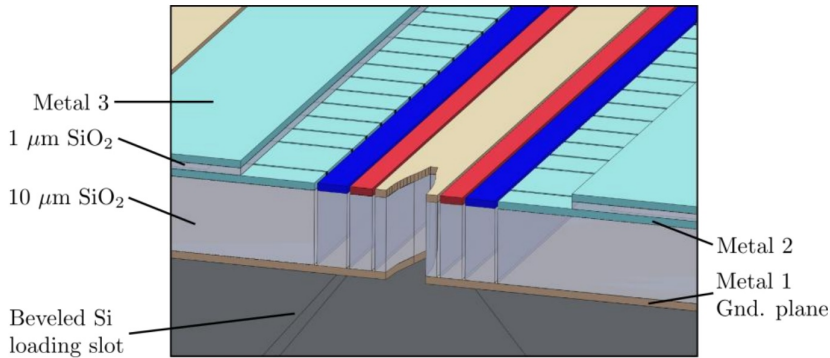


Figure 2.7: A cross section showing internal layers of the Microwave I Chip (the vertical direction is scaled by 10x for visual clarity). (Fig. from GTRI Microwave I Trap manual[4])

2.2.1 DC Electrodes Voltage Control and Shutting

The electrode structure of the trap is shown in Fig. 2.8. The trap has two long DC electrodes, 5 and 6, along the trap axis, array of 21 pairs of DC electrodes, microwave rail, RF electrodes that stretches along the trap axis, and the middle ground electrode. The rest of the metals in this area and around it are grounded. DC pairs around the loading zone are roughly $100 \mu m$ wide and rest of the pairs are $80 \mu m$ wide for better precision in ion shuttling and positioning. The width of the middle ground electrode that stretches along the trap axis is $80 \mu m$. In the modified trap, optics are patterned on this electrode and the width of this electrode defines the width of these optics. The white oval shaped cut between electrode 9 and 10 is the loading zone hole. Neutral atom oven (section 2.4) is placed under this hole. After trapping, ion appears at the center of this region. At this point ion height is $52 \mu m$ but when it leaves the loading region the height becomes $58.6 \mu m$.

DC electrodes are connected to the voltage controllers through four DB25 feed-troughs. The map between DC electrodes and DB25 pins is provided in the trap manual[4]. A National Instruments PXI-1044 14-slot chassis with 12 NI PXI-4713 cards controls the DC voltages. This device can apply -10 to $+10 V$. GTRI provided us with a 2X amplifier to increase the voltage range to -20 to $+20 V$. To generate the correct trapping potential, it is important that DC and RF controllers have a common ground.

DC electrodes are used for different functionalities. This includes generating longitudinal, lateral and vertical DC compensation voltages and generating harmonic potential along the trap axis. The harmonic voltage confines the ion along the trap axis where RF trapping potential does not confine it. By moving the center of this harmonic potential we can shuttle the ion along the trap axis.

GTRI team use a Poisson solver software for each of the above functionalities to de-

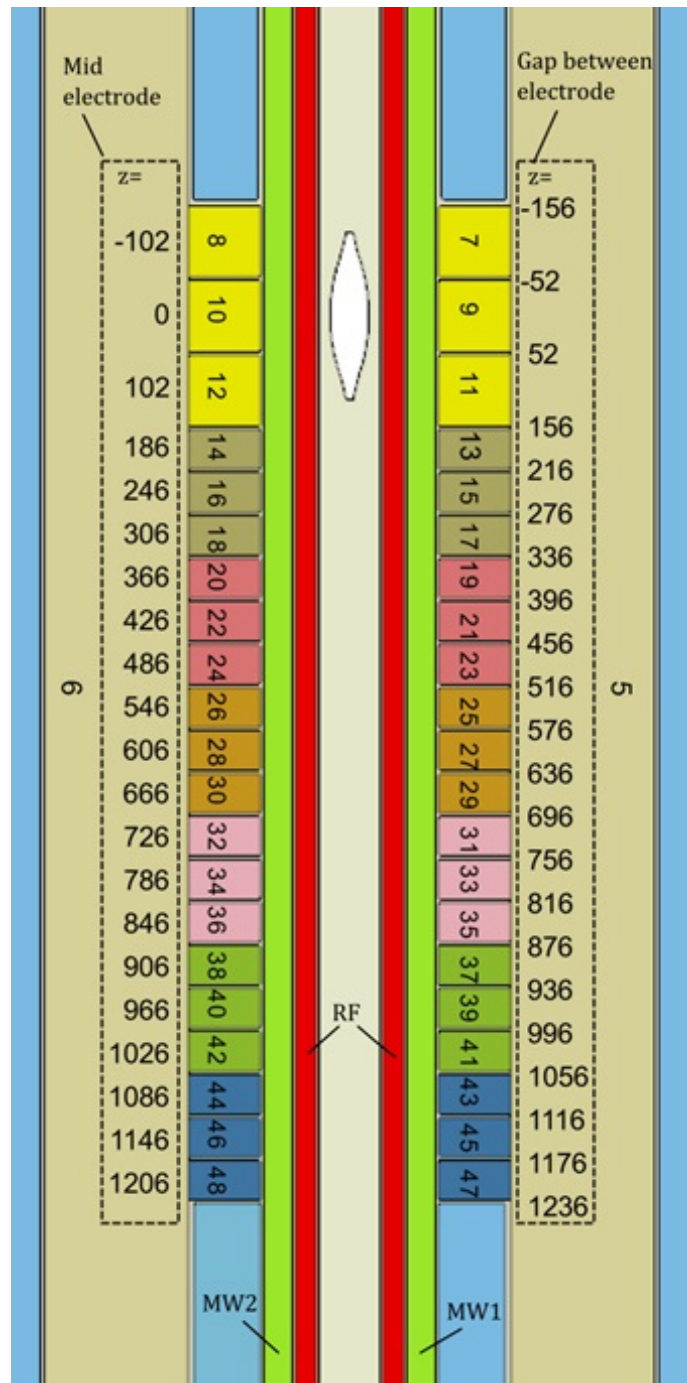


Figure 2.8: Dimensions and electrode IDs of the trapping region for a Microwave I trap. The z coordinates along the length of the trap correspond to the ion positions relative to the loading position. (Fig. from GTRI Microwave I Trap manual[4])

termine the voltage for each DC electrode. Set of files, named waveforms, are provided by GTRI for each of these functionalities. These are comma separated value (CSV) files in the following format:

Position	DC_{05}	DC_{06}	...
i_1	$U_{05}(i_1)$	$U_{06}(i_1)$...
i_2	$U_{05}(i_2)$	$U_{06}(i_2)$...
i_3	$U_{05}(i_3)$	$U_{06}(i_3)$...
...

Each file specifically determines the voltage for each of the DC electrodes for a given functionality at a given ion position along the z axis. Since Poisson equation is a linear equation, to scale the electric field created by these waveforms, we can simply scale all the individual voltages by the same amount. If we need to use different waveforms at the same time the linearity allows us to simply add them together. For the stray field compensation voltages, applying a waveform is equivalent to applying electric field of 1000 V/m to the ion. One can scale these voltages by multiplying a scalar weight to all the electrode voltages in the waveform table.

We used LabVIEW(TM) to develop a program that has a user interface that enables user to input the file path for all the waveform files and the scalar weights associated to them. An input is provided for user to choose the accuracy in position down to 100 nm . The accuracy provided in the waveform files is 6 μm . The program uses a linear interpolation to find the middle values for the desired accuracy.

In the next step, the software multiplies the electrode voltages by the weights given by user to scale them and add them together. The user is allowed to opt between fixed or position dependent weight. The fixed weight option uses one scalar weight provided by the user for all positions. If position dependent weight is selected, a CSV file must be provided by the user that contains some arbitrary positions and the weight associated to them. The program uses a linear interpolation to calculate the weight for the positions not given in the file.

This functionality helped us to solve the problem of shuttling the ion over certain problematic locations of the trap. We had the problem of losing the ion at these points. One of the points was where the ion leaves the oval shaped loading area. The borders between the optics were also problematic. We realised that the stray fields vary very fast near these points. To compensate for these fields and reduce micro-motion and ion heating, I added this capability to the program to accept position dependent weights for each DC compensation waveform and vary that dynamically while shuttling. We mapped the compensation voltages for every 25 μm and saved it in an input file for the program. That modification together with using stronger harmonic DC potential solved the shuttling problem.

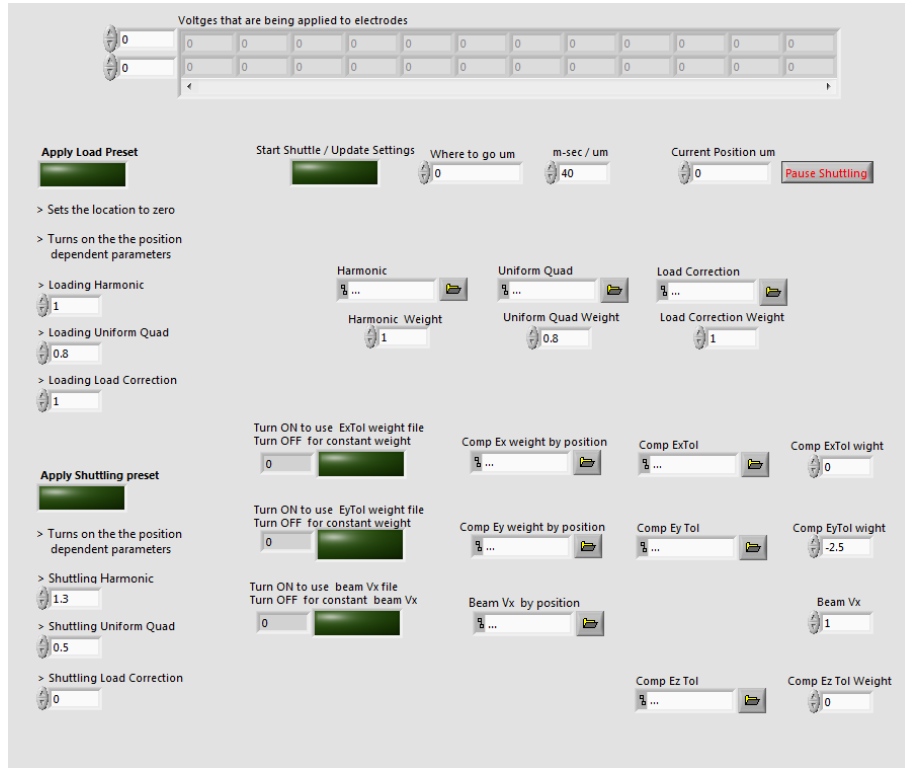


Figure 2.9: Screenshot of the LabVIEW program interface for controlling DC electrodes for shuttling and applying compensation fields. At the top part, the program displays the voltages that are currently being applied to the electrodes. Below that section, the user can enter a destination in the "Where to go um" field and a speed in "m-sec um" and start shuttling using the button "Start Shuttle / Update setting" to the left of those. The input fields at the bottom allows user to choose a file for each waveform and select between constant weight or position dependent weight. Left inputs are used to save two pre-sets for loading and shuttling and apply them when needed.

Fig. 2.9 shows a screen shot of the user interface of the program. To shuttle the ion around, the program gets a destination in μm from the loading spot and a speed of shuttling. Using current position, destination, accuracy and speed, program calculates the number of steps and the time for each step. Applying the calculated number of steps and the delay needed for each step, it smoothly moves the ion to the destination.

In this procedure lasers must also track the ion position. We use an Optics In Motion(TM) OIM5001 fast steering mirror that is controlled by a DAC (Digital-to-Analog Converter) system. We measured the x and y voltage needed to position all lasers at the loading zone ($0 \mu m$) with the correct height and at the end of the trap ($1086 \mu m$) with the correct height. For the rest of the positions the program uses a linear interpolation to calculate the voltages. The user is also allowed to provide a position dependent file for slight modification of laser positioning.

The program allows user to save two preset lists of input values for trapping and shuttling. By the click of a button, the program changes all the parameters to the saved values to make the voltages ready for trapping a new ion or shuttling it around.

After long period of using a trap, depositing neutral Yb on the back side of the loading zone creates vertical fringe fields around the exit point of the loading zone. Depending on the position of the coating, the field can be upward or downward. This created a problem for us in shuttling the ion outside the loading zone, after two years of using the same trap. We solved this problem by applying a 1200 V/m upward electric field in the loading zone and gradually reducing it to 0 at $200 \mu\text{m}$ away from the loading point.

2.2.2 RF Electrodes and RF Voltage Generation

For trapping, this trap needs a RF voltage between $80\text{--}200 \text{ V}$ and a frequency of $25\text{--}30 \text{ MHz}$. To supply this RF voltage we use a HP 8647 RF generator that runs at $+8 \text{ dBm}$ and the output goes through a -29 dB attenuator before being fed into a $+40 \text{ dB}$, 10 W high power RF amplifier. The attenuator is used to make sure that even when the maximum power on the generator is used, the final voltage remains below 200 V . The output of the amplifier goes to the antenna of the a helical resonator shown in Fig. 2.10 . This antenna induces an RF voltage on the inner coil which goes to the chip.

The helical resonator acts as a transformer to keep the supplied RF power to a minimum. It consists of a copper cylinder that houses a one loop antenna and a coil and a capacitive divider. The RF source is connected to the antenna and induces a current on the coil. The outer cylinder is a copper tube that was sand blasted to remove contaminations. A BNC plug mounted on a adjustable lid is the input to this resonator and is connected to an aluminium antenna. The inner coil is made of copper wire and is connected to the grounded housing tube from one side and to the vacuum RF feedthrough from the other side. The adjustable lid is used to find the optimum position for the antenna to reach maximum coupling. The coupling efficiency is optimised by minimising the amount of RF back reflection to input. Changing the position of the antenna changes the resonant frequency therefore the antenna position and RF frequency must be changed iteratively to reach the optimum coupling.

The design of the resonator is based on the design and equations in [71]. For a desired resonant frequency, quality factor and resonator length, the equations determine number of turns, coil length, winding pitch, and the sizes of all the other conducting components. For a given resonant frequency, these designs can reach quality factors of a few hundreds to a thousand in a compact resonator. Capacitive load reduces the resonant frequency and the quality factor. To replicate the real capacitive load we used a bare vacuum feedthrough during the tests of coupling efficiency and quality factor. This lacks the capacitance of the chip itself therefore the final test numbers are slightly different from the operating values

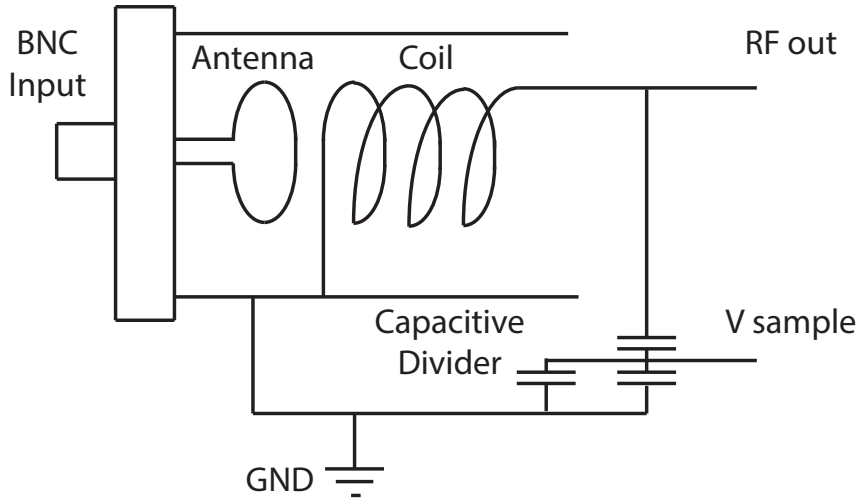


Figure 2.10: Schematic of the helical resonator used for RF input of the trap. Capacitive divider is used to sample the output voltage.

at the trap. The length of the inner coil is the main parameter that we change to achieve the desired resonant frequency. The test quality factor for our resonator was 95 but when it is attached to the trap the quality factor drops to 80. The resonant frequency for the test condition was 27.1 MHz but it is 25.7 MHz when it is connected to the trap.

The helical resonator for the chip trap includes a capacitive divider that is used for monitoring the trap RF voltage. The ratio of capacitance in this divider is 200:1 but the practical voltage ratio is 530:1. This is partly because of the input capacitance of the oscilloscope and the stray capacitance. Our experience shows that this ratio changes dramatically with slight changes in position of components of helical resonator so care must be taken in measuring a reliable ratio. These changes in the reading are because of parasitic capacitance and inductance. We read 0.15 V peak to peak from the monitoring output therefore we are applying 80 V peak to peak to the trap RF electrodes. There was a worry that the nano-structuring of the ground electrode for the new optics may lower the RF breakdown voltage but based on our experience it is the same as the standard trap.

2.3 Diffractive Mirrors

Currently all the basic tasks of quantum information processing with ions have been demonstrated with small numbers of ions[31, 32]. The highest number of entangled ion created has been only 14 [39]. This number is theoretically limited to about a hundred

ions[37] because of spontaneous decay, laser phase coherence and ion heating[38]. The future of this field depends on scaling the number of ion qubits under control and that is why recently the interest of researchers turned towards micro-fabrication of ion trap technologies. In recent years, micro-fabricated trapping technology has improved a lot[44] and some researchers are working on scalable optical interfaces to use with these modern traps. Scalability in this context is the ability to increase the number of ions and optics without affecting the performance of the optics and without adding too much technical complexity.

Light collection efficiency directly impacts the time needed for the read-out and remote ion entanglement. To collect the maximum amount of light the optic must cover large fraction of total solid angle around the ion. As an example, in a collaborating project between Massachusetts Institute of Technology and Max Planck Institutes, researchers manufactured a trap with a built in parabolic mirror that covers 80% of the solid angle [56]. To scale the number of ions, the prospect is to have the ion density of about one ion in every $100 \mu\text{m}$ for 1D linear traps. 2D traps have the potential to have even higher densities. At that scale the only way to cover more than 10% solid angle is to place the optic at a distance smaller than $100 \mu\text{m}$ to the ion. If we place a dielectric optic this close to the ion, charging from photo-ionisation starts to build up on the optic very quickly and makes trapping impossible. Transparent conductor coatings, like indium tin oxide (ITO), are a solution for this problem but might not be practical for all designs. The problem with metal optics, if they are not part of the trap, is that they change the trapping field configuration. Integrated mirrors do not have any of these problems because they are integrated into the original electrodes of the trap. They also do not restrict optical access of the trap. These characteristics enable us to increase optics density beyond any other competing technology. This design does not need optical alignment and is robust against thermo-mechanical movement and stress during bake-out. The fabrication process uses standard lithography and is robust against ion trap bakeout. The performance of these optics is comparable to advanced non-scalable technologies.

We demonstrated that a large fraction of the collected light by this optic can be coupled into a single mode fibre. Single mode fibre coupling of the ion light is important for remote entanglement and quantum communication. Single mode fibre coupling efficiency, η_{SM} , depends both on the free space collection efficiency, η , and the beam quality, M^2 (for definition of M^2 see section 4.2). A rough estimate is that $\eta_{SM} \approx \eta/M^2$. We demonstrated that the light collected with these optics have M^2 values close to unity and large percentage of the light can be coupled into a single mode fibre without additional aberration correction. In chapter 6 we demonstrate that we can couple 71(5)% of the collected light into the single mode fibre which is equivalent to coupling of 4.1(6)% of the total ion light into the single mode fibre.

As another method to demonstrate the imaging quality, we showed that images cap-

tured with the diffractive mirrors are close to the diffraction limit (section 4.4) and this is another reason to show why these optics are ideal for single mode fibre coupling (section 4.3).

To manufacture theses integrated diffractive mirrors, a joint project was defined between our team at Griffith University and Quantum Information Systems group at the Georgia Tech Research Institute (GTRI). The project was funded by Intelligence Advanced Research Projects Activity (IARPA), Griffith University and Australian Government. M. Ferstl at the Heinrich-Hertz-Institut of the Fraunhofer-Institut fur Nachrichtentechnik in Germany performed the step that needed electron beam lithography.

2.3.1 Theory of Diffractive Mirrors

A collimated beam has a flat phase front. What a conventional focusing curved mirror does is that it focuses the light by changing the phase front of a beam so that all the different parts of the beam become in phase at our desired focus point. This phase shift can be written in the form $2n\pi + \Delta\phi$. Here $\Delta\phi$ is between 0 and 2π . n might be different at different positions but it does not have an effect on the focusing procedure. In design of diffractive mirrors we set n to zero and impose periodic $\Delta\phi$ from 0 to 2π to the phase front.

When a beam reaches the focus point from an off-axis distance r (Fig. 2.11) it has travelled a distance equal to $\sqrt{r^2 + f^2}$ (f is the focal length). Thus the phase difference between the on-axis beam and this beam is:

$$\Delta\phi = (\sqrt{r^2 + f^2} - f)k \quad (2.14)$$

where $k = 2\pi/\lambda$ is the wavevector and λ is the wavelength of the light.

We need to change the path length to eliminate this phase difference. If $\Delta\phi$ is greater than 2π we can deduct multiples of 2π from the phase shift without changing the effect of phase shift (or equivalently if the difference in path length is greater than λ we can deduct $m\lambda$ from the path length difference). To eliminate this phase difference and make beams in phase at focus, we can increase the height by $\Delta h = \sqrt{r^2 + f^2} - f$ at r (This must be done by deducing multiples of λ when Δh is grater than λ). This means that at radii associated with 2π phase difference, the height starts at zero and increases to λ at the next radius associated with 2π phase shift and then drops abruptly to zero and continue increasing up to the next ring. These rings are located at:

$$r = \sqrt{2n\lambda f + n^2\lambda^2} \quad (2.15)$$

This creates a pattern shown in Fig. 2.11.

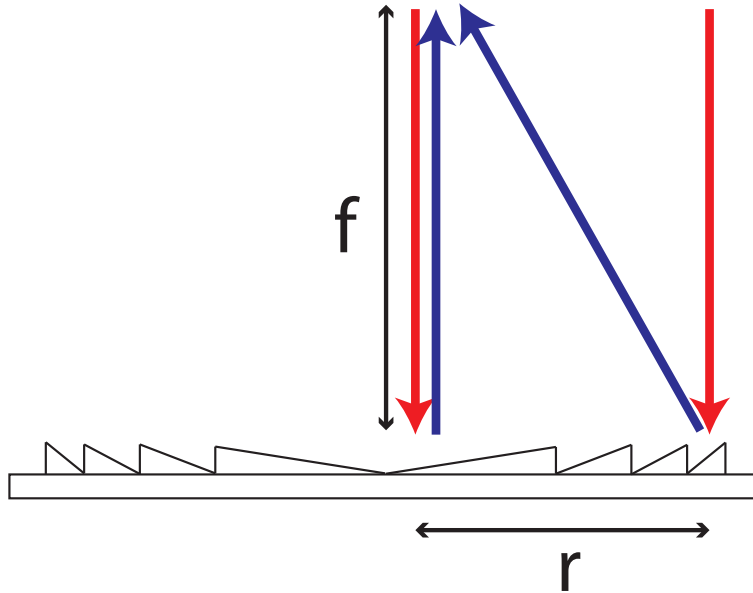


Figure 2.11: A diffractive mirror with 2π cycles. Red arrows are incoming beams at the centre and at the offaxis distance r . Blue arrows are reflected beams that both go to the focal point.

Unlike curved mirrors, different parts of a single curved phase front created by diffractive mirrors is from different flat phase fronts incident on the mirror. This is not a problem in the steady state regime but can be a problem in pulsed regime if the pulse length is of the order of this time domain effect. The maximum time difference, Δt , can be calculated from the path difference between the beam coming from the center of the mirror and the beam coming from the edge of the mirror, Δl :

$$\Delta t = \frac{\Delta l}{c} = \frac{\sqrt{r^2 + f^2} - f}{c} \quad (2.16)$$

Where c is the speed of light. This value is very small when mirror size is small. For example for our mirror with focal length of $59.6 \mu m$ and maximum radius of $150 \mu m$, $\Delta t = 3.4 \times 10^{-13} s$. This can only cause a problem if the pulse length is of the order of a picosecond or shorter.

In practice it is hard to fabricate the smooth height pattern calculated for the diffractive mirrors. In the small angle limit where the scalar diffraction approximation is valid, approximating the continuous pattern even with two levels can lead to about 30% diffraction efficiency and 4 level approximation can increase the efficiency up to 70%.

In our group we have used diffractive lenses to collect ion light[61]. The advantage of our new method of using mirrors is that for moderate NA's (< 0.5 NA) maintaining high diffraction efficiency is much easier with mirrors. Interference effects lowers the diffraction efficiency at moderate angles in diffractive lenses. This effect is absent in diffractive mirrors. For mirrors with high NA's(> 0.5 NA), the scalar approximation is not valid anymore and vector diffraction must be used. In this regime, the reduction in phase contrast for step profile reduces the diffraction efficiency by a considerable amount. Another effect that becomes important in vector regime is the polarization dependence of the diffraction efficiency. Using a vector method, it is possible to optimise the profile to maintain diffraction efficiency of 95% even for solid angle coverage near 50%[72].

2.3.2 Design of the Diffractive Mirrors

In this project we integrated diffractive mirrors into the middle ground electrode of the Microwave I trap. Fig. 2.12 Shows a microscope image of Integrated Diffractive Mirror trap (IDM trap) taken by GTRI. The array of optics consists of 5 collimators and 3 other test optics. Collimators collect ion light, collimate it and send it out of the vacuum chamber. We also have a collimator at the loading zone which is located at the most left side of the trap. This collimator is $200 \mu m$ long. Most of the area of this collimator is etched away to create the loading zone (oval shape black area on the left side of the chip in Fig. 2.12). We demonstrated that even with this highly modified mirror, imaging is possible and aberration is not dramatically high. On the right side of the loading zone there is a small area left for logo and labelling and after that the main array of optics starts. The length of each optic is $127 \mu m$ to match the commercial v-groove fibre connectors. The width of the optics are the same as the middle ground electrode which is $80 \mu m$. These optics cover about 13% of total solid angle around the ion. The collimators in different designs have a focal length equal to the nominal ion height, $58.6 \mu m$, or equal to $58.6 \pm 1 \mu m$ or $58.6 \pm 2 \mu m$. The design is wavelength dependent and for this case the design wavelength is $369.5 nm$ which is the wavelength of the main cooling transition for Yb^+ ion. The first test optic is a self imager. This optic focuses the ion light on itself. This works as a half cavity and designed to investigate quasi-cavity effects such as change of the spontaneous emission lifetime [73]. The second test optic is a laser addresser. This optic focuses the collimated laser light incident normally at the chip surface on an ion. This improves the area efficiency of laser addressing comparing to addressing parallel to the chip surface. We also have a cross imager optic. If we place two ions on each side of this cross imager, their light will be focused on each other. This optic is for testing photon mediated interactions between two ions.

The design of the diffractive mirrors comprised of 5 main steps:

1. Ray tracing design

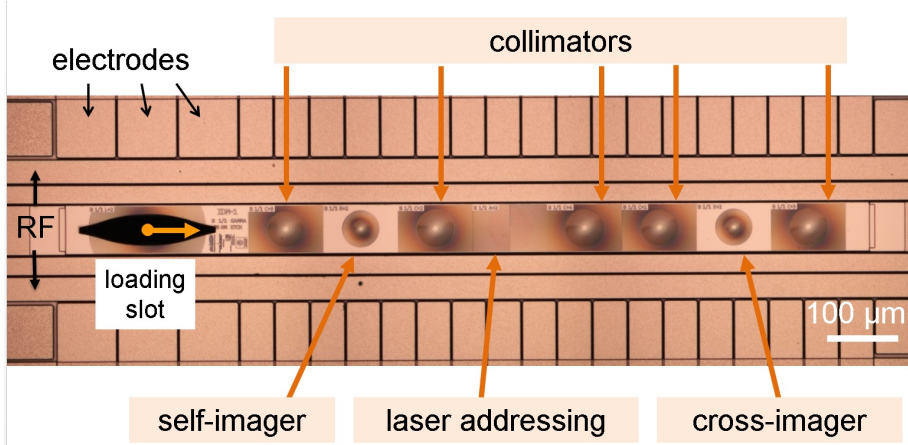


Figure 2.12: Microscope image of the integrated diffractive mirror trap taken by GTRI and layout of the array of the optics.

2. Grating structure design
3. Single-optic mask generation
4. Array-level mask generation
5. Wafer layout design

All the design tasks were performed by David Kielpinski at Griffith University. For each of the optics ZEMAX OpticStudio was used to model a realistic ray optic tracing and find the best phase function to minimise the aberration. Designs are aberration free and their field of view is $2 \mu m$. The effect of off-conjugate imaging was also simulated to evaluate the effect of fabrication imperfections. Simulations show that the error in ion height can have the largest contribution to aberration.

The next level of fabrication was to create 2-level, 4-level and hybrid step profiles using the phase functions obtained in the previous step. The 2-level design approximates the phase profile with a two level profile with the height of $90 nm$. In the 4-level design, steps are $45 nm$ high and have equal widths. The hybrid design uses 4 levels for the inner rings with widths greater than $200 nm$ and 2 levels for the outer rings with widths smaller than $200 nm$. For all the designs, lateral features smaller than $100 nm$ were removed. To optimise the diffraction efficiency of the step profiles we used a genetic algorithm. GSolver and GD-calc was used to calculate the diffraction efficiencies.

GSolver solves Maxwell's equations within an arbitrary periodic grating structure at the interface of two semi-infinite half-spaces: the superstrate, and the substrate. It is a visual software that uses rigorous coupled wave analysis and modal analysis to evaluate diffraction efficiency of arbitrary gratings. GD-calc is a MATLAB-based system simulation

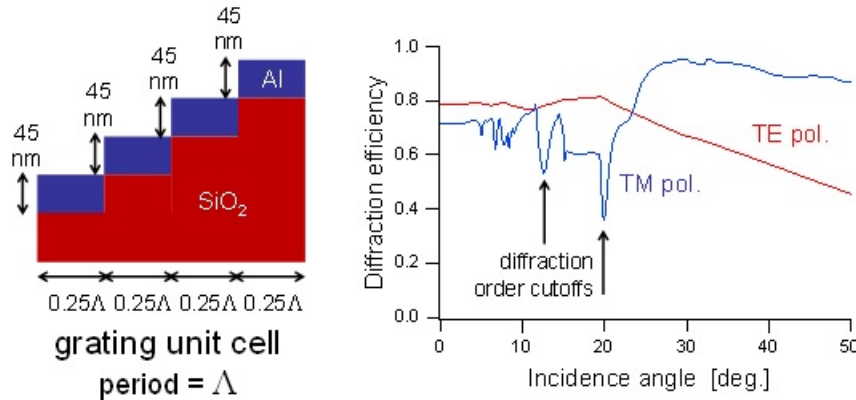


Figure 2.13: Left: Schematic of the design sizes for the 4-level grating structures. Right: Simulated diffraction efficiency as a function of the incidence angle of light. (Figure courtesy of David Kielinski)

that also uses rigorous coupled-wave vector diffraction analysis to calculate diffraction efficiency. These two independent solvers were used to make sure that diffraction efficiency calculations are accurate and consistent. The final step in diffraction efficiency evaluation was to add constraints in fabrication with lithography to calculate a realistic diffraction efficiency.

Fig. 2.13 shows a schematic of a 4-level profile and its calculated diffraction efficiency. The steps have equal widths and heights and the diffraction efficiency is between 60-80%. Simulation shows that if we use 2-level design with the height of 90 nm, we have 30-40% diffraction efficiency and for hybrid design we have about 40-60% efficiency.

Next step in designing was to create the masks. To account for fabrication limitations we used different types of designs in each mask. Masks were saved in PNG format. Nominal ion height in Microwave I Trap is $58.6 \mu m$. This number is inferred using Poisson's equation simulation but was never confirmed experimentally by GTRI. Because of optical aberrations in high NA optics, our design tolerance is only $1 \mu m$. With deviances greater than $2 \mu m$, the aberration becomes significant. Because of this problem we designed arrays that contain collimators that have focal lengths equal to or 1 or $2 \mu m$ above or below the nominal ion height. In general it is possible to use DC fields to push the ion up or down but pushing ion away from the RF node increases the micromotion and makes ion unstable therefore we tried to avoid using this method as much as possible. We designed four different masks and labelled them α, β, γ and δ . These designs have different sets of focal lengths for the collimators. Currently we use γ design which contains collimators with focal lengths equal to nominal ion height or $+1, +2$ and $+4 \mu m$.

To fabricate mirrors and electrodes, a separate lithographic processes is used and this

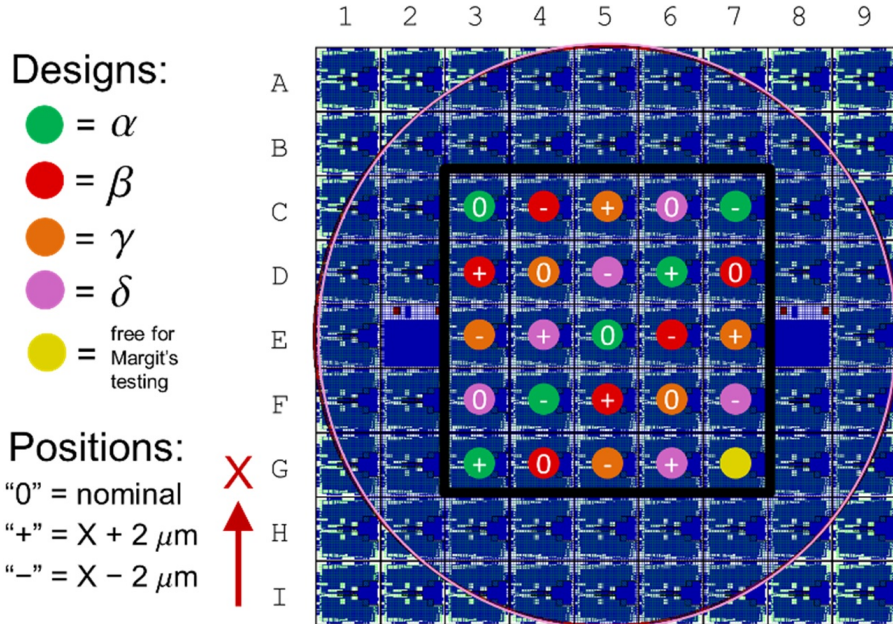


Figure 2.14: Complete layout of a single wafer, incorporating defence against both ion height errors and lateral offset errors.(figure courtesy of David Kielpinski)

may lead to an offset between ion poison and focal point in the plane parallel to the trap surface. Offset along the RF rails is not a problem because it can be fixed with DC fields without any side effects but if we push the ion laterally we increase the micromotion of the ion. Even though this offset was predicted to be less than $1 \mu m$, we still tried to defend against this possible problem by having lateral offsets in some of our array designs.

We combined all these different array designs in a wafer to create the final mask for fabrication. This mask is shown in Fig. 2.14.

2.3.3 Fabrication of the Diffractive Mirrors

GTRI and Fraunhofer Heinrich-Hertz Institute (FHHI) performed the fabrication of the integrated diffractive mirrors. The process needed a work flow that would match the capabilities of both institutes. The coordination and supervision of the process flow were undertaken by David Kielpinski at Griffith University. FHHI had some design requirements and material characteristics to be able to perform a fine task of fabrication of diffractive mirrors. We had to decide at which step of the original fabrication process we wanted to perform the intervening step of etching the mirrors. After consulting with both institutes the decision was that GTRI should build an initial three level substrate and send it to Germany for electron lithography and leaves the rest of the process until after receiving the altered substrate back.

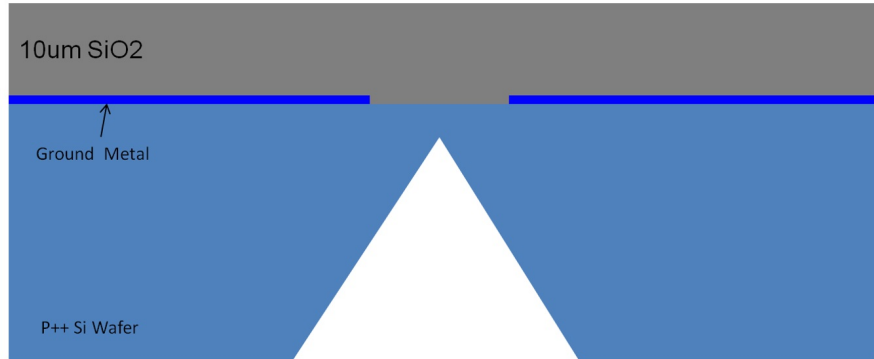


Figure 2.15: Representative image of the substrate prepared by GTRI to send to Fraunhofer Institute (details in text) (image courtesy of David Kielpinski)

This substrate included a *Si* wafer that had a ground metallic layer on top of that and at the uppermost level there was a $10 \mu\text{m}$ SiO_2 layer (Fig. 2.15). The next step was sending this substrate to FHII for lithographic etching of the mirrors. FHII required 1.5-2 μm alignment marks with vertical side walls and uniform oxide thickness with RMS roughness of $< 5 \text{ nm}$. The original roughness of the oxide layer was of the order of 10-20 nm . GTRI performed a chemical mechanical polishing -which is not part of their original fabrication process- to reach the roughness of 5 nm . Before starting the fabrication process some preliminary samples were sent to FHII to confirm the suitability of the characteristics of the substrates.

After transferring the substrate to FHII, they started the fabrication process of the mirrors with electron lithography. They tried to fabricate 2-level, hybrid and 4-level designs. The fabrication of 2-level and hybrid designs were successful but they concluded that feature sizes are too small for 4-level design for the alignment tolerance required. We currently use the hybrid design which has 4 steps for big features and 2 steps for small features. FHII performed an AFM microscopy and confirmed that the step sizes are within 5% of the nominal size (45-50 nm). A representative image of the outcome of this process is shown in Fig. 2.16.

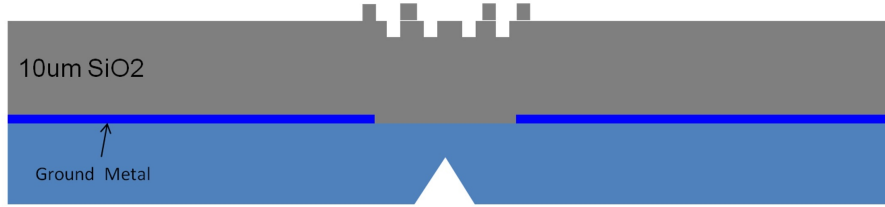


Figure 2.16: Cross section as delivered by FHII after diffractive mirror fabrication (mirror features are not to scale) (details in text) (image courtesy of David Kielpinski)

At this point GTRI had to coat a metal layer on top of the oxide layer but they had to consider some complications that could have arisen during the process:

1. The most important challenge was that the coating may wash the features out.
2. This metal had to act as ground electrode and if after fabrication it was not electrically connected it would not perform its role.
3. The features could have been damaged during the coating of surrounding thick electrodes and had to have some protection during this process.
4. Mirror's layer and other thicker electrodes had to end up at the same height at the end of the process.

In deciding the ideal metal layer thickness, both feature size and connectivity plays a role. After coating the metal layer, ridges become thicker and trenches become narrower and using too much metal washes out the whole features. On the other hand using too thin of a metal layer may affect the electrical connectivity. After some tests 100 nm of metal was found to be the best thickness. This thickness still changes the size of ridges and trenches but this had already been considered and countered in the mask design. Figure 2.17 shows a microscope image of the features before and after metal deposition.

After this step, surrounding oxide substrate was plasma-etched to match the height of mirrors with the thicker electrodes that would be deposited later (Fig. 2.18a). An oxide layer was also deposited on the mirrors to protect them during subsequent processing (Fig. 2.18b)

In that stage of the process DC and RF electrodes were deposited and ICP aluminium etch was used to cut the metal and separate different electrodes (Fig. 2.19a). Then a 1 μm oxide layer was used on the outer side of the electrodes to insulate these DC electrodes from the outer ground electrode that would be deposited at that position (Fig. 2.19b). At this point the final etching of the oxide layer for making the gap between the electrodes and making the loading zone hole was performed. A photo-resist was used to protect

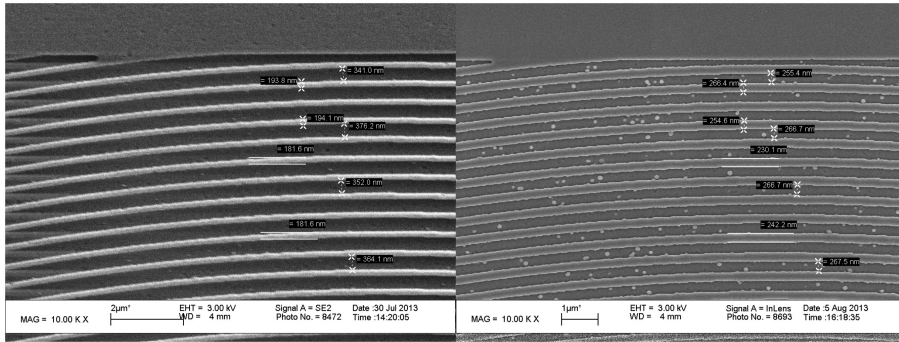


Figure 2.17: Small diffractive mirror features before (left) and after (right) metal deposition taken by GTRI.

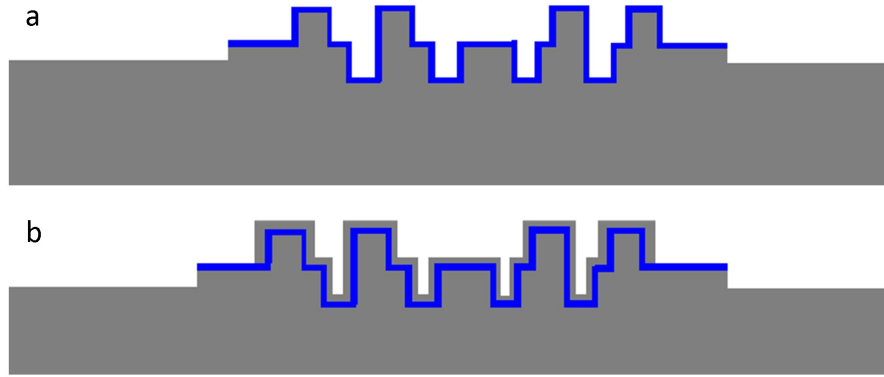


Figure 2.18: a. The wafer after plasma etch b. Diffractive mirrors with oxide protection layer (details in text) (image courtesy of David Kielpinski)

mirrors from etching. Finally to finish the fabrication process the protective oxide layer was removed (Fig. 2.19c).

Not all the attempts of fabricating a completed chip from patterned substrate were successful but GTRI could fabricate a number of working ion trap chips from patterned substrates. An Image of a successful binary and hybrid mirror fabrication is shown in Fig. 2.20. Figure 2.21 shows a SEM microscope image of a completed 2-level mirror taken by GTRI. They also imaged a completed chip using a dark-field microscope shown in Fig. 2.22.

To investigate the potential ways of improvement in fabrication, nano-imprinting was found to be an attractive option[74]. It can solve multilevel fabrication problems, trap misalignment issues and feature size limitations that we had in electron lithography. The only possible problem is that the pressure that it needs for imprinting is 1 GPa which is on the order of fracture stress for silicon wafers. At this moment this is just a plausible idea and an extensive research is needed to make it practical.

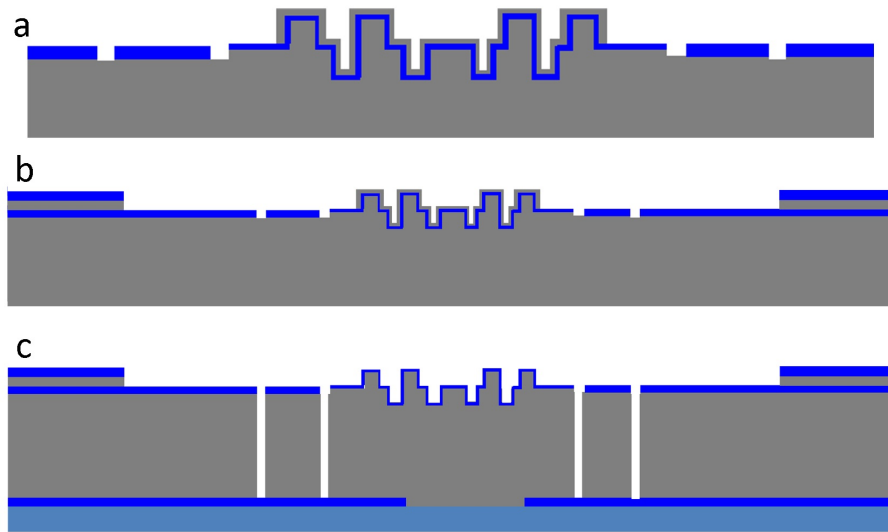


Figure 2.19: a. DC/RF metal deposition and etch b. Top metal deposition and etch c. Final device cross section (details in text) (image courtesy of David Kielinski)

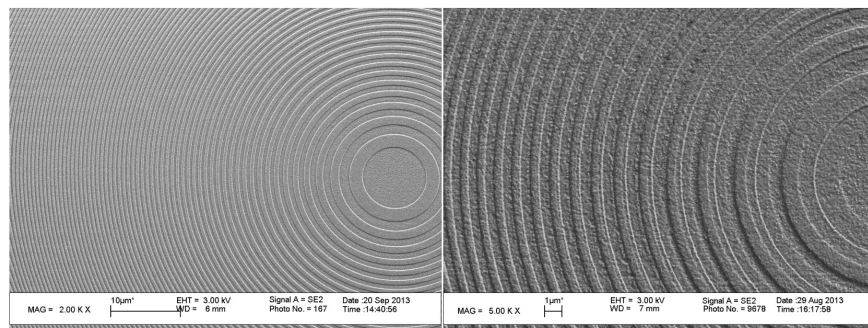


Figure 2.20: Binary (left) and hybrid (right) diffractive mirrors after completed ion trap fabrication. (image taken by GTRI)

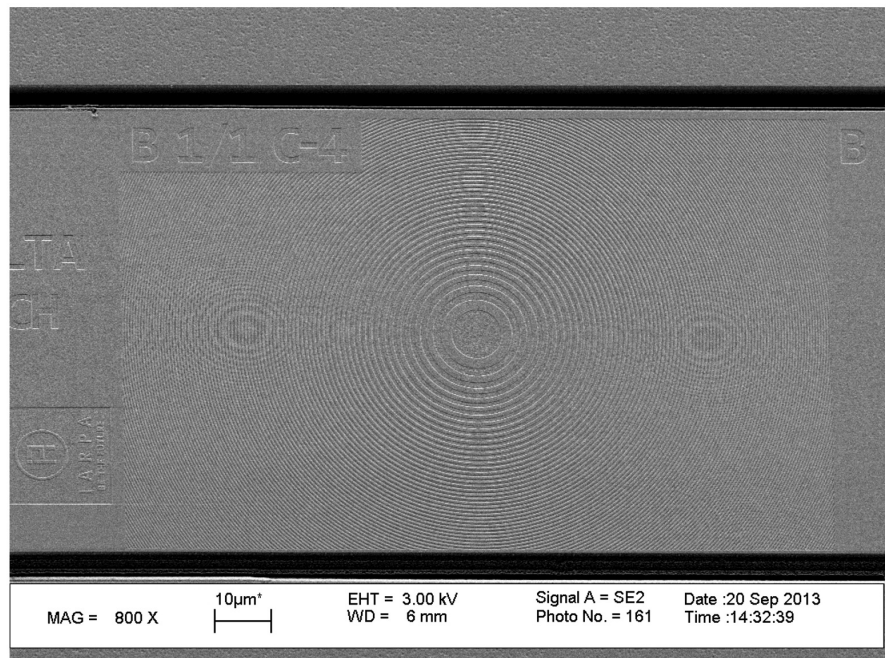


Figure 2.21: Full Binary DOE on a completed ion trap (Image taken by GTRI)

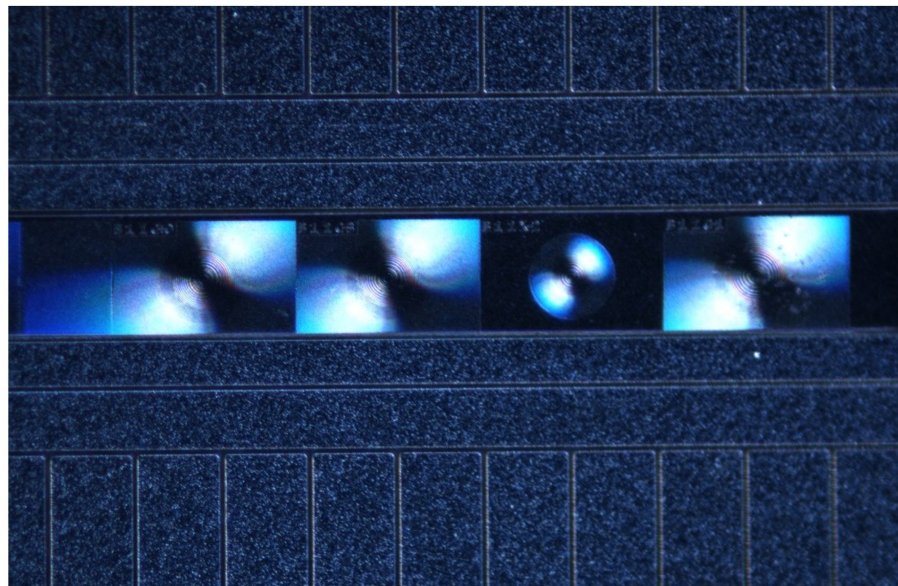


Figure 2.22: Dark field image of DOE's on a completed ion trap. (image courtesy of GTRI)

2.3.4 Characterisation of the Diffractive Mirrors

This section covers the preliminary tests performed by GTRI and our group on the Integrated Diffractive Mirror chip. The main characterisation of imaging and light collection will be discussed in chapters 4 and 6 .

GTRI did the initial tests on the new chip. The first test chip was a hybrid one. The ion used by GTRI for testing was Ca^+ ($\lambda = 397 nm$) so the wavelength was slightly different from the design wavelength of $370 nm$. The first optic that they tested was the self-imager. This test was as straightforward as moving the ion over the optic and capturing the ion image next to the ion itself (Fig. 2.23). Images show that there is a lateral displacement between the ion and its image. This is due to the mismatch of less than a μm between mirror fabrication and electrode fabrication. Using a lateral DC field they showed that this mismatch is fixable (Fig. 2.24). Because of the nonlinear EM gain in their EMCCD camera, the relative brightness of the image cannot be used to estimate the collection efficiency of the optic.

To test the collimator, they used a reflective objective to image the ion. As shown in Fig. 2.25, this objective has an annular aperture and the center of the objective is blocked by the second mirror. This means that the second mirror will block the collimated beam in the ideal situation where the ion is at the center of the collimator and both optics have a common axis. By pushing the ion to the side they captured the image shown in Fig. 2.25b. This is taken with the iris closed to its minimum aperture and depth-of-field is large enough that the blocked area is roughly visible in the center of the image in Fig. 2.25a.

Fig. 2.26 shows two images of the ion with iris open (a) and iris closed(b). The one with the iris open collects, the collimated light, the direct light from the ion and the scatter from the chip. In this mode, it is hard to distinguish the light that is coming from the collimator. With the iris closed the numerical aperture becomes very small for direct light and the scatter but has minimal effect on the narrow collimated light therefore a clear image of the collimated beam can be captured that is shown in Fig. 2.26b.

To measure the enhancement in light collection form the collimator they used a PMT to count the number of photons for different ion positions both with iris open and closed.

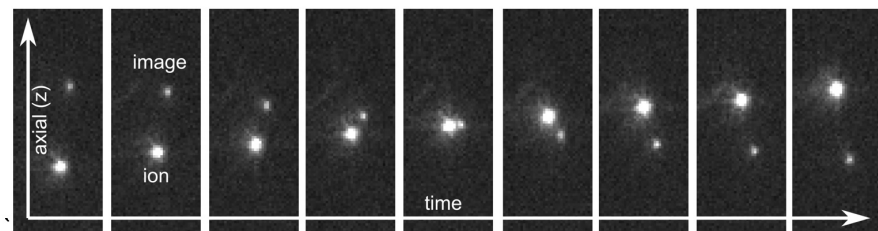


Figure 2.23: Ion transport image over the self-imager taken by GTRI

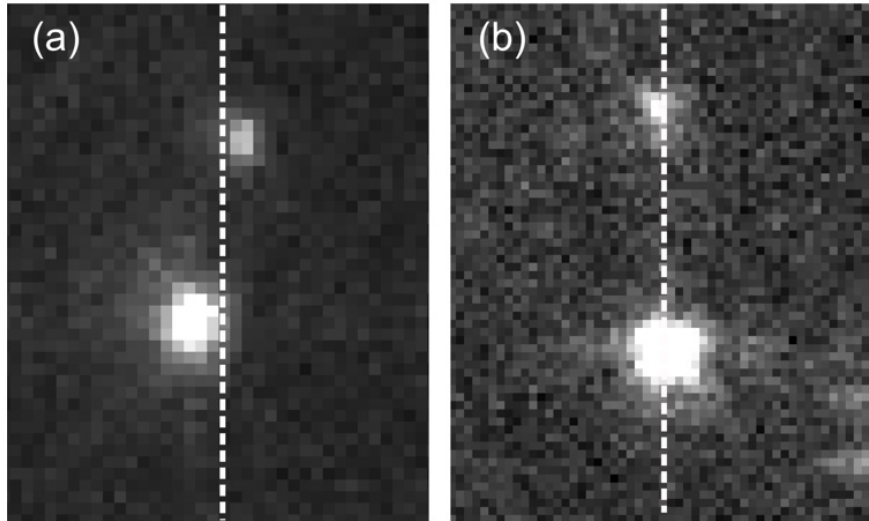


Figure 2.24: (a) Ion and image alignment when micromotion nulled. (b) Applied lateral electric field pushes the ion to the right, with a corresponding movement of the image to the left. (image taken by GTRI)

In both cases lasers track the ion position to keep fluorescence constant. The background scattered light is also measured without ion for both cases. Fig. 2.27 shows the background corrected data for different positions. The graph shows that with the iris open, the number of photons in a fixed time interval is 0.8. For the positions that collimated light is also being collected this number increases to maximum of 1.8. The second graph shows that closing the iris suppresses almost 90% of the direct light collection but has almost no effect on the collimated light. Even though the center of the collimator located at $235 \mu m$ (nominal position marked on the graph), the maximum light collection happens around $245 \mu m$. This happens because of the occluded objective that GTRI used and does not mean that the center of the collimator is at $245 \mu m$.

Data on the graph in Fig. 2.27 suggests that the collection for direct light is 0.8 and for mirror is 1 in a fixed interval. Knowing that the numerical aperture (NA) of the objective is 0.28, they estimated NA of 0.31 or collection of 2.5% for the diffractive mirror. Our later rigorous characterisation shows that this collection is 5.8% (see chapter 6).

After finishing the initial tests GTRI sent the tested trap to Griffith. This trap was damaged during transport and some DC electrodes on the side that are used for shuttling were shorted. GTRI sent us a special set of potentials that took into account the shorted electrodes. We used a 2X amplifier for our operations because our standard DAC system supplies $\pm 10V$ but some electrodes needed $\pm 20 V$.

The next step for trapping was to prepare lasers. We were sure that the frequencies of the lasers were correct because we trapped an ion in our old trap, using the same lasers.

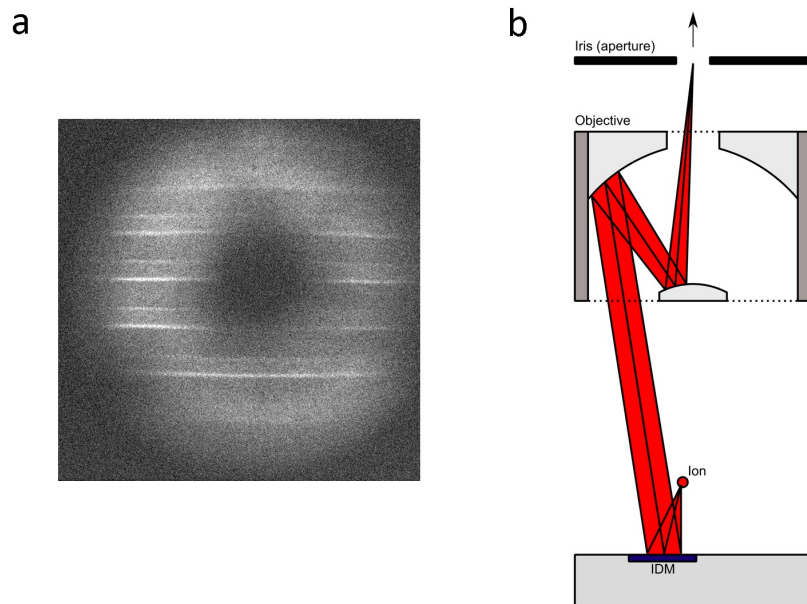


Figure 2.25: a. With the lens aperture closed, the depth-of-field is large enough that the central obscuration of the objective is visible as a dark inner region. The bright horizontal bands are patterns on the trap surface. b. Rough diagram of light collection from IDM with the reflective objective. The collimating optic collection efficiency data were taken such that the light would both be collected by the lens and pass through the iris when the iris was closed. (image courtesy of GTRI)

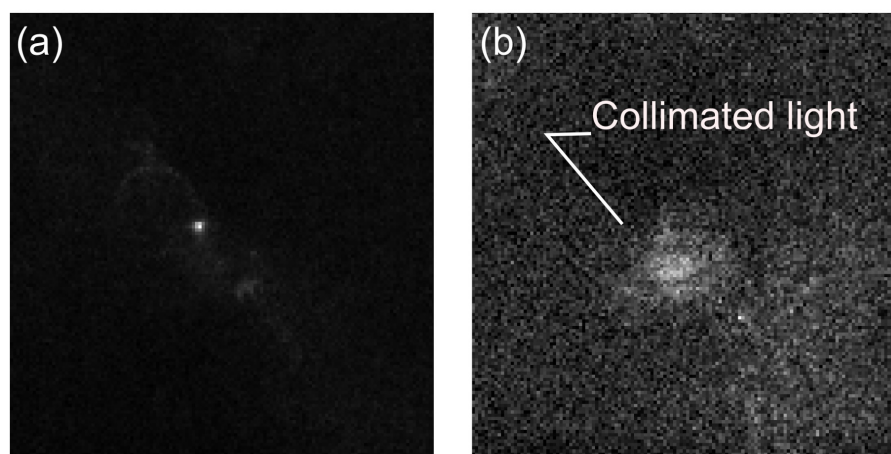


Figure 2.26: a. Direct imaging (iris full open) and b. Collimated light imaging (iris closed to minimum) of the ion. (image courtesy of GTRI)

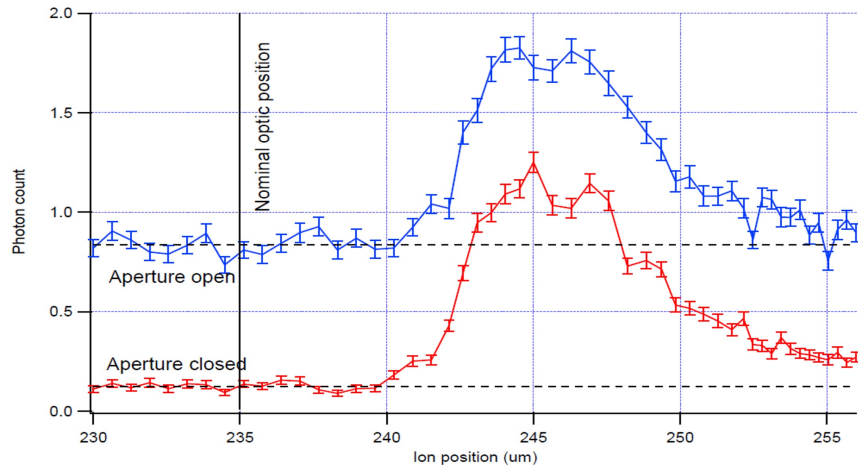


Figure 2.27: PMT counts vs. ion position over the collimating optic for the lens aperture (iris) fully open and for the aperture at minimum (closed). The dashed lines are guides for the eye, showing the photon counts for the direct light from the ion, as extrapolated from the measurements in left wing of the plot. Both measurements have had position dependent backgrounds (measured separately without an ion) subtracted out. (graph by GTRI)

To set the beam pointing we had to preset the laser position and angle and then scan the beam position around the preset point. The first step in preset was to make sure that the beam is parallel to the surface of the chip. We did this by checking the laser beam on a card where it exits the back window. When the beam is too angled towards the surface, a clear reflection of the laser off the surface can be seen on the card. When the beam is angled up, pushing the beam towards the surface cuts the laser in half but no reflection can be seen. When the beam is parallel to the surface, hitting the chip creates a diffraction pattern on the card. When the diffraction pattern has the maximum brightness, the center of the beam is at the chip surface. From this point we need to move the beam up by about 50-60 μm to center it at the ion. The positioning parallel to the surface was done by setting the beam to the center of the oval shape loading zone hole. This was performed by looking at the camera image taken from the top.

It is important that the beam does not hit the surface of the trap while RF voltage supply is on. If this happens the photo electrons ejected by high energy UV photons hit the exposed silicon dioxide and charge it. This build up of charge over time creates a stray field that makes trapping impossible. A wait time of several hours is needed for the charge to dissipate.

Supplying the RF voltage was the next step. We started with RF pk-pk voltage of 180 V and frequency of 23 MHz but our attempts were unsuccessful. By changing the RF frequency to about 26 MHz and using the same amplitude, we managed to trap our first

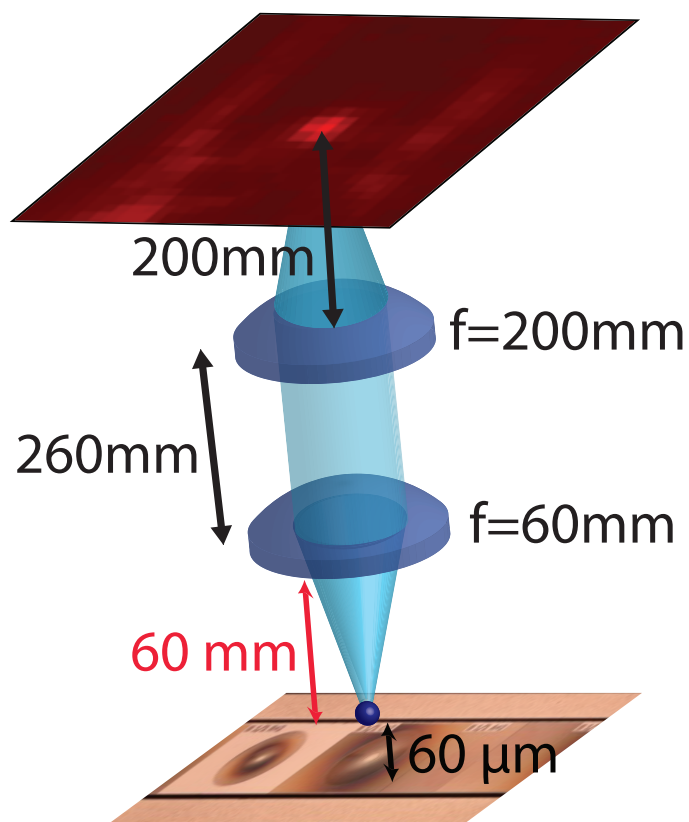


Figure 2.28: Schematic of bulk collection optics. The first lens collects and collimates the ion fluorescence and the second lens focuses the collected fluorescence onto the camera chip.

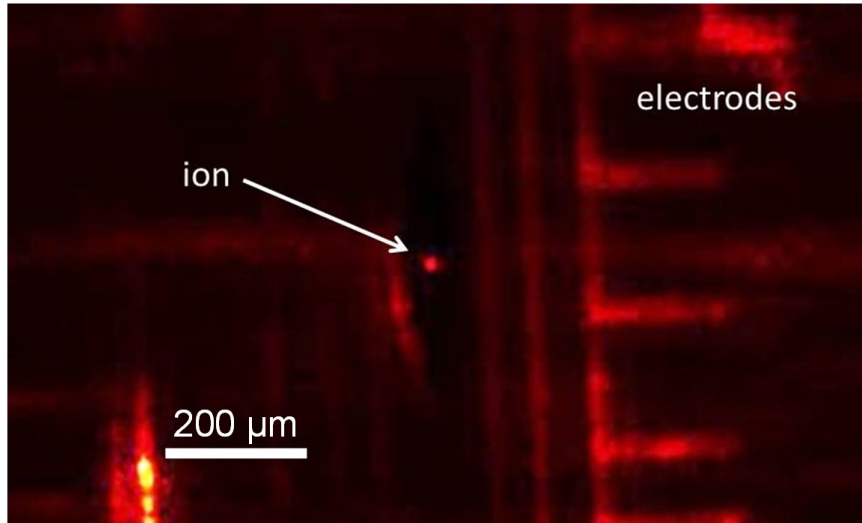


Figure 2.29: A single ion trapped in the IDM trap loading region. Imaging was performed using the bulk-lens objective. The diffractive mirrors were not used to obtain this image.

ion. The first image that we captured (Fig. 2.29) was obtained only using external bulk optics as shown in Fig. 2.28. We use this imaging mode for trapping and shuttling. At this point of time we did not have the capability to shuttle the ion and all the test were made at the loading zone.

By changing the optical setup configuration, we focused the light reflected from the load zone collimator on the camera. The image taken is shown on the right side of Fig. 2.30. In this mode we used an iris on our objective lens to make sure that we are limiting the collection of scatter from the surface of the chip. Due to aberration the image size is several times larger than diffraction limit. One of the reasons for this aberration is that the ion is not exactly at the right height for the collimator. Another important reason is that during the ablation of the loading zone the mirror had been deformed. The image in Fig. 2.31 shows that if we move the ion along the trap axis by several μm two images will be formed from one ion. Changing the height of the ion changes the distance between these two images. The same behaviour was observed in the diffractive lens project (previous project in the group) when ion was not at the focus.

The florescence counts that we measured from the collimator was the same as bulk optic imaging within 20%. Numerical aperture of the bulk optics is 0.39 equivalent to collection efficiency of 4%. Therefore, the estimate for collection efficiency of the loading zone mirror is $4 \pm 1\%$. The size of loading zone mirror is about 50% larger than the other collimators but about half the area is ablated to create the loading hole therefore we have higher collection efficiencies for other mirrors (see chapter 6).

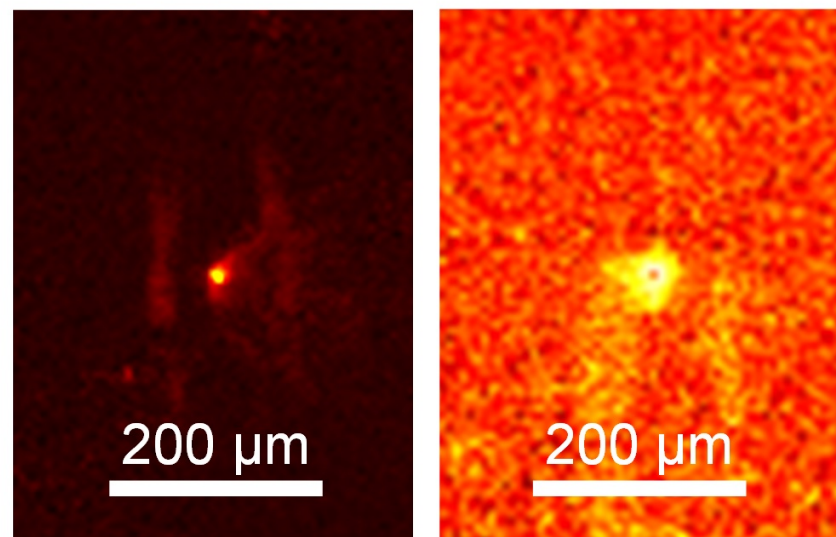


Figure 2.30: Comparison between bulk-lens and diffractive mirror imaging for a single ion in the IDM trap. Both images are taken under identical camera integration conditions and are background-subtracted to remove the scattered light. Left: bulk-lens image. Right: diffractive mirror image obtained with the loading zone collimator. The fluorescence collection efficiency is estimated as 4%. The loading zone collimator is cut in the middle to create the loading hole and this has been deformed the mirror and has increased the aberration.

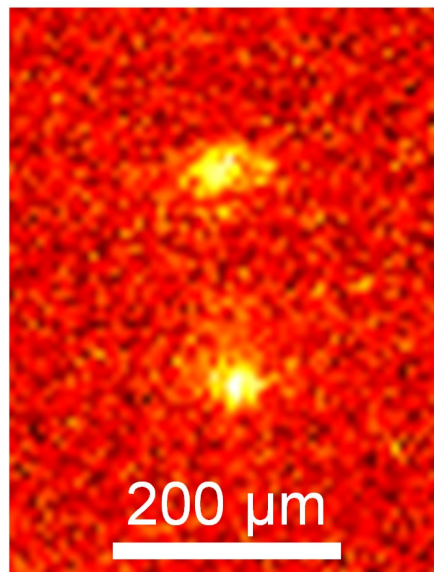


Figure 2.31: Image of a single ion using the loading-zone diffractive mirror. The image was obtained by moving the ion several microns along the trap axis relative to the image in Fig. 2.30. The apparent duplication of the image is consistent with aberrations of the imaging system.

2.4 Atom Source

To create and trap Yb ions, a source of neutral Yb atoms is needed. We generate a beam of these atoms using an atomic oven. The oven consists of a tantalum foil cylinder filled with Yb chips. We apply 1 A of current through the oven and resistive heating evaporates the neutral Yb. A second cylinder is placed between the oven's output and the loading hole in the chip. This second cylinder prevents neutral Yb from coating the chip pins and shorting them. It consists of two disk with a hole at the middle that collimates the neutral Yb beam and directs that towards the trapping node.

Despite having the collimating cylinder, the oven coats some Yb on the back side of the loading hole and over time this layer changes the potential around the loading zone. This can be countered by applying an upward electric field with respect to the chip surface to the ion. Previous experience in our group on the previous needle trap shows that Yb gradually covers the top vacuum window and this may drop the transmission of the window dramatically over time. In this case the trap has to be brought up from vacuum and the window must be cleaned by soaking in a dilute concentration of sulphuric acid.

2.5 Vacuum System

The trap needs to be installed in a vacuum chamber for operation. In ultra-high vacuum regime ($\leq 10^{-11}$ Torr) the ion lifetime is of the order of hours for our system. A schematic of our vacuum system is shown in Fig. 2.32 . A Kimball Physics MCF600-SO200800 spherical octagon chamber is the central part of our vacuum system. This design allows us to have six windows with clear aperture of 1.5", approximately 150 mm from the center of the trap, for horizontal access of the lasers, and two windows with clear aperture of 4.3" for optical access from top and below (with the chip trap only the top window can be used for imaging). It is equipped with a titanium sublimation pump, an ion pump and an ion gauge.

The chip itself is built on a $11 \times 11 \text{ mm}^2$ silicon dioxide substrate which is housed in an interface plate that contains 100 pins connected to trap DC electrodes. The trap socket is made of the vacuum compatible plastic PEEK (polyetheretherketone). Socket pins are connected to four vacuum compatible Accu-Glass 100220 DB25 connectors through Kapton coated solid-core wires. To avoid contamination from entering the vacuum system, at the time of building or opening, a walk-in clean room (specified at class 10,000) is used. Many types of contaminations including plastic and bio-chemicals can prevent the trap from reaching ultra-high vacuum even with long baking times. The new chamber was baked for 20 days without the trap installed. We use heater taps and aluminium foil to heat the trap up and use manual variacs to control the heat. The temperature is monitored at multiple points using a thermocouple thermometer.

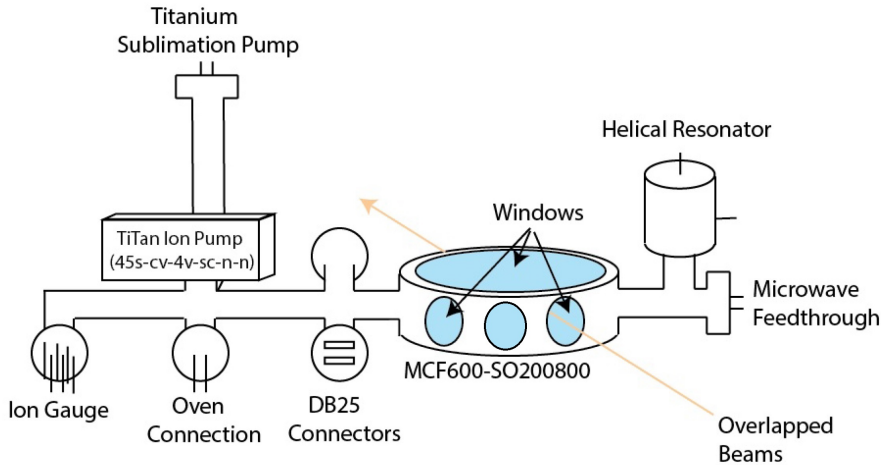


Figure 2.32: A schematic of the vacuum chamber which consists of the main octagonal part and branches for titanium sublimation pump, ion pump, ion gauge, oven connection, Microwave feedthrough, DB25 connections and RF input. (Image taken from [7])

To build the vacuum chamber for the first time we cleaned all the components (except for the chip itself) by sonication in acetone, then methanol, and lastly isopropanol. Then all the metal and ceramic parts were assembled and mechanically pumped to $\sim 10^{-8}$ Torr. This pumping system consists of a turbo pump connected to a roughing pump. At this stage a residual gas analyser (RGA) was used for leak check. Then the chamber was baked (without chip trap) with $350^\circ C$ for 20 days to remove hydrogen and water from the stainless steel. After baking and cooling down, we were able to pump the chamber down to 10^{-11} Torr using the ion pump.

The next part was installing the chip and reaching ultra-high vacuum. This part of the procedure must be repeated each time we open the trap. We need to fill the chamber with nitrogen to bring it to atmospheric pressure and open it in a clean room. After installing the chip we let the turbo and roughing pump to drop the pressure to 10^{-8} Torr. At this stage the chamber(including the chip) is baked at $200^\circ C$ for a week. After finishing the baking and letting the chamber to cool down, ion pump, ion gauge and Titanium sublimation pump are degassed. At this stage the chamber is sealed, with an all metal angle valve, and the ion pump and titanium sublimation pump bring the pressure down to 10^{-11} Torr and keep it there. At the moment we do not use an ion pressure gauge because it tends to increase the pressure while operating. The pressure is monitored using ion pump pressure reading which is derived from the pump current.

In our first attempt after installing the trap the chamber was baked for about 2 weeks at $250^\circ C$. At the end of the procedure, the monitoring of the contaminations with residual gas analyser (RGA) showed PEEK contamination. After cooling down the chamber the

pressure only reached 3×10^{-9} Torr which is not acceptable for the trap operation. The problem was that the temperature was too high for PEEK and it started outgassing. Baking the chamber again without the trap with $350^\circ C$ did not solve the problem therefore ultrasonic cleaning was used. For the next bakeout we tried to keep the temperature between $180 - 200^\circ C$ and successfully reached 10^{-11} Torr. Baking with the temperature of $200^\circ C$ and higher for a long time can also lead to formation of micron sized hummocks and extruded whiskers on trap electrodes (see [4]), therefore it is recommended to keep the temperature below $200^\circ C$ and keep the baking time as short as possible.

CHAPTER 3

Laser Systems, Cooling and Ionisation

Cooling an ion trapped in a Paul trap and manipulating and reading the ion's quantum state involves interaction of the ion with one or more lasers. Driving an optical transition with one laser requires very narrow linewidths on the order of *MHz* and precise control of the laser frequency.

Three external cavity diode lasers (ECDLs) are used in my experiments. Two of them are in UV range and one them is in the IR range. We use atomic spectroscopy to lock the frequency of the UV lasers to the desired transition. These lasers include a 370 nm laser, used for cooling/fluorescence generation and ionisation, a 399 nm Laser for ionisation, and a 935 nm laser used to drive the ion when it falls to the $D_{3/2}$ dark state and can no longer be excited by the 370 nm laser.

3.1 Scattering Rate and Saturation Intensity

The three main atom-photon processes involved in this experiment are absorption, spontaneous emission and stimulated emission. In the process of absorption, a photon that has an energy close to the energy difference between the two atomic levels, is absorbed and excites the atom to the higher level. For an atom in an exited state, there is an exponential decay probability with a time constant called transition lifetime, to decay to a lower state and emit a photon in a random direction governed by a specific emission pattern that depends on the transition. This is called spontaneous emission. Stimulated emission is the interaction of a photon with an atom in exited state that causes the atom to fall into a lower state and emit a photon which is coherent with the incident photon.

The probability of absorption and emission of a photon depends on the intensity of the laser, natural characteristics of the atom and the specific transition properties. The total scattering rate for a 2 level atom, driven by a laser, is [75]:

$$\gamma_p = \frac{s}{1+s} \frac{\gamma/2}{1 + (\frac{2\delta}{\gamma\sqrt{1+s}})^2} \quad (3.1)$$

where s is the saturation parameter, γ is the linewidth of the transition in rad/sec (which is equal to $1/\tau$ where τ is the transition lifetime) and δ is the laser frequency

detuning from the resonance.

The saturation parameter s is defined by the ratio of the laser intensity I and the saturation intensity I_{sat} . Saturation intensity is defined as having one photon per atomic cross section per spontaneous lifetime. The saturation intensity for a 2 level atom, with laser at resonant frequency, is [75]:

$$I_{sat} = \frac{\pi hc}{3\lambda^3\tau} \quad (3.2)$$

where h is the Planck's constant, c is the speed of light, λ is the wavelength of the laser, $\tau = 1/\gamma$ is the excited state lifetime. The resonance saturation parameter is defined by:

$$s_0 = \frac{I}{I_{sat}} \quad (3.3)$$

for the ${}^2S_{1/2}$ - ${}^2P_{1/2}$ transition of ${}^{174}Yb^+$ we have:

$$I_{sat} = 5.05 \times 10^2 W/m^2 \quad (3.4)$$

If the laser is detuned by δ from the resonance, the scattering cross section of illuminated photons decreases therefore we have smaller, effective saturation parameter:

$$s = \frac{s_0}{1 + (2\delta/\gamma)^2} \quad (3.5)$$

Equation 3.1 shows that if the laser frequency is at resonance and the laser intensity is the saturation intensity, the scattering rate is $\gamma/4$. For ${}^{174}Yb^+$, the ${}^2S_{1/2}$ - ${}^2P_{1/2}$ transition linewidth, γ , is 123×10^6 rad/s (19.6 MHz) therefore the scattering rate on resonance at 10^{-8} Torr saturation intensity is 30.8×10^6 photons/s.

3.2 Yb Atomic Transitions

In my project two sets of distinct energy levels of Yb were important; the first one was the transitions for the neutral ${}^{174}Yb$ atom and the second for the ${}^{174}Yb^+$ ion.

At the start of each experiment we generate neutral Yb atoms (see section 2.4) and ionise them in a two level process shown on the left side of Fig. 3.1 (For detailed explanation of ionisation process refer to section 3.3). The first step of the ionisation is to excite the 1S_0 - 1P_1 transition in neutral Yb. The wavelength of this transition is 398.9 nm with the natural linewidth of 28 MHz giving an excited state lifetime of 5.7 ns. The second transition is the excitation from the 1P_1 level to the ionisation continuum. The maximum wavelength to ionise the atom is 394.1 nm and the energy of 370 nm photons is enough for this final step of ionisation.

The right side of Fig. 3.1 shows the relevant transitions for ${}^{174}Yb^+$ ion. The main

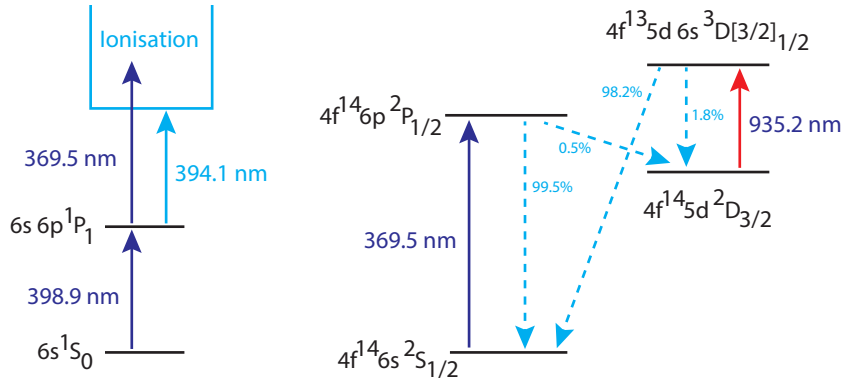


Figure 3.1: Relevant energy levels for neutral and ionised Yb. Left: Neutral Yb energy levels from [5]. Right: Yb^+ energy levels and branching ratios from [6]. Spontaneous decay times from $^2 P_{1/2}$, $^2 D_{3/2}$ and $^3 D_{3/2}$ states are 8.1ns, 53ms and 37.9ns respectively.

transition here is the $^2 S_{1/2} - ^2 P_{1/2}$ transition with wavelength of $369.5\ nm$. Linewidth of this transition is $19.6\ MHz$ which is equivalent to excited state lifetime of $8.1\ ns$. This is the main transition for cooling, fluorescence imaging and single photon generation. When the ion is excited to the $^2 P_{1/2}$ state, it returns back to the $^2 S_{1/2}$ state 99.5% of the time and emits a photon with wavelength of $369.5\ nm$ but there is a 0.5% chance for the ion to fall into the $^2 D_{3/2}$ state. The lifetime of this state is $53\ ms$ and falling into this state slows down the process of cooling and fluorescence generation for this period of time. To prevent this delay, we pump the $^2 D_{3/2} - ^3 D_{3/2}$ transition with a laser at $935.2\ nm$ wavelength. The linewidth of this transition is $4.2\ MHz$. From the exited state of $^3 D_{3/2}$, atom falls to $^2 S_{1/2}$ state with probability of 98.2%. The lifetime of this decay is $37.9\ ns$ which is about six orders of magnitude shorter than the lifetime of the metastable state $^2 D_{3/2}$. There is a 1.8% chance for the ion to return back to $^2 D_{3/2}$ state but $935.2\ nm$ laser excites the ion again and eventually it ends up in the ground state.

3.3 Ionisation

In the process of trapping an ion, our atom source sends neutral Yb atoms into the region of trapping potential. This neutral Yb gas contains seven different stable isotopes. Table 3.1 shows the list and specification of these isotopes.

^{174}Yb and ^{171}Yb are the most widely used isotopes for trapped ion experiments. ^{171}Yb has a nuclear spin of $1/2$ and this creates a hyperfine splitting in its energy levels. ^{171}Yb is used when there is a need for hyperfine levels such as when we want to encode a qubit. To drive these hyperfine levels and have a continuous cooling cycle, a microwave source is needed [78]. Neither of our experiments needed these hyperfine levels, therefore we only

Isotope	168	170	171	172	173	174	176
Natural abundance	0.13%	3.04%	14.28%	21.83%	16.13%	31.83%	12.76%
Isotope shift (MHz)	1887	1192	939 (centroid), 832 ($F=3/2$), 1153 ($F=1/2$)	533	291 (centroid), 587 ($F=7/2$), 515 ($F=3/2$), -253 ($F=5/2$)	0	-509

Table 3.1: Natural abundances [76] and isotope splittings [77] of neutral Yb. Isotopes with an odd number of atomic mass units have multiple peaks due to hyperfine structure.

used ^{174}Yb . This isotope is the most abundant isotope and does not have nuclear spin. Because of the abundance, the choice decreases the time needed to ionize and trap an ion.

To selectively trap the ^{174}Yb isotope, we use a double step ionisation process. First we use a 398.9 nm laser to isotope selectively drive neutral ^{174}Yb from 1S_0 to 1P_1 . Because of the different nuclear masses and nuclear spins, the wavelength of this transition is slightly different for each isotope. The difference in the wavelengths is very small therefore we need to have a laser with a narrow linewidth locked to the frequency of the transition of that isotope, to be able to select it.

Even if our laser linewidth is narrower than a MHz , because of the finite linewidth of the transitions we may excite the neighbouring isotope ^{172}Yb . To calculate the relative chance of exciting ^{172}Yb , we use equation 3.1.

If we suppose that the laser is at resonance for ^{174}Yb ($\delta = 0$), it is detuned by the amount equal to isotope frequency splitting for ^{172}Yb . Dividing the two scattering rates, the relative scattering rate is:

$$R_\gamma = 1 + (\Delta\delta/\gamma_0\sqrt{1+s_0})^2 \quad (3.6)$$

where $\Delta\delta$ is the frequency difference between the transitions for the two isotopes. From table 3.1 $\Delta\delta = 533MHz$. The natural linewidth of 1S_0 to 1P_1 transition for neutral Yb, γ_0 , is 28MHz [77]. With 399 nm laser intensity of $0.5W/cm^2$ and saturation intensity of $6.8 \times 10^{-2}W/cm^2$ [77] we have a saturation parameter s_0 of 7.25. Therefore from equation 3.6 our relative scattering probability is 44.9. Higher natural abundance of ^{174}Yb increases this value by a factor 1.5 and decreases the chance of trapping ^{172}Yb to 1/75. If the transition is Doppler broadened the chance of trapping other isotopes increases. With the collimation procedure described in section 2.4 we minimise the component of atoms' speed along the laser direction and reduce Doppler broadening. A graph of loading ratio versus frequency detuning is shown in figure 3.2. It shows that if the frequency shift is higher, the load ratio of ^{174}Yb increases but higher saturation parameter decreases the load ratio of the ^{174}Yb .

In the second step of the ionisation process we need to drive the atom from 1P_1 to the free continuum state. This transition needs at least 3.1468 eV (394.1 nm) and the

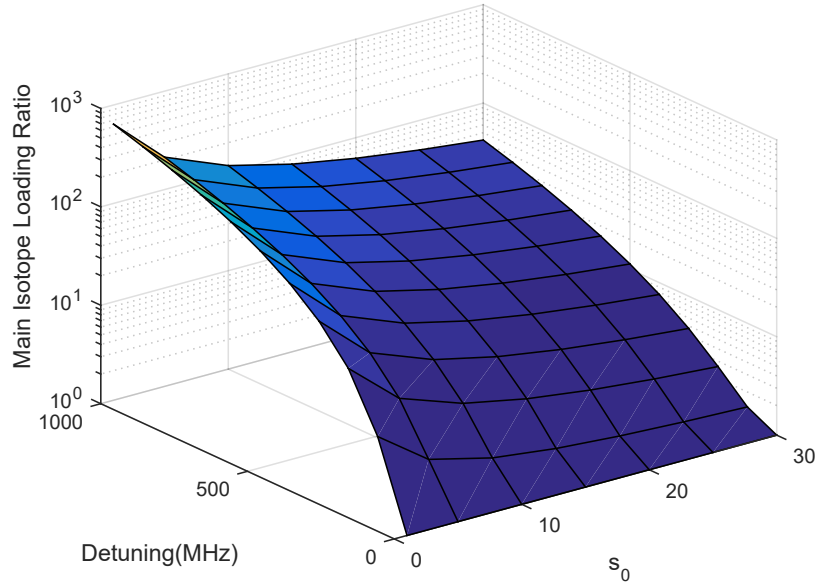


Figure 3.2: Loading ratio of ^{174}Yb for different frequency shifts and saturation parameter. Higher frequency shift increases the load ratio of ^{174}Yb but higher saturation parameter decreases this ratio.

3.3509 eV energy of 370 nm photons is enough to ionise the atom. This ionisation happens near the trapping node and if the ion speed is low enough so that the sum of kinetic and potential energy of the ion is less than the depth of the trapping potential, it confines the ion. The energy of the ion is equal to the thermal energy of the neutral atom and the recoil energy of the electron does not have a large effect on this energy (because electron is about 300000 times lighter than the atom). The depth of our trap is about 100 meV and this is equivalent to temperature of 1160 K. After laser cooling the temperature becomes less than a mK.

3.4 Laser Cooling

To reduce the temperature of the trapped ions we use Doppler laser cooling. Doppler cooling is the process of decreasing the momentum of the ion using recoil photon absorption and emission by the atom. For this type of cooling one needs to use a transition with short lifetime (narrow bandwidth) [12] and laser frequency must be red detuned relative to the resonance. To explain this effect, for simplicity, we only focus on the axis parallel to the laser direction. Because of the Doppler effect, the frequency of the laser in the ion's reference frame changes depending on the direction of the ion's velocity. In the case that ion moves towards the photons the frequency shifts towards blue. The relativistic

frequency shift is:

$$\omega' = \omega \sqrt{\frac{(1 - \frac{v}{c})}{(1 + \frac{v}{c})}} \quad (3.7)$$

Where ω' is the frequency in ion's reference frame, ω is the frequency in lab's frame, v is the ion's speed and c is the speed of light. By neglecting the $(\frac{v}{c})^2$ term for the low velocity limit, the frequency shift is:

$$\omega' = \omega(1 - \frac{v}{c}) \quad (3.8)$$

Ignoring relativistic effects (second-order Doppler shift) leads to error of about 1 kHz . This is three orders of magnitude smaller than 1 MHz accuracy that we need in our experiments. This error becomes important in some applications such as atomic clocks [79]. Rearranging equation 3.8 in terms of frequency detuning gives:

$$\Delta\delta = \omega - \omega' = \frac{\omega v}{c} \quad (3.9)$$

This means that to effectively cool the ion, detuning must be proportional to the speed of the ion. If this frequency shift is equal to the laser detuning, there is a higher chance for the photons to get absorbed by the atom. If the photons are absorbed, this head to head collision reduces the momentum of the atom in this direction. The excited atom spontaneously emits a photon in an approximately random direction (Based on the emission patterns explained in section 5.1). The recoil from the emission adds to the momentum of the ion. In many scattering events the effect of this recoil averages to zero and given that ion speed is larger than recoil velocity, the process reduces the atom's energy.

In the case that the atom moves away from the photons absorption leads to heating. If we suppose that the laser is at ideal frequency detuning of $\omega v/c$ (where v is the thermal speed of the ion), the frequency of the cooling photons will be at resonance and the frequency of the heating photons will be at $-2\omega v/c$ from the resonance. This shows that the higher the temperature the ion has, the higher the difference in scattering rate of the cooling and heating photons and this means that the overall effect is cooling and this cooling is more effective when ion temperature is higher.

If for different trapping axes the trapping frequencies are degenerate, at least 3 lasers are needed to cool the atom; one for each axis. In our case because of the anisotropy for the two RF axes and the DC axis, it is possible to use only one laser. The only requirement is that we need to set the laser direction in a way that it has a component along each of the three axes. In an experiment in our group the effect of cooling only in a specific direction was engineered and the failure of the cooling in the other directions was observed using the thermometry method proposed in the paper [80].

The lower limit for the Doppler cooling is reached when the cooling and heating rates are in equilibrium. From [12] we have two limits for the minimum temperature achieved by Doppler cooling. One is the limit imposed by recoil energy of one photon:

$$T = \frac{\hbar^2 k^2}{2mk_B} \quad (3.10)$$

where k is the wavevector of the photon, k_B is the Boltzmann's constant, m is the mass of the ion and \hbar is the reduced Plank's constant.

Because of the finite natural linewidth of the transition the mean squared velocity does not average to zero and this leads to another limit for the Doppler cooling:

$$T = \frac{\hbar\gamma}{2k_B} \quad (3.11)$$

Where γ is the transition linewidth (in rad/s). In our case the second limit is larger and sets the limit for our cooling. The transition that we use for cooling is the $^2S_{1/2}$ - $^2P_{1/2}$ transition with wavelength of 370 nm and transition linewidth of $123 \times 10^6\text{ rad/s}$. For this transition the minimum temperature is 0.47 mK .

3.5 External Cavity Diode Laser

The lasers used in my experiments need to be tunable at least over a few tens of GHz in frequency, have linewidths smaller than 1 MHz and hit the wavelength needed for the specific atom we are using. External cavity diode lasers are cost effective and efficient options for this purpose. A bare diode has a very wide bandwidth (a few tens of nm in wavelength) and is very sensitive to optical feedback. Random feedbacks can change the gain for the modes near the main mode and push laser to operate in multimode or hop to another mode. Sending a controlled amount of light to the diode keeps the gain of main mode higher than other modes and stabilises the mode. This fractional feedback is generated by a diffraction grating. The -1 order of the grating is used to reflect back approximately 12% of the light into the diode. The rest of the light is reflected normally and used as output. This grating forms a long external cavity that narrows the bandwidth and stabilises laser against stray light. A lens is needed to collimate diode light before it is sent to the grating (Fig. 3.3).

The laser usually oscillates in the highest gain mode because this mode limits the number of electron-holes for the other modes and as a result extinguishes the others. In ECDL this gain is a function of four factors (Fig. 3.4):

1. The medium gain: this gain is determined by the properties of the diode and is very wide in wavelength. For example this is about few tens of nm for the 935 nm laser. The peak of this wide gain can be changed using diode temperature.

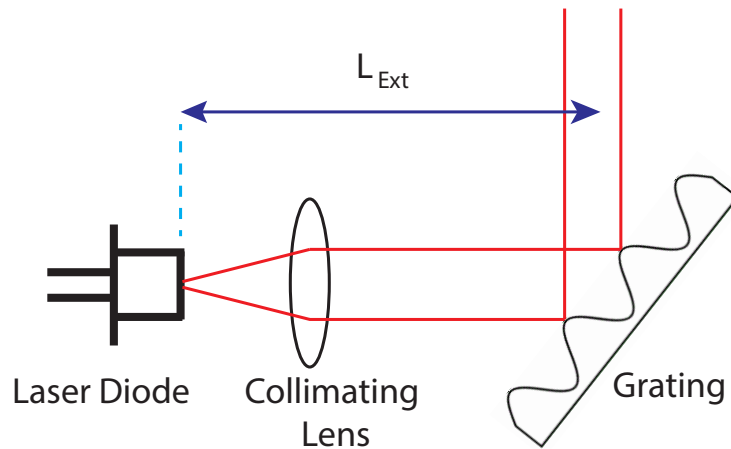


Figure 3.3: A schematic of external cavity diode laser components

2. Internal Cavity: facets of the diode forms an optical cavity that makes the gain periodic. This period is called free spectral range. The internal cavity of 935 nm laser is about 1 mm long. Free spectral range for this cavity is about 10 pm . Changing temperature shifts the peak of this gain in the same direction of the medium gain but with a different rate. Because the former changes by variation in diode length due to thermal expansion but the latter changes by the variation in the bandgap energy of the semiconductor due to the change in the lattice spacing.
3. The grating feedback: For each angle of grating only a certain frequency is reflected back to the diode. The linewidth of this feedback decreases with the increase of the line density of the grating. The linewidth also depends on the beam spot size on the grating. For our 935 nm laser the spot size is about $1\text{ mm } 1/e^2$ diameter and the grating density is 18000 lines/mm . This gives us linewidth of about 5 pm .
4. The external cavity: Grating creates an extra cavity for the diode but with longer length. This leads to a much shorter free spectral range and narrower linewidth. The cavity length of the 935 nm ECDL is about 10 mm and this gives us free spectral range of about 1 pm .

All the lasers that we use are ECDLs. All of them were originally homebuilt ECDLs but currently we use MOGLabs commercial laser for 370 nm laser. During my doctoral studies I had to realign and optimise ECDLs. The first step in this process was to make sure that diode light is collimated after the lens. The next step was to change the tip/tilt

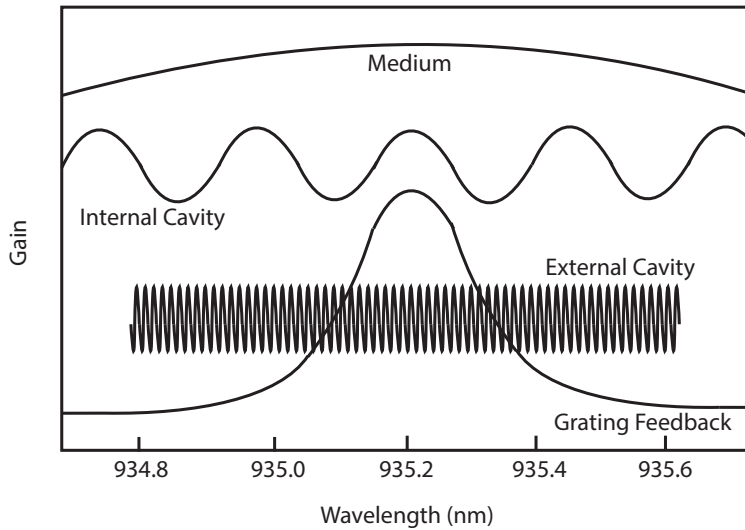


Figure 3.4: Schematic representation of 935 nm laser ECDL gains vs. wavelength.

of the grating and the focus of the lens iteratively to minimise the lasing threshold current. To measure the threshold current, I set the current just below lasing threshold and swept the current and monitored laser power on a photo-diode. The next step was to increase the current to reach the desired power. At this power, frequency was set by changing the length of the external cavity. A discrepancy of few picometers in wavelength was fixed by changing the diode temperature.

The laser frequency is normally changed through changing the control voltage of the the grating piezo. This gives us about 2 pm mode-hop free tuning range on the 370 nm laser. To increase this range to about 4 pm , we use a variable gain amplifier that amplifies the monitor output of piezo driver and feed that to the modulation input of the laser current controller. By adjusting the gain to the right ratio, 4 pm mode-hop free tuning range is achieved.

3.6 Optical Isolator

To protect our diodes from back reflection and prevent unwanted laser light feedback to the diode, we use an optical isolator consisting of two polarisers and a Faraday rotator (Fig 3.5). Faraday rotation is a magneto-optic phenomenon that rotates the polarisation of the light depending on the propagating direction, along or against the magnetic field. The isolator uses an input polariser that makes the polarisation of the light linear. The Faraday medium rotates the polarisation by 45° . The exit polariser is set to the same

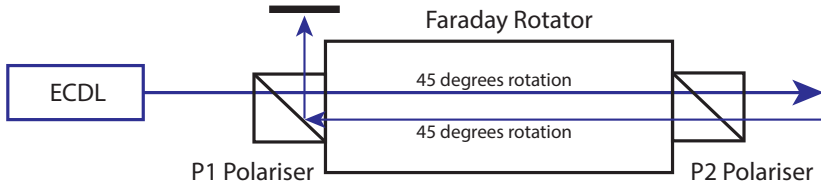


Figure 3.5: A Faraday optical isolator. The input polariser, P1, is set to maximum transmission. The Faraday medium rotates the polarisation by 45° and the output polariser, P2, set to the same angle, transmits the light. For a back-reflection the same process rotates the polarisation in the same direction and this makes the direction of the polarisation perpendicular to the axis of the input polariser, P1. Therefore the polariser rejects the light.

angle to let all the light through. If there is any back-reflection into the isolator the output polariser makes the polarisation linear and the Faraday medium rotates that in the same direction by 45° . This makes the polarisation of the light perpendicular to the direction of the input polariser and this polariser does not let the light to go back to the laser diode.

The angle of rotation depends on the medium properties and strength of the magnetic field. In these isolators, the magnetic field and the polarisers' directions can be manually adjusted. An iterative process is used to find the optimum orientations of the polarisers and the strength of the magnetic field for the 45° rotation. The first step is to take the output polariser, P2, out and set the input polariser, P1, to maximum transmission. The P1 orientation is kept fixed after this step. The second step is to return P2 to its position and rotate the isolator to isolation direction. With this direction P2 is changed for maximum isolation. The third step is to return isolator to transmission direction and maximise transmission by changing the magnetic field. Steps two and three must be repeated until they converge.

3.7 370 nm Diode Laser

We use a commercial MOGLabs Littrow extended cavity diode laser ECD003 as our 370 nm laser source [81]. This system uses the ECDL configuration described in section 3.5 and the control box for this laser provides current controller, piezo voltage controller and one proportional integral derivative (PID) controller. It is also possible to sweep piezo voltage and monitor different laser properties with this box. This box stabilises diode temperature using negative temperature coefficient thermistor for sensing and Peltier thermoelectric

cooler for changing the temperature. At the start of my candidature we used a homebuilt ECDL with Nichia diodes. We experienced sharply reduced lifetime of the diode to one month comparing to one year in the previous diodes. Nichia discontinued manufacturing 20 mW , 375 nm laser diodes and replaced them with 70 mW , 375 nm laser diodes. The new model showed less stability and needed near-perfect feedback setting. We switched to the MOGLabs laser that shows better opto-mechanical stability and flexibility. After optimising ECDL configuration in MOGLabs laser we achieved 4 pm tuning range near 369.525 nm which matches the specification of this MOGLabs model. Our maximum operating power after the grating is 7 mW but the device itself can supply up to 10 mW .

A schematic of our 370 nm laser system is depicted in figure 3.6. This system consists of following components:

1. Optical Isolator: This Faraday optical isolator prevents the back reflection, from the optics in the system, from reaching laser diode. Random back-reflections may push the diode to lase in a power higher than specification and may damage the diode. This component protects the diode against these unwanted feedbacks.
2. Wavemeter: This is used for coarse measurement of laser wavelength with accuracy of 1 pm .
3. Polarisation Spectroscopy: This component works as an atomic reference to lock the laser frequency to the desired transition frequency for a specific isotope. This part is discussed in section 3.7.2.
4. Fabry-Perot Etalon: This component is used to make sure that the laser is lasing in one mode and it is also used for fast locking discussed in 3.7.2.
5. Off Resonant Output: This output goes through an Acousto-optic modulator (AOM) and this AOM changes the frequency to 70 MHz red-detuned from the resonance. We also use this AOM as a switch when needed.
6. On Resonant Output: Using an AOM we can continuously tune the frequency of this output from resonant frequency to about 30 MHz red-detuned. This laser normally operates at -10 MHz from the resonance. This AOM makes a switch to turn the laser on and off for some applications.

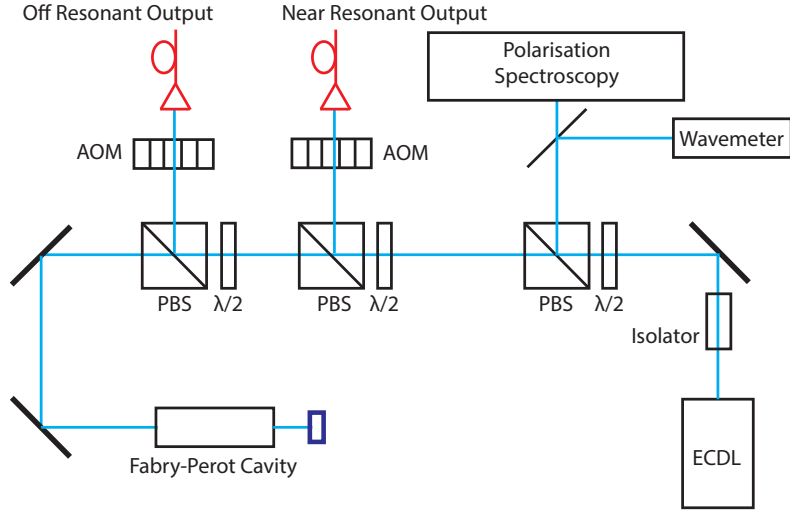


Figure 3.6: A schematic of 370 nm laser system. An external cavity diode laser generates a narrow linewidth laser near wavelength of 370 nm. Half-waveplates and polarising beam splitters are used to split the power for different components. These components include a wavemeter, polarisation spectroscopy system, Fabry-Perot cavity and two outputs with different frequencies for the ion trap.

3.7.1 Lock-in Amplifier

A lock-in amplifier is an electronic component that is used in our atomic spectroscopy systems. This device accepts a periodic reference input and only amplifies the part of the signal that has the same frequency. The signal to noise ratio, that we normally achieve in our spectroscopic systems, is 10 to 1. This is not enough for having a stable reference to lock the frequency. Noise components in the signal are spread on random frequencies. If we modulate the signal with a reference frequency, we can amplify the signal while keeping the noise at the same level.

The first step in using a lock-in amplifier is to generate a reference signal and use it to modulate the signal and feed it to reference input on the lock-in amplifier. The reference signal can be written as:

$$V = V_{ref} \sin(\omega_{ref} t + \theta_{ref}) \quad (3.12)$$

The modulated signal can be written as:

$$V = V_{sig} \sin(\omega_{sig} t + \theta_{sig}) \quad (3.13)$$

where V is the amplitude, ω is the angular frequency and θ is the phase. Lock-in amplifiers multiply the reference signal and the modulated signal and generate the mixed

signal below:

$$V_{mix} = \frac{V_{sig}V_{ref}}{2} \cos([\omega_{sig} - \omega_{ref}]t + \theta_{sig} - \theta_{ref}) - \frac{V_{sig}V_{ref}}{2} \cos([\omega_{sig} + \omega_{ref}]t + \theta_{sig} + \theta_{ref}) \quad (3.14)$$

In the next step, the lock-in amplifier uses a low-pass filter and suppresses all the high frequency components. After this stage ideally only the first term in equation 3.14 remains and if the modulation frequency, ω_{sig} , and reference frequency, ω_{ref} , are the same the output is a DC signal:

$$V_{mix} = \frac{V_{sig}V_{ref}}{2} \cos(\theta_{sig} - \theta_{ref}) \quad (3.15)$$

The equation above shows that the amplitude of the signal is dependent on the phase difference; For no phase difference, the signal is maximum and for phase difference of $\pi/2$ it is zero. Even though we use the same generator for modulation and reference signal, the signal and the reference usually have different phases because they go through different electronics and different lengths of cables that changes the relative phase between them. To get the highest signal, using the phase control knob, we apply a phase shift to the input signal to make it in phase with the reference and maximise the signal. Doing this we reach the maximum signal level of $\frac{V_{sig}V_{ref}}{2}$.

There are two other important settings in every lock-in amplifier: sensitivity and time constant. Sensitivity is inversely proportional to the amplification gain. It determines the voltage level that is equal to 1V/gain. The time constant is the inverse of the bandwidth of the low pass filter. By increasing the time constant, the output becomes more steady and easier to measure reliably. The trade off comes when real changes in the input signal take many time constants to be reflected at the output.

3.7.2 370 nm Laser Frequency Stabilisation

For laser-cooling, we use 370 nm laser which is resonant to the $^2S_{1/2}$ - $^2P_{1/2}$ transition. The linewidth of this transition is 20 MHz and to be able to efficiently cool the ion we need to stabilise the laser frequency within a MHz.

To achieve under a MHz frequency stabilisation, we use saturation polarisation spectroscopy. Our frequency locking system consists of a fast lock using a Fabry-Perot cavity and a slow lock using an atomic reference (See Fig. 3.7). This two-level system is necessary for fast and reliable laser frequency stabilisation for laser-cooling.

The first step of locking is to detect changes in frequency by monitoring changes in Fabry-Perot signal and use a PID controller to compensate for it by changing the external cavity length of the ECDL. A PID controller needs a signal that crosses zero at the desired state of the system. To create this signal we use a dual photodiode. Using a beam splitter

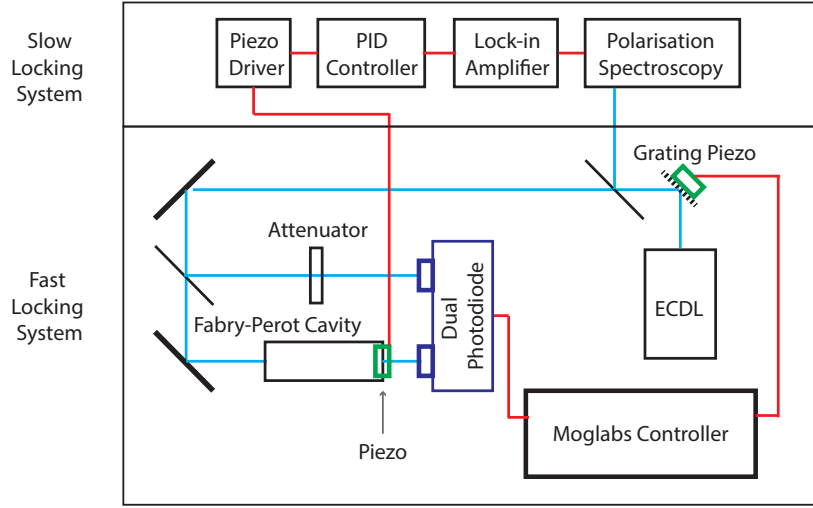


Figure 3.7: A schematic of the 370nm laser locking system. The fast lock section uses a signal from a Fabry-Perot cavity to stabilise the frequency. The slower signal that comes from an atomic reference is used to stabilise the Fabry-Perot cavity length.

we send part of the light through the Fabry-Perot cavity and into one of the detectors. The second part goes through a variable optical attenuator and then goes to the second detector. By adjusting attenuator and subtracting signals we set the middle of the Fabry-Perot peaks to zero volt. The middle of the peak is the steepest part of the signal and the best for fast response to frequency changes.

The locking system above works fine as long as the Fabry-Perot cavity length stays constant but temperature fluctuation alters the cavity length and shifts the frequency away from the set value. We use an atomic reference to stabilise the Fabry-Perot cavity length. This system is a sub-Doppler spectroscopy system.

We use a 3QQNY/YB Heraeus discharge lamp as an atomic reference [82]. This lamp, which has an Yb cathode, is filled with neon with the pressure of 6 Torr. The lamp works at 15 mA of current. The voltage difference between the electrodes accelerates stray electrons in the gas and they ionise Ne . The new electrons from ionisation also ionise other neon atoms and this creates an avalanche. After ionisation, Ne^+ ions start moving towards Yb cathode and sputter Yb throughout the lamp. Neutral Yb atoms are then ionised through the Penning interaction with neon ions.

The simplest way of extracting a signal from this lamp is using the linear absorption of the laser near resonance but the problem is that because of the Doppler effect this signal is tens of GHz wide in frequency and it does not resolve the peaks for different Yb isotopes that have about 1 GHz splitting. To eliminate the Doppler effect we use a saturation absorption spectroscopy technique (Fig. 3.8). In this technique we add a

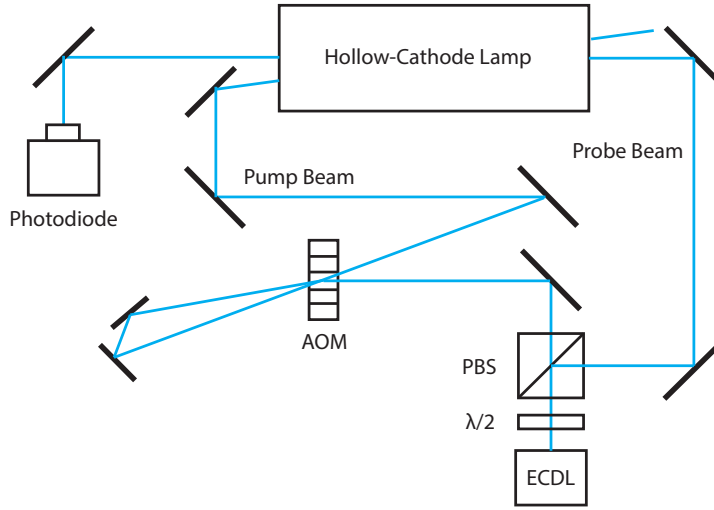


Figure 3.8: Saturation spectroscopy system that uses a high intensity counter-propagating beam to eliminate the Doppler broadening of the spectroscopy signal.

counter-propagating beam to the previous setup that has a high intensity that saturates the absorption by the Yb ions. If we scan the frequency over the resonance and monitor the probe beam, the exact same absorption happens except for the resonant frequency for which we observe small or no absorption. The reason is that because of the Doppler effect the two beams excite different speed classes of the ions. Only at resonance both beams excite stationary ions. In this situation because most stationary ions are already in the excited state, due to presence of the high intensity pump beam, we see much less absorption in the probe beam.

The signal to noise ratio of this signal is not high and to improve it we modulate the pump beam with an AOM and use a lock-in-amplifier to amplify the signal (see section 3.7.1). The signal now has resolution of a few 100 *Mhz* and can resolve different isotopes but it is not suitable for PID controllers that need a zero crossing signal.

To create a zero crossing signal we use the birefringence of Yb ions. From [83] we know that the imaginary part of the complex absorption coefficient is:

$$Im(\alpha) = -\alpha_0 \frac{\gamma(\omega_0 - \omega)}{\gamma^2(1 + I) + (\omega_0 - \omega)^2}, \quad (3.16)$$

Where α_0 is resonant absorption coefficient, γ is the transition linewidth, ω_0 is the resonant frequency and ω is the frequency of the light. This equation shows that a beam experiences a negative phase shift when it is red detuned from the resonance and positive phase shift when it is blue detuned. To use this effect we change our configuration to what is shown in Fig. 3.9. One of the new components is a $\lambda/2$ waveplate in the probe

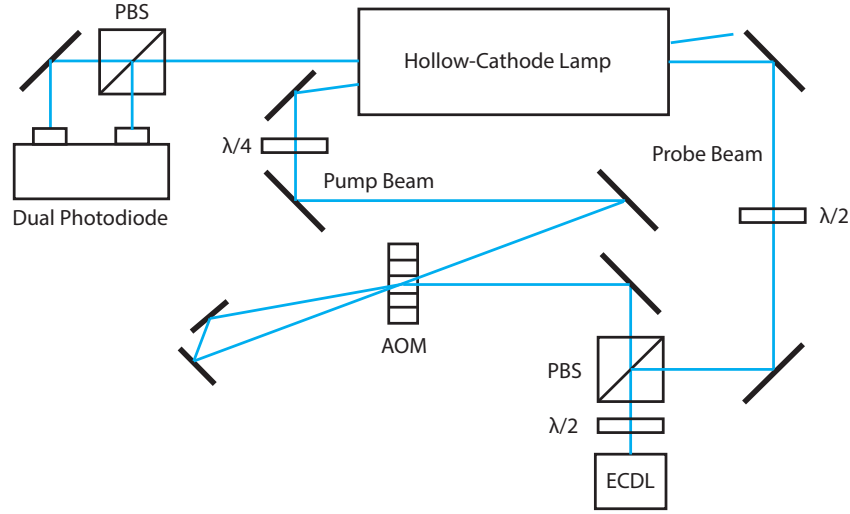


Figure 3.9: A schematic of polarisation spectroscopy for 370nm laser. By using a pump beam with circular polarisation and a probe beam with linear polarisation that goes to a dual photodiode. A narrow zero crossing signal is generated.

beam path to be able to rotate the linear polarisation of this beam. We also change the polarisation of pump beam to σ^+ by adding a $\lambda/4$ waveplate. The probe beam in the new setup, after passing through the lamp, goes through a polarising beam splitter and goes to a dual photodiode.

To realise what happens to the probe beam in the lamp, we need to write it as an equal superposition of σ^+ and σ^- light.

$$E_{\sigma^+} = E_0(\hat{x} + i\hat{y})\cos(kz - \omega t) \quad (3.17)$$

$$E_{\sigma^-} = E_0(\hat{x} - i\hat{y})\cos(kz - \omega t) \quad (3.18)$$

Where E_0 is the amplitude of the electric field, \hat{x} and \hat{y} are unit vectors along x and y axes, i is the imaginary unit, k is the wavenumber and ω is the angular frequency of the electromagnetic wave. If we add these two beams together, they form a linear polarisation. The orientation of this linear polarisation depends on the phase difference between the two beams. If we apply a $+\theta$ phase shift to the σ^+ beam and a $-\theta$ phase shift to the σ^- beam, the sum will be a linear polarisation that creates an angle θ with respect to the x axis.

$$E_{\sigma^+} = e^{+i\theta} E_0(\hat{x} + i\hat{y})\cos(kz - \omega t) \quad (3.19)$$

$$E_{\sigma^-} = e^{-i\theta} E_0 (\hat{x} + i\hat{y}) \cos(kz - \omega t) \quad (3.20)$$

$$E_{\sigma^+} + E_{\sigma^-} = E_0 (\cos(\theta)\hat{x} + \sin(\theta)\hat{y}) \cos(kz - \omega t) \quad (3.21)$$

To setup the system, initially we turn the lamp and pump beam off and set the angle of the polarisation of the probe beam to $\pi/4$, so that equal amount of light goes to the different inputs of the dual photodiodes. In this situation the balanced photodiode shows signal of zero.

The discharge lamp has a magnet that defines the quantization axis, and therefore half of the ions absorb σ^+ polarised light and the other half absorb σ^- polarised light. If we turn the lamp on but keep the pump beam off, both beams experience the same phase shift and the signal remains zero, regardless of the light frequency. But if we turn the σ^+ pump beam on, it saturates the atoms in resonance with σ^- portion of probe beam (because they are counter-propagating). This means that the plasma cloud becomes transparent for σ^- light and it experiences no phase shift. For the σ^+ portion of the probe beam, phase shift depends on frequency. Based on equation 3.16, this phase shift is zero at resonance, positive on the red side of the resonance and negative on the blue side of the resonance. Equation 3.21 shows that this phase shift induces a change in the angle of linear polarisation of the probe beam. On the red side of the resonance this angle increases to values greater than $\pi/4$ and changes the balance between horizontal and vertical ratio of linear polarisation and creates a positive signal. On the blue side the exact opposite happens and we see a negative signal. Based on 3.16 far from the resonance the phase shift becomes zero again and signal retunes to zero.

In reality it is not only the phase-shift that is different between saturated and unsaturated components of the probe beam, linear absorption is also slightly different and this leads to slight amplitude imbalance for the two components of the probe beam after the lamp. This means that the polarisation will not be perfectly linear but rather slightly elliptical. The effect of this ellipticity on the ratio between horizontal and vertical polarisation is much smaller than the phase-shift and it has a small effect on the signal. A graph of the acquired signal is shown in Fig. 3.10.

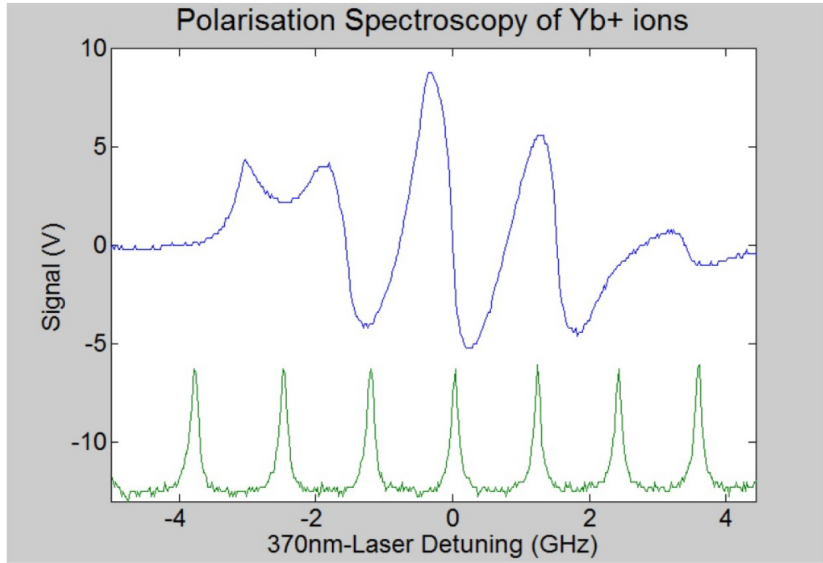


Figure 3.10: Plot of polarisation spectroscopy and Fabry-Perot trace. The blue signal is the polarisation spectroscopy and the green signal is a Fabry-Perot trace. The free spectral range of the Fabry-Perot peaks is 1.25GHz. (graph courtesy of Valdis Blumes [7])

3.8 399 nm Diode Laser

The 399 nm laser system consists of an external cavity diode laser, an isolator, and a spectroscopy set-up. It is used to excite only ^{174}Yb isotope which is then ionised by the 370 nm laser (see section 3.3).

3.8.1 399 nm Diode Laser Frequency Stabilisation

To lock the 399 nm laser to the desired frequency we use a sub-Doppler spectroscopy system shown in Fig. 3.11. This system is similar to the 370 nm spectroscopy set-up (see section 3.7.2) with two main differences. It probes the change in the absorption instead of the phase shift and it uses frequency modulation instead of amplitude modulation.

In this set-up, the portion of the light that is branched for spectroscopy system goes through a $\lambda/4$ wave-plate. This changes the polarisation of the light to σ^+ . This beam acts as a pump beam. After the lamp, beam goes through a polarising beam-splitter and a mirror reflects the vertically polarised part of the light back into the lamp. This beam is an equal superposition of σ^+ and σ^- light (see section 3.7.2 and equations 3.21).

Atoms in resonance with σ^- part of the probe beam are already saturated with the σ^+ pump beam so this part does not experience a frequency dependent absorption explained by equation 3.22.

After the lamp this part again goes through a $\lambda/4$ wave-plate and its polarisation

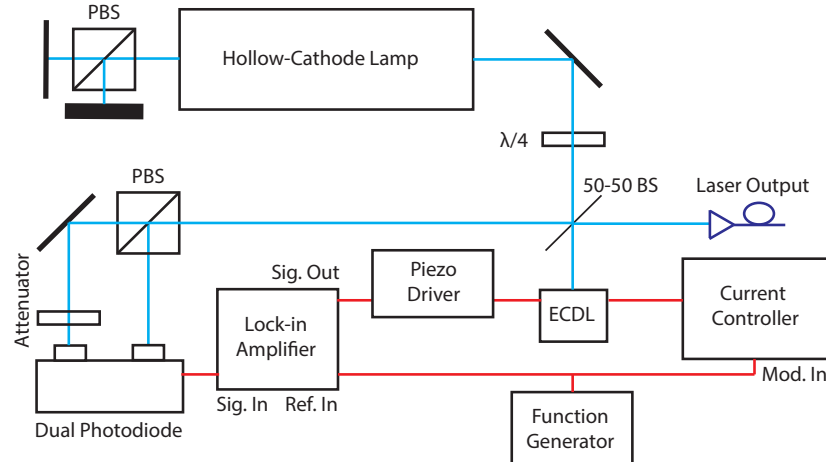


Figure 3.11: Schematic for 399nm-laser polarisation spectroscopy. The first beam through the hollow cathode discharge lamp is a circularly polarised pump beam. After the discharge lamp the beam is split into two and a weaker linearly polarised probe beam is sent back through the hollow cathode discharge lamp. The probe beam is then sent to the dual photodiode. The laser frequency is modulated at 20kHz and a lock-in amplifier is used to amplify the signal.

becomes vertical and after going through a polarising beam splitter, goes to the reference detector in the dual photodiode.

Atoms in resonance with the σ^+ part of the beam are not saturated therefore this part of the beam experiences absorption as explained by equation[83]:

$$Re(\alpha) = \alpha_0 \frac{\gamma^2}{\gamma^2(1+I) + (\omega_0 - \omega)^2}, \quad (3.22)$$

where α_0 is absorption at resonance, γ is the transition linewidth, I is a dimensionless intensity, ω_0 is the resonant frequency and ω is the laser frequency.

This part of the beam also goes through the $\lambda/4$ and becomes horizontally polarised and the polarising beam-splitter sends it to the signal detector of the dual photodiode. This means that the signal is zero away from resonance and it becomes negative near the resonance. This is a narrow signal in terms of frequency but still not a zero crossing signal. To lock the frequency using a PID controller the signal must change sign when crossing the resonant frequency.

We use frequency modulation together with a lock-in amplifier to both amplify the signal and convert it to a zero crossing signal. Suppose that our signal strength is S and we are modulating the laser frequency:

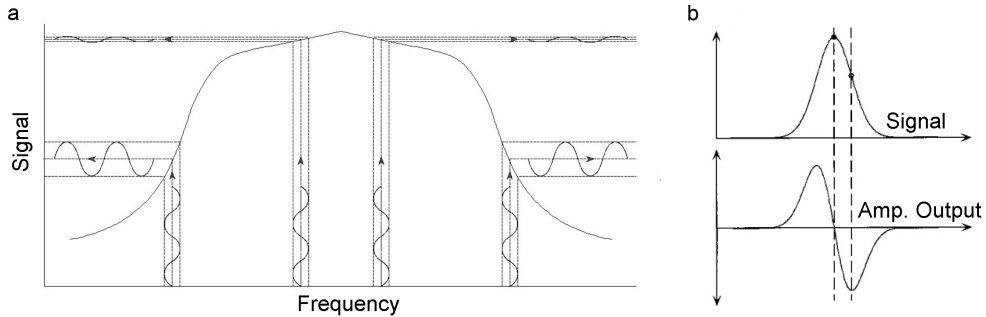


Figure 3.12: a. In a frequency dependent signal, change in signal is proportional to change in frequency times the derivative of the signal with respect to the frequency. b. The lock-in amplifier only amplifies the modulated signal which is proportional to derivative of the signal, therefore its output is positive where derivative is positive and vice versa.

$$f(t) = f_0 + A \sin(\omega t) \quad (3.23)$$

For the limit of small amplitude change we have:

$$S(t) = S_0 + \frac{dS}{df} \times A \sin(\omega t) + O(A^2) \quad (3.24)$$

Because the lock-in amplifier only picks up the modulated part of the signal (see section 3.7.1), its output is proportional to the derivative of the signal with respect to frequency (See Fig. 3.12). This shows that not only the strength of the output but also its sign is dependent on this derivative. Therefore the output is positive on one side of the resonance and negative on the other side.

A graph of obtained signal is shown in figure 3.13. We verified this signal by checking the neutral Yb fluorescence on different isotope peaks.

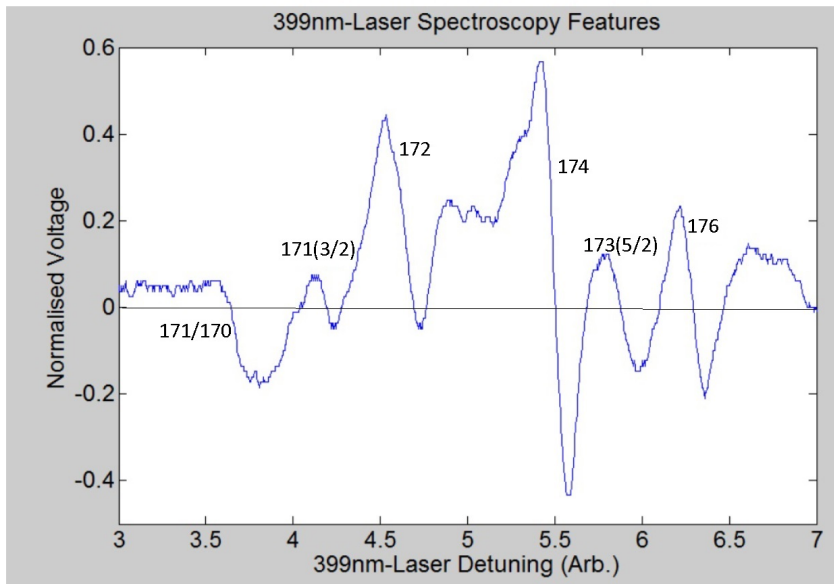


Figure 3.13: 399nm laser spectroscopy trace for neutral Yb. (graph courtesy of Valdis Blums)

3.9 935 nm Diode Laser

As it is shown in Fig. 3.1, during the cooling process, an ion may decay into the $^2D_{3/2}$ state with probability of 0.5%. This is a metastable state with lifetime of 53 ms. This can decrease the cooling rate significantly. To pump the ion out of this state we pump it to $^3D[3/2]_{1/2}$ using a 935.2 nm laser. From this state, the ion decays back into the ground state in 42 ns and emits a 297 nm photon. The 935 nm laser system consists of a home-built external cavity diode laser, an isolator and a Fabry-Perot cavity. This laser does not have any frequency stabilisation system. To make sure that we are efficiently driving the transition, we operate laser at 650 μW , which with spot size of 240 μm $1/e^2$ diameter gives maximum intensity of $2.8 \times 10^4 W/m^2$. This is well above the saturation intensity of $25 W/m^2$. At the same time we sweep the frequency of the laser. With the sweeping, we make sure that the transition is saturated even if the center of frequency sweep slightly drifts from the resonance. To trap the ion it is enough to set the frequency roughly to the resonance using a wavelength meter with an accuracy of a picometer. After trapping, we maximise the ion fluorescence by manually adjusting the center frequency of the sweep. Because of the thermal drifts, we readjust the center frequency once every half an hour. We sweep the laser frequency by modulating the laser current using a bias-tee. The frequency of modulation is 1 MHz.

3.10 Beam Combiner

All the lasers mentioned above are delivered to the trap using single mode fibres. We use fibres so that we can independently align optics in the ion trap side of the experiment and in the laser set-up. We use a beam-combiner set-up to overlap the beams and send them into the vacuum chamber (Fig. 3.14).

There are four inputs to this system. One of them is a 370 nm laser, whose frequency can be tuned from -30 MHz from the resonance up to the resonant frequency. The other one is again a 370 nm laser which is -70 MHz detuned from the resonance. These are combined using a polarising beam splitter thus have linear polarisations perpendicular to each other. Each of these inputs are equipped with a half waveplate to maximise the power after the polarising beam-splitter. We use two dichroic mirrors to add 399 nm and 935 nm lasers to these beams.

These lasers must be overlapped before going to the vacuum chamber. Each fibre is mounted on an adjustable mount and in front of each of the fibre outputs there is a mirror that together with the adjustable fibre mounts enable us to set the position and angle for each input. We use a beam profiler to iteratively overlap laser positions with and without a focusing lens.

The last two components of the system are an Optics In Motion(TM) OIM5001 fast steering mirror and a Thorlabs(TM) LA4874-UV lens with focal length of 150 mm . The lens is mounted on a translator with accuracy of $1\text{ }\mu\text{m}$ and is used for precise positioning of the beam. The steering mirror is used to move the beams with the ion during the shuttling. The mirror has angular resolution of $2\text{ }\mu\text{rad}$ and its response time is 5 ms .

This setup overlaps the four beams and creates a spot size of $80\text{ }\mu\text{m}$ for UV lasers and $240\text{ }\mu\text{m}$ for the 935 nm laser.

For the single-photon generation, we need circular polarisation for 370 nm lasers. In this experiment we add a quarter waveplate after the fast steering mirror to turn the perpendicular 370 nm lasers' linear polarisations into σ^+ and σ^- polarisations.

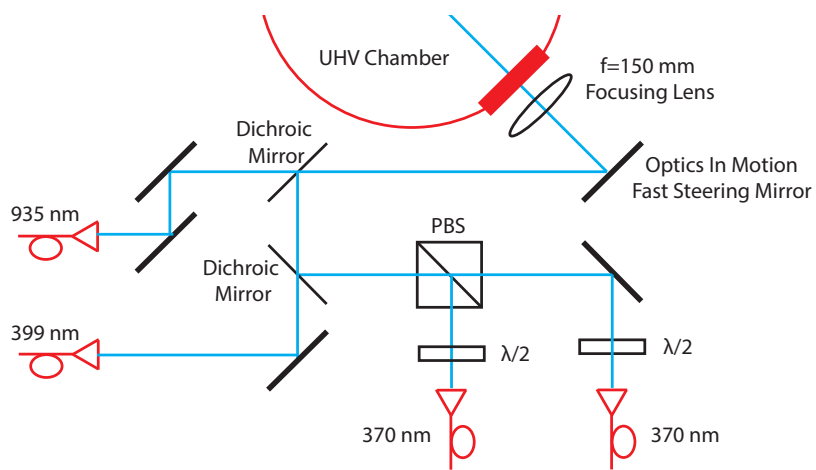


Figure 3.14: Beam combiner setup for lasers in use. The two 370nm laser are combined using a polarising beam splitter and then 399nm and 935nm lasers are added using dichroic mirrors. A fast steering mirror and a lens mounted on a translator is used for adjusting the position and angle of the beam that goes to the vacuum chamber.

CHAPTER 4

Imaging and Optical System

All of my experiments involved fluorescence collection from ions and imaging of ions. For ion imaging and fluorescence collection, we use two modes of imaging: bulk optics imaging and integrated diffractive mirror imaging. The first technique only uses external optics and is used for trapping and shuttling. The second one only works when the ion is near the focus of a diffractive mirror. In this case, we can use diffractive mirrors for high efficiency fluorescence collection and high resolution imaging. The NAs for the two axes of the diffractive mirrors are 0.56 and 0.73. This is equivalent to 13.3% solid angle coverage. The mirror provides total collection efficiency of 5.8(8)%.

4.1 Imaging Using External Bulk Optics

A bulk imaging system enables us to image an ion at every location on the chip (Fig. 4.1). This mode does not use the integrated diffractive mirror therefore has low collection efficiency of approximately 2%. The objective lens has focal length of 60 mm and diameter of 50 mm which is equivalent to NA of 0.38. This mode is a flexible and tolerant mode of imaging for trapping, shuttling and other diagnostic purposes. Imaging in this mode is implemented using a system that consists of two refractive lenses. The first lens is an Asphericon A50-60FPX-U-S with effective focal length (EFL) of 60 mm , working distance of 48.3 mm and diameter of 50 mm . This lens needs to be positioned a focal length away from the ion to collimate the ion fluorescence. The second lens is a Thorlabs LE4560-UV lens with focal length of 200 mm and diameter of 50.8 mm . This second lens focuses the collimated beam, created by the first lens, into a CCD camera and forms an image of the ion. The camera that we use for this mode, is an Andor DV437-BU2 CCD. The detector of the camera is an array of 512×512 pixels and each pixel is $13 \times 13\text{ }\mu\text{m}$. The magnification of the system is the ratio of focal lengths which is $3.33X$.

The distance of the chip from the vacuum chamber window is not exactly known therefore it is impossible to set the position of objective lens first. We know that if the position of this lens is correct, the ion light is collimated after that. Knowing this, we set the distance of the 200 mm lens from the camera to 200 mm and move the position of the objective lens until the chip surface is in focus. To be able to see the chip surface we

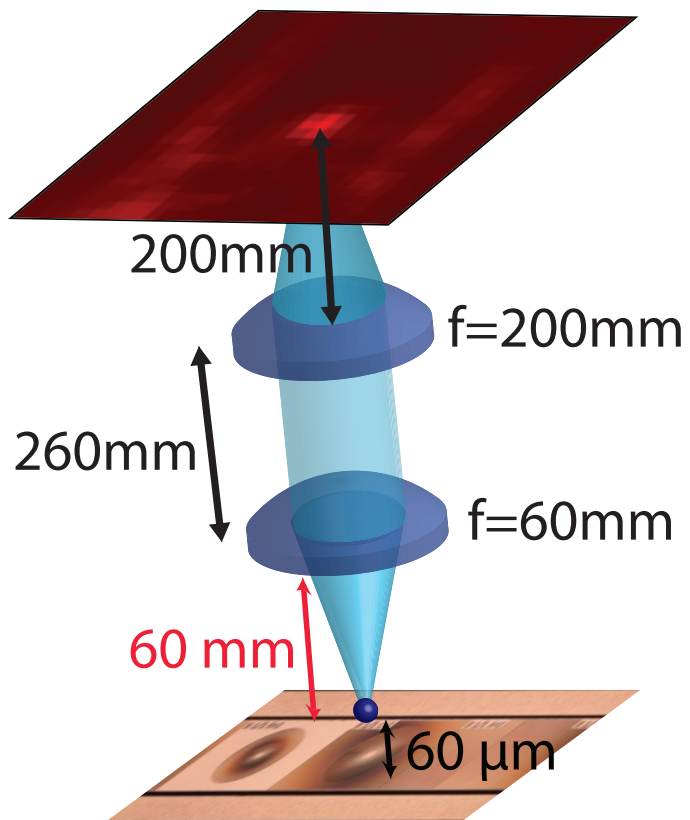


Figure 4.1: A schematic of the lens configuration in the bulk imaging mode (image is not to scale). The ion is located $60 \mu\text{m}$ above the chip. The objective lens with focal length of 60 mm is positioned 60 mm away from the ion. This lens collimates the ion fluorescence. The collimated beam is focused on the camera using a second lens located 260 mm away from the objective lens (vacuum chamber window omitted for clarity).

moved the laser lower to illuminate the chip surface. During this set-up, while the laser is shining on the chip, the RF voltage must be off, otherwise the trap will be charged. As a secondary test to make sure that the objective lens position is correct, we attached the 200 mm lens to the camera and moved both of them together; if the light is collimated after the objective lens the chip image must remain focused regardless of camera position. After this test, the 200 mm lens was detached from the camera and placed 260 mm (sum of the focal lengths) away from the objective lens. Moving the objective lens 60 μm away from the chip puts the ion at the focus. Minor adjustment is needed after trapping to focus the ion image precisely. After optimizing the position of the objective lens we reset the distance of the two lenses to the sum of the focal lengths. Fig. 4.2 shows an image of an ion at the loading zone captured with this optical system. In this image DC electrodes are also visible on both sides of the ion. The oval shaped glow around the ion is the reflection of the laser and the ion light from the edge of the loading zone.

The objective lens is a high NA lens. High NA refractive lenses create an aberrated image if the object is not located on the axis of the lens. To make sure that the imaging axis is aligned with the lenses axes, we used two irises on both sides of each of them and found the tilt angle that enable us to image the ion even with the minimum aperture of the irises. This sets the imaging axis to the center of the lenses and makes it perpendicular to lenses' surface. Using the two irises attached to the camera, we also made sure that the imaging axis is perpendicular to the camera's imaging screen.

After trapping, using the scheme described in section 2.2.1, we shuttled the ion to different regions of the chip. One of the integrated optics that we checked was the self-imager. This optic focuses the ion light back onto the ion itself. Figure 4.3 shows three images of the ion and its secondary image, at three different locations near the center of the self-imager. The image shows that both the direct and indirect images of the ion are in focus. This means that the reflected image from the mirror is at the same distance as the ion from the mirror. Therefore the ion height is the same as the designed focal length of the optic which is equal to the nominal ion height of 58.6 μm . The middle image shows that images are almost overlapped. This means that the ion position has a very small lateral offset comparing to the center of the optic. This shows that the lateral mismatch between the fabrication of diffractive mirrors and the chip electrodes is very small.

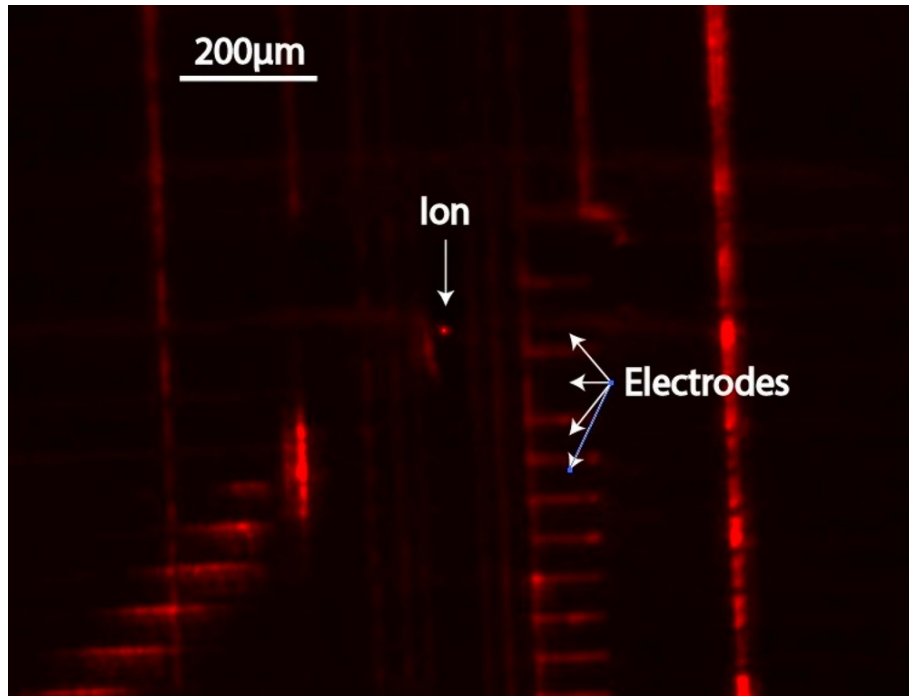


Figure 4.2: An image of the chip and a trapped ion located at the loading zone captured using bulk imaging system. Ion is located at the middle of the loading zone. The oval shaped scatter around the ion is the reflection of laser from the edge of the loading zone. DC electrodes are visible on both sides of the ion.

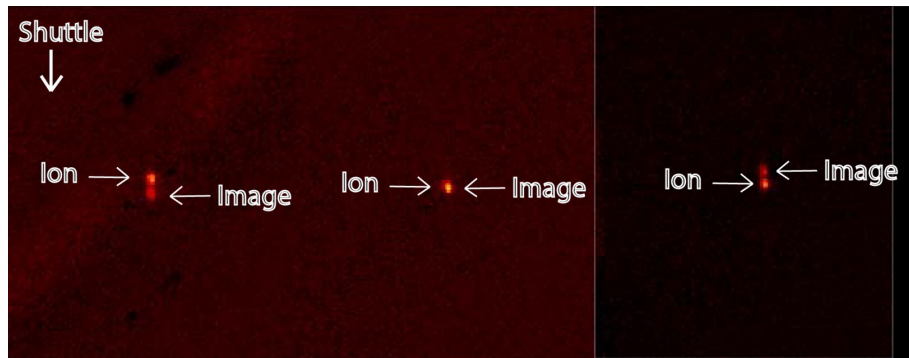


Figure 4.3: Three images from the ion and its image created by the self-imager diffractive optic for different ion positions. This optic forms an image from the ion on itself. Left: the ion is located before the self-imager. Middle: the ion is located on top of the self imager, images are almost overlapped and this shows that we have small lateral mismatch between optics fabrication and electrodes fabrication. Right: the ion located after the self-imager optic

4.2 Diffraction-limited Imaging (Theory)

In the 19th century Lord Rayleigh developed a criterion for the ability to resolve two point sources in an optical system. He showed that because of the wave nature of the light the resolution of an optical system has a limit imposed by diffraction. If one images a point source with an optical system of circular input aperture of radius a , the image looks like the Airy function shown in Fig. 4.4. This means that the image is not confined to a point but it has a central bright peak in the middle and the intensity becomes zero at a ring with $\theta = 1.22\lambda/2a$ (λ is the wavelength of the light) and then again we have series of lower intensity peaks. The exact intensity profile is:

$$I(\theta) = I(0) \left(\frac{2J_1(\rho)}{\rho} \right)^2 \quad (4.1)$$

$$\rho = \frac{2a\pi \sin(\theta)}{\lambda} \quad (4.2)$$

Where $I(0)$ is the maximum intensity, J_1 is the first order Bessel function, a is the radius of the aperture and λ is the wavelength of the light. With this diffractive effect if one tries to image two point sources that are too close to each other their intensity profile overlaps and they become unresolvable. The Rayleigh criterion is that they are resolvable when the peak of one source coincides with the first trough of the other, that is their angular separation is $\theta = 1.22\lambda/2a$.

In the case that the optics add aberrations to the image, the width of the middle peak

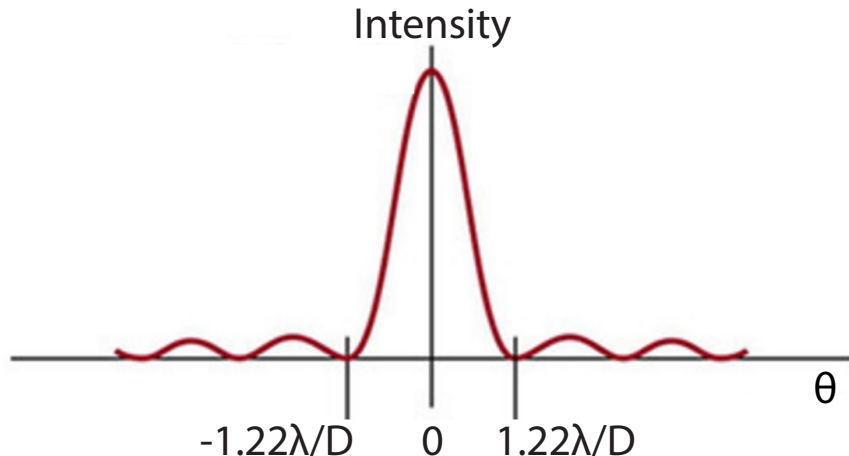


Figure 4.4: Graph of intensity of the diffraction pattern for a circular aperture. First minima happen at $\pm \frac{1.22\lambda}{D}$, where λ is wavelength and D is the diameter of the aperture.

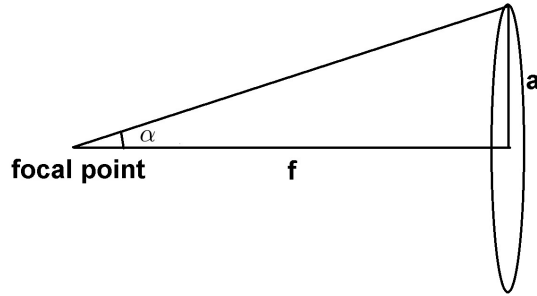


Figure 4.5: Numerical aperture (NA) of an optical system is a dimensionless number that characterizes the range of angles over which the system can accept or emit light. It is equal to $n \sin(\alpha)$, where n is the index of refraction of the medium and α is half of the acceptance angle.

becomes larger; therefore having an image with the same intensity profile as the theoretical profile is an indication of aberration free imaging. If we ignore the surrounding rings, the closest Gaussian profile to the middle peak is a profile with $1/e^2$ radius of [80]:

$$r = 0.43 * \lambda / NA \quad (4.3)$$

In which $NA = \sin(\alpha)$ is the numerical aperture of the optical system (Fig. 4.5). An aberration free imaging system, that creates an image with the $1/e^2$ radius of r from a point source, is called diffraction limited.

Spot size is not the only property of the beam that changes due to aberration; divergence of the beam may also increase if the beam is aberrated. The transverse intensity profile of a Gaussian beam is shown in Fig. 4.6. For a Gaussian TEM_{00} mode, if the $1/e^2$ radius of intensity of the beam at focus is w_0 , The size at a distance y from the focus is [84]:

$$w(y) = w_0 \sqrt{1 + \left(\frac{y}{y_R}\right)^2} \quad (4.4)$$

where $y_R = \frac{\pi w_0^2}{\lambda}$ is Rayleigh range and is the distance from the focus point where the area of the cross section doubles. In the far field, $y \gg y_R$, the angle of divergence approaches:

$$\theta = \frac{\lambda}{\pi w_0} \quad (4.5)$$

For any Gaussian beam, zero order or mixed mode, the product of the radius at the focus, w_{0R} , and the far-field divergence angle, θ_R , is constant. This enables us to define a dimensionless constant for the beam that compares it with lowest divergence case of

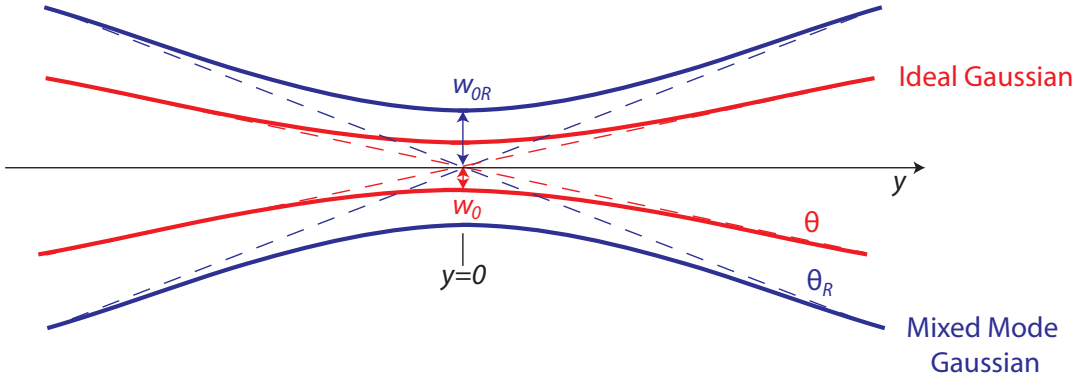


Figure 4.6: $1/e^2$ intensity radius of a Gaussian beam. w_0 and θ are the radius and the angle of the far-field divergence of the ideal zero order Gaussian beam and w_{0R} and θ_R are the radius and the angle of the far-field divergence of the mixed mode beam.

TEM_{00} mode:

$$M^2 = \frac{w_{0R}\theta_R}{w_0\theta} \quad (4.6)$$

This constant is equal to one for Gaussian TEM_{00} mode and it is greater than one for mixed mode beams. This shows that it is possible to match the size or divergence of an imperfect beam to an ideal beam but it is impossible to match both. In applications like fibre coupling both the size and the divergence of the beam must be matched to that of the fibre and this equation shows that it is impossible to do this for a mixed mode beam. Therefore losing part of the power in fibre coupling becomes inevitable.

M^2 cannot be determined with only one size measurement. Based on ISO/DIS 11146 [85], a valid M^2 calculation needs at least 5 profile measurement at the focus and 1 and 2 Rayleigh ranges away from the focus on both sides. It is possible to approximate the divergence angle of the beam with $\theta_R = \arctan(\frac{w(2y_R)}{2y_R})$ and insert it to equation 4.6 and calculate M^2 but the more accurate way to do that is to fit the parametric function below to the data points and calculate the M^2 of the beam:

$$w = w_0 \sqrt{1 + \left(\frac{(y - y_0)\lambda M^2}{\pi w_0^2} \right)^2} \quad (4.7)$$

To use this formula to measure M^2 , we take at least five images around a focus point of the beam and use two Matlab(TM) routines that I developed: *Ion_size* (appendix B) and *M2_Calc* (appendix C).

Ion_size receives a saved background corrected image from the camera in the ASC

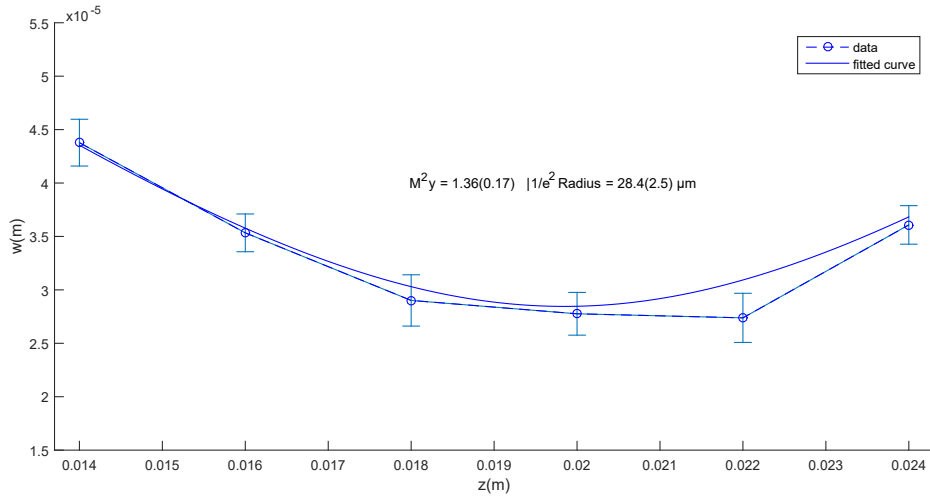


Figure 4.7: An example of measuring M^2 by fitting equation 4.7 to the spot sizes around the focus point for the optical configuration shown in Fig. 4.10. The blue circles are the measured radii and the solid line is the fitted function. In this case M^2 is 1.36 which suggests that our beam is slightly aberrated.

format and returns the size of the ion in two dimensions. In the first step, it identifies the ion position and cuts the image around the ion and then fits the two dimensional Gaussian profile below to the image:

$$f(x, z) = A \exp \left(- \left(\frac{(x - x_o)^2}{\sigma_x^2} + \frac{(z - z_o)^2}{\sigma_z^2} \right) \right) \quad (4.8)$$

where A is the maximum intensity, x_0 is the ion position along the x direction, σ_x is the $1/e^2$ size of the image along the x direction, z_0 is the ion position along the z direction and σ_z is the $1/e^2$ size of the image along the z direction.

M2_Calc receives the ion image sizes and the corresponding camera positions as input and outputs M^2 , focus positions and focus sizes for the two axes, by fitting the equation 4.7 to the data. An example of the output of this program for the light from the ion is shown in Fig. 4.7.

4.3 Imaging Using Microfabricated Collimators

After the initial trapping, in the first attempt, we tried to capture an image using the collimator at loading zone. This part of the experiment was discussed in section 2.3.4. The next step was to shuttle the ion to 4th collimator on the chip, according to procedure discussed in section 2.2.1 .

The optical telescope, used in bulk imaging, does not focus the light reflected from the

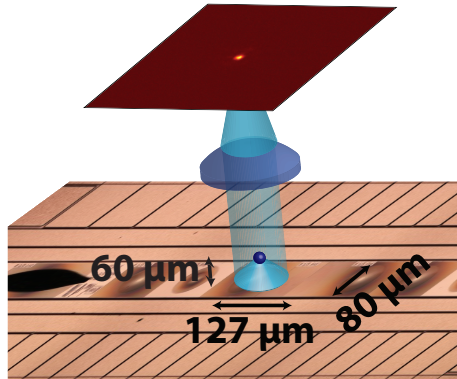


Figure 4.8: Imaging using integrated collimating mirrors. The collimated light can be focused on the screen using a second lens. This method can be used if the distance between the mirror and the axillary lens is less than Rayleigh range of the beam which is 8.7 mm for one axis and 5.1 mm for the other axis. In our system the distance between the mirror and the first lens is 60 mm . This distance is much greater than the Rayleigh range of the beam and beam is diverging when it reaches the lens. Gaussian beam simulation must be used to predict the evolution of the beam and to design an optical system to image the light collected with the mirrors.

diffracted mirrors on the camera screen.

To focus and image the light from the mirrors, we need to change the setting of this optical system or add some more lenses to bring the light into focus. To be able to easily switch between the two modes, we left the bulk imaging lenses untouched and decided to add lenses to the system to focus the light collected by the mirrors. To setup this new imaging system we needed to predict and calculate the beam behaviour through the optics. One might naively think that the ion light from the collimator remains collimated until it reaches the first objective lens and then it can be focused by this lens (Fig. 4.8). Correctness of this assumption depends on the Rayleigh range of the beam and the distance between the mirror and the lens. The calculation of the Rayleigh range for an ideal Gaussian beam collected for the 4th collimator on the chip, shows that the Rayleigh range is 8.7 mm for the larger axis of the beam and 5.1 mm for the smaller axis of the beam. This shows that after travelling 60 mm to the first objective lens, the beam is not collimated any more. In fact at this point the beam is in the far-field diverging regime. The minimum divergence angle (for the ideal beam) is 3.2 mrad and the spot size at the 60 mm lens is 0.22 mm by 0.29 mm . The size is 12.1X and 6.9X larger than the original size of the

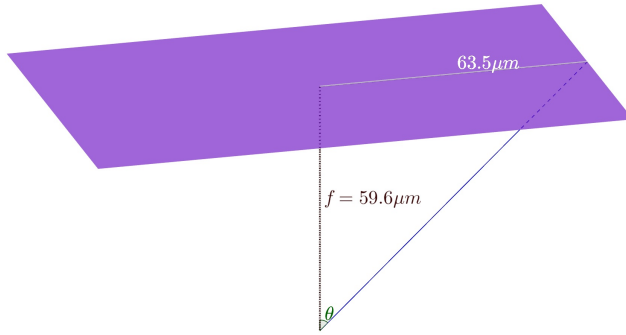


Figure 4.9: Numerical aperture (NA) of the mirror for the z axis. The distance from the ion to the mirror is $59.6 \mu m$ and the half side of the mirror along the z axis is $127 \div 2 = 63.5 \mu m$. Therefore $NA = \sin(\theta) = 0.73$.

beam at the mirror respectively.

The calculation of Rayleigh range was made by assuming that the beam starts with diffraction limited spot size at the ion position. Ion is located a focal length away from the mirror which is $59.6 \mu m$ for the 4th collimator. Based on equation 4.3, the diffraction limited size depends on the mirror NA which is different for the two axes. Along the translation axis for shuttling, which we call z axis, $NA = \sin(\theta) = 0.73$ (Fig. 4.9) and perpendicular to this direction (x axis) $NA=0.56$. The $1/e^2$ diffraction limited size calculated using equation 4.3 is $285 nm$ for the z axis and $218 nm$ for the x axis. From the ion position to the mirror, the beam evolves according to equation 4.4 and using this equation shows that the size at the mirror is $32 \mu m$ for the z axis and $24 \mu m$ for the x axis. The mirror collimates this diverging beam coming from the ion. The spot size of this collimated beam is $32 \mu m \times 24 \mu m$ and this is equivalent to Rayleigh range of $8.7 mm$ and $5.1 mm$. After travelling $60 mm$ to the objective lens the beam is closer to a diverging beam from a point source rather than a collimated beam. Due to the different spot sizes in two axes, we observe astigmatism. To be able to predict the behaviour of the beam, I developed a simulation program with MATLAB(TM) that is explained in the next section.

4.3.1 Gaussian Beam Propagation Simulation

To simulate the behaviour of the light from the ion we used ABCD analysis [84]. In this type of analysis for Gaussian beams, we use the beam complex parameter q :

$$\frac{1}{q(y)} = \frac{1}{R(y)} - \frac{i\lambda}{\pi w(y)^2} \quad (4.9)$$

Where R is the radius of curvature, i is the imaginary unit, λ is the wavelength of the light and w is the beam waist. The evolution of the beam in free space is based on:

$$q(y') = q(y) + d \quad (4.10)$$

Where d is the distance between y and y' . When a beam goes through a thin lens with focal length f , q' after the lens is:

$$q' = \frac{q}{1 - \frac{q}{f}} \quad (4.11)$$

I wrote a MATLAB routine (appendix D) to use these equations to simulate the propagation of the beam. The MATLAB routine receives mirror size, ion distance from the mirror, lens positions and lens focal lengths as input. In the first step the program calculates NA for the two axes based on mirror size and ion distance from the mirror. Having NA, it uses equation 4.3 to calculate the ideal size of Gaussian beam at the ion. From here it uses equation 4.10 to calculate q just before the mirror. The next step is to apply equation 4.11 to calculate q just after the mirror. From here it calculates evolution of q in free space with steps of one mm and applies lens effect where it reaches a lens.

To prepare an output it calculates an array of beam sizes, w , and radius of curvature, R , for each mm using equations below:

$$R = \frac{1}{Re(1/q)} \quad (4.12)$$

$$w = \sqrt{-\frac{\lambda}{Im(1/q)\pi}} \quad (4.13)$$

Where λ is the wavelength, $Re()$ is function that returns real part of a complex number and $Im()$ is a function that returns the imaginary part of a complex number. The program also calculates the Rayleigh range after each lens and identifies focus points and their sizes and magnifications. Finally it plots the evolution of the beam for two axes and adds the calculated values to the graph.

Fig. 4.10 shows the output of the program for one of the optical setups that we use for beam transfer.

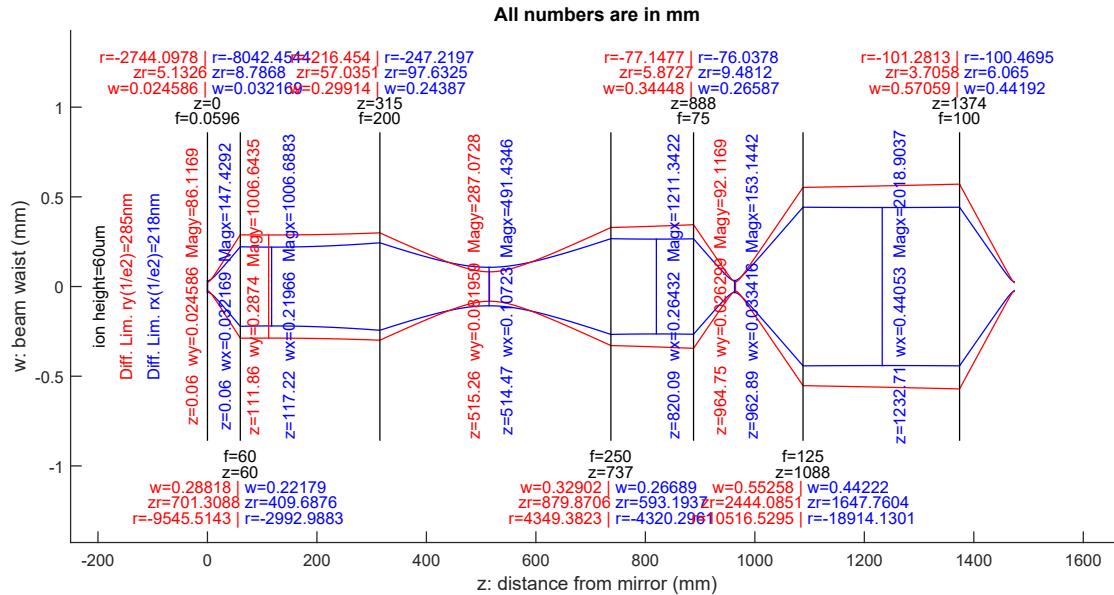


Figure 4.10: Gaussian beam propagation simulation (appendix D) for one of the settings we used for beam transfer. Blue curve shows the size of the beam in the x direction and red curve shows the size of the beam for z direction. Vertical black lines are lenses with f their focal lengths and z their distances from the diffractive mirror. r , zr and w labels, next to the focal length label, are radius of curvature, Rayleigh range and beam size respectively. Vertical blue and red lines show the focus points and for each axis the beam size, focus position and magnification is shown with respective color next to them. On the left side of the output graph, the program displays the diffraction limited size at ion position for each axis.

4.4 Near Diffraction-limited Image

After simulating the beam propagation and setting up required optics, we captured images using different collimators that we have on the chip. The camera that we used for this imaging was an Andor Luca DL-658M-TIL. The detector chip is an array of 658×496 pixels with dimensions of $10 \times 10 \mu\text{m}$.

The focal lengths of the four collimators on the chip were $58.6(+0)$, $60.6(+2)$, $62.6(+4)$, $59.6(+1) \mu\text{m}$. The ion is more stable when its height is at nominal $58.6 \mu\text{m}$ or lower therefore we expected to get the best image with our first collimator in the array which has a focal length of $58.6 \mu\text{m}$. We captured an image using this collimator but unfortunately it is too close to the loading zone and ion is unstable at this position. This is because near this zone, the hole for the loading zone changes the field pattern from ideal. Gradual deposition of neutral Yb on the back side of the loading zone makes the situation worse and over time the ion becomes more unstable around this area.

Another more important problem with this collimator was that when we tried to

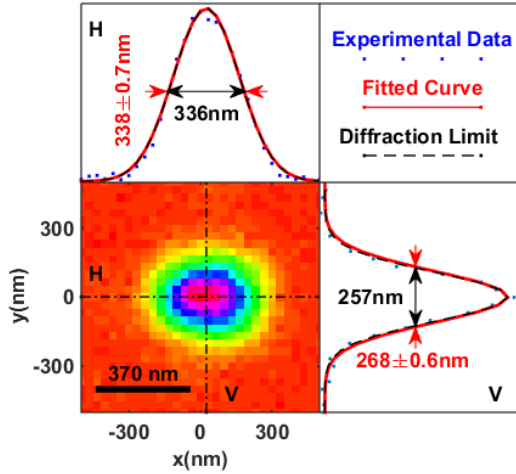


Figure 4.11: Near diffraction limited image of an $^{174}\text{Yb}^+$ ion obtained using integrated diffractive mirror and comparison with diffraction limited size. Solid angle coverage is 13.3% and exposure time is 1 second. Ion image size measured to be $338(1.6)$ nm \times $268(1.2)$ nm FWHM diameter.

position the ion at the center of this collimator in the z direction (along RF lines) we captured a distorted image which was apparently being blocked partly by some object. This object turned out to be the conducting mesh on the top of the chip that is placed to protect the chip from stray fields. The wires of the mesh are very thin (about $25\ \mu\text{m}$) and it does not have any visible effect on the normal external imaging but unfortunately one of the mesh lines is located directly above the center of this collimator and blocks part of the image. The effect on the total collection is small but it prevents high resolution imaging and high fibre coupling efficiency. Therefore it is only possible to image the ion by positioning ion $1\ \mu\text{m}$ away from the center of the collimator in the z direction. This adds aberration to the image and increases the M^2 value of the beam. this means that the beam size becomes greater than the diffraction limited size.

The next best option was the 4th collimator which has a focal length of $59.6\ \mu\text{m}$ ($1\ \mu\text{m}$ higher than nominal height). To capture an image we set-up the optical system shown in Fig. 4.10. In general it is not necessary to have 6 lenses to image in this mode. The first two lenses are the ones that we use for bulk imaging and we did not want to remove them. The remaining lenses are only used for resizing the beam for the fibre coupling experiment (section 6.2). In principle only one lens is enough to focus the light on camera if there are no positioning and distance constraints. Using this system we captured the image shown in Fig. 4.11.

To be able to capture this nearly diffraction limited image, we needed to optimize two important set of parameters:

1. external optics positioning and orientation
2. ion position relative to diffractive mirror

To have the best image, the light from the ion must go through the center of the external lenses and must be perpendicular to the lenses. To align the first two lenses in the setup , *i.e.* the $f = 60\text{ mm}$ objective lens and the $f = 200\text{ mm}$ lens, we mounted them on 3-axes translators for accurate positioning and adjustable mirror mounts to set the angle. We attached two irises before and after each lens and iteratively made irises tighter and tighter and optimized position and angle to get clearest and brightest image of the surface of the chip.

The next task was to optimize the ion position. Our convention for direction is to label the axis along the RF lines z , perpendicular to the chip surface y and the lateral direction x . Along the z direction the DC harmonic potential confines the ion so we can position the ion finely without adding to the micro-motion. For this alignment, we have an accuracy of 100 nm on the control program. From our design we know the position of the centre of the mirror within few μm . The field of view in this direction is $2\text{ }\mu\text{m}$. Within the field of view we capture a round and clear ion image but outside the field, the ion image starts to become distorted. We set the ion position to the center of this region. This center is located at $871.1\mu\text{m}$ away from the loading point.

Along the x direction we move the ion using a set of voltages named `Ex_Comp` waveform (see section 2.2.1). This set of voltages are designed to apply 1000 V/m to the ion along the x direction. We use a scalar parameter `Ex_Comp_Weight` to scale this electric field and apply the desired field to the ion. Moving the ion in this direction increases the micro-motion of the ion and eventually leads to the loss of the ion. Even though the best E_x for cancelling the stray fields is position dependent, `Ex_Comp_Weight` is usually between -0.2 and $+0.2$. This is equivalent to applying an electric field between -200 to $+200\text{ V/m}$ to the ion. Normally we lose the ion when the `Ex_Comp_Weight` is set to greater than 0.7 or smaller than -0.7 . At the center of the 4th collimator, `Ex_Comp_Weight=0.1` is the best field that minimizes the micro-motion. We find this parameter by setting the laser frequency -5 MHz detuned from resonance and find the `Ex_Comp_Weight` that maximizes the ion fluorescence in external imaging mode. For imaging with the collimator we capture a round small image for $0 < \text{Ex_Comp_Weight} < 0.4$. Outside this range the image becomes skewed and the image size starts to increase. We use `Ex_Comp_Weight=0.2` for imaging and this does not have a significant effect on the micro-motion.

Position in y direction or the ion height is the most important parameter that can affect the image quality. Ideally we want to have the ion exactly at the focus of the collimator. The nominal ion height is shown in figure 4.12. This is based on simulation of the RF and DC field done by GTRI and never confirmed experimentally. Therefore we can only roughly guess that the ion height is $58.6\text{ }\mu\text{m}$ when we apply no field along the y direction.

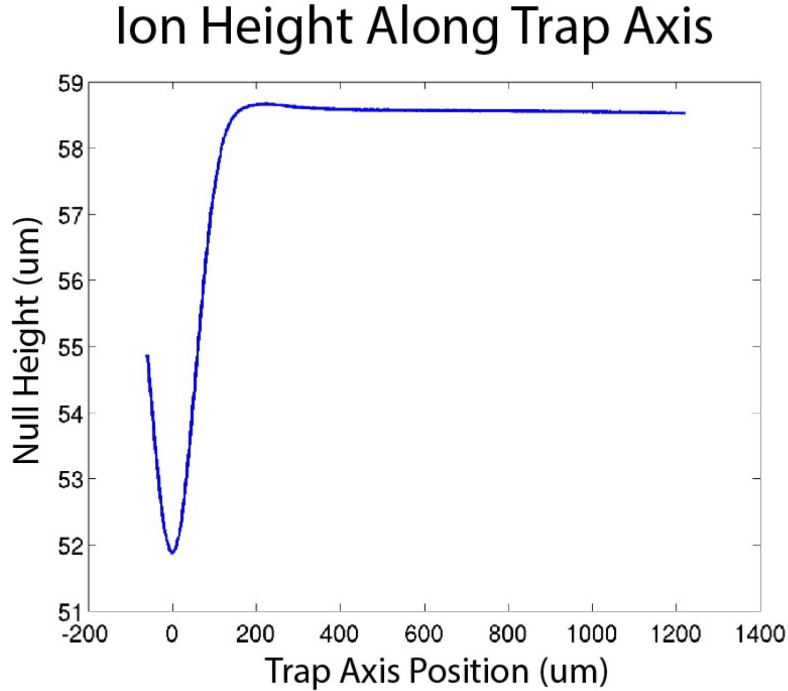


Figure 4.12: The ion height for the different positions of the ion on the chip. When at the middle of the loading zone the ion height is $52 \mu m$. Ion height gradually increases by moving away from the loading point and becomes $58.6 \mu m$ outside of the loading zone. (graph after GTRI)

For the 4th collimator with the focal length of $59.6 \mu m$ we need to apply a positive E_y (away from surface of the trap) to push the ion $1 \mu m$ higher but the exact amount of electric field for this displacement is also unknown. To find the right height we used the imaging simulator described in section 4.3.1. We created a list of different ion heights and simulated the image focus position relative to the last lens before camera. Then we applied a set of different E_y fields and created a table of E_y vs camera focus point. Because the dimensions of our mirror are asymmetric, the image suffers from astigmatism and this makes it hard to recognise the focus point. For each ion height we saved a set of five images around the focus point and fitted a Gaussian beam profile to find the focus for each axis. By comparing to the simulation we found out that `Ey_Comp_Weight=0` corresponds to the height of $58.6 \mu m$ and `Ey_Comp_Weight=0.5` corresponds to the height of $59.6 \mu m$. We confirmed these results by doing the same procedure for the 1st collimator with the focal length of $58.6 \mu m$.

After finding all the right parameters and aligning external optics we captured the image shown in Fig. 4.11. To be able to compare the image size with the diffraction limited size, we scaled the image size on camera by the magnification of the optical system. To measure the magnification, using the control program, we shuttled the ion $1 \mu m$ towards

the $-z$ direction and $1 \mu\text{m}$ towards the $+z$ direction and captured two images. We fitted a Gaussian profile to these images and knowing the camera pixel size, which is $10 \times 10 \mu\text{m}$, we calculated that it moves $780.0(2) \mu\text{m}$ which is equivalent to Magnification of 390X.

Fitting a Gaussian profile to the captured ion image and dividing the sizes by magnification of 390 we arrive at near diffraction limited spot size of $338(0.7)$ nm horizontal (H) and $268(0.6)$ nm vertical (V), FWHM diameter. This image is only slightly larger than the diffraction limited size of 336 nm (H) and 257 nm (V) (0.6% for horizontal and 4% for vertical).

To characterize the mode quality we took 5 images of the ion by defocusing the camera around the focus point and found the M^2 of the beam as described in section 4.2. The M^2 , mode quality, of the spot was $1.36(0.17)$ (H) and $1.54(0.10)$ (V), compared to an ideal Gaussian beam with $M^2 = 1$. Other than design imperfections, this slightly non-ideal behaviour is driven by the increased divergence in the beam due to astigmatism and the fundamentally non-Gaussian distribution of the ion's photon emission.

CHAPTER 5

Single Photon Generation

To rigorously measure the collection efficiency of the diffractive mirrors, we designed and implemented a single photon generation scheme. This is also a demonstration of a quantum mechanical application and could be used for quantum communication.

The conventional method for measuring collection efficiency is to use the fluorescence from the cooling cycle. It is possible to calculate photon emission rate for a certain laser intensity and by comparing it with the number of detected photons, the collection efficiency can be calculated. The fluorescence counts depend on the intensity of the laser and the frequency detuning from the resonance. The fluorescence rate for a two-level atom is given by [75]:

$$\gamma_p = \left(\frac{s_0}{1+s_0} \right) \left(\frac{\gamma/2}{1 + (2\delta/\gamma\sqrt{1+s_0})^2} \right) \quad (5.1)$$

where s_0 is the saturation parameter which is proportional to the laser intensity (see section 3.1), γ is the linewidth of the transition in rad/s and δ is the detuning from the resonance. For this calculation to be accurate the laser frequency linewidth must be much narrower than transition linewidth which is the case in our experiment. The repumper laser power must also be saturating its transition and laser powers must be stabilised to make sure that the intensity remains constant. Another important point is to measure the beam size at the ion precisely to calculate the intensity. With on-demand deterministic single photon generation, we do not need to rely on the accuracy of these assumptions. We generate a predictable number of photons and compare them with the number of the collected photons.

5.1 Atomic Transitions, Absorption and Emission Patterns

In the process of generating single photons, to excite the ion, we use lasers with circular polarisations. In this process the emitted photons - depending on the transition and the orientation of the emission - can have linear, elliptical or circular polarisation. In order to explain the protocol, it is necessary to know the absorption and emission patterns for these polarisations.

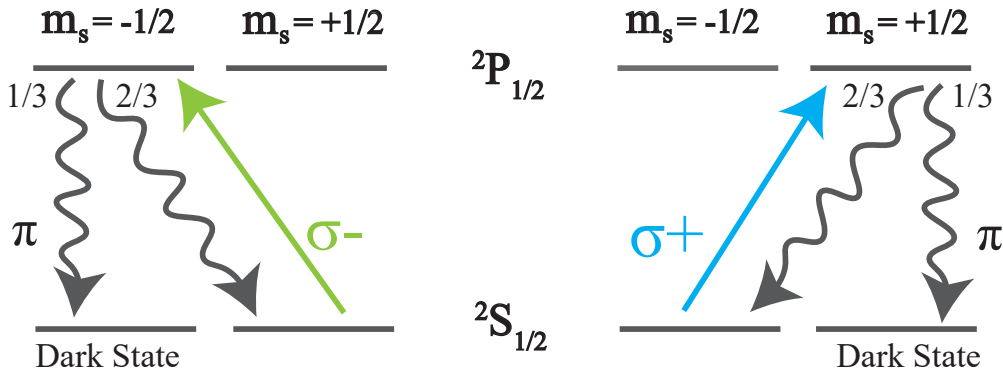


Figure 5.1: Relevant transitions for the single photon generation protocol. The 370 nm σ^- laser can only excite $^2S_{1/2} m_j = +1/2$ to $^2P_{1/2} m_j = -1/2$ transition. The excited ion may emit a σ -photon, with probability of $2/3$, and return back to $m_j = +1/2$ ground state or it may emit a π -photon, with probability of $1/3$, and decay into $m_j = -1/2$ state. This is a dark state for σ^- laser and the ion does not interact with the laser while in this state. For the σ^+ laser, after excitation, the ion will undergo the same type of decaying and emission as the case for σ^- laser. The only difference is that it can only excite $m_j = -1/2$ ground state but not $m_j = +1/2$ ground state.

For our single photon generation protocol, we use the usual $^2S_{1/2}$ - $^2P_{1/2}$ cooling transition at wavelength of 370 nm. Figure 5.1 shows the transitions that can be driven by σ^+ and σ^- 370 nm lasers. The σ^- laser can only excite the ion to the $^2P_{1/2} m_j = -1/2$ state when it is in $m_j = +1/2$ ground state.

From the $m_j = -1/2$ excited state, with probability of $2/3$, the atom decays into the $m_j = +1/2$ ground state by emitting a σ -photon or with probability of $1/3$, decays into the $m_j = -1/2$ ground state by emitting a π -photon. In the $m_j = -1/2$ ground state the ion does not interact with the σ^- laser any more. On average the ion emits two σ -photons, before it emits the single terminal π -photon and goes to the dark state.

From the $m_j = -1/2$ ground state, the σ^+ laser can excite the atom into the $^2P_{1/2} m_j = +1/2$ state. Again the ion may emit a π or σ -photon and in the case of emitting a π -photon, likewise it falls to the dark state for the σ^+ laser.

Figure 5.2 shows the anisotropic intensity patterns for the π and σ photons. For the π transition, the intensity is maximum perpendicular to the magnetic field and zero along the magnetic field. For the σ photons the transition rate is maximum along the magnetic field and decreases to half in the direction perpendicular to the magnetic field.

The emission pattern of a π transition is the same as the emission pattern of an oscillating electric dipole along the z direction:

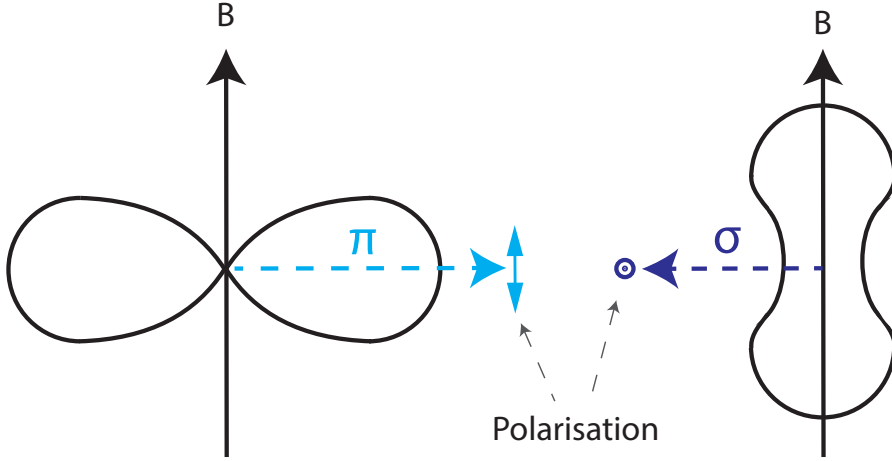


Figure 5.2: Emission patterns of the π and σ polarised photons. Left: For the π -photons the maximum probability of emission is perpendicular to the magnetic field. No π -photon is emitted along the magnetic field direction. Right: The probability of emission of σ -photons along the magnetic field is twice the probability perpendicular to the magnetic field. Both polarisations are linear, if they are emitted perpendicular to the magnetic field. In this direction polarisation of the π -photons is along the magnetic field and polarisation of the σ -photons is perpendicular to the magnetic field.

$$\vec{E}_\pi(r, \theta, t) = \frac{\mu_0 p_0 \omega^2}{4\pi r} \sin(\theta) \cos(\omega t - \omega r/c) \hat{\theta} \quad (5.2)$$

which has the amplitude of:

$$\vec{E}_\pi(r, \theta) = \frac{\mu_0 p_0 \omega^2}{4\pi r} \sin(\theta) \hat{\theta} \quad (5.3)$$

For a σ transition, the emission pattern is the same as a rotating dipole around the z axis:

$$\begin{aligned} \vec{E}_\sigma(r, \theta, t) &= \frac{\mu_0 p_0 \omega^2}{4\pi r} \cos(\theta) \left(\cos(\omega t - \omega r/c) \cos(\phi) + \sin(\omega t - \omega r/c) \sin(\phi) \right) \cos(\omega t - \omega r/c) \hat{\theta} \\ &\pm \frac{\mu_0 p_0 \omega^2}{4\pi r} \left(\cos(\omega t - \omega r/c) \sin(\phi) - \sin(\omega t - \omega r/c) \cos(\phi) \right) \cos(\omega t - \omega r/c) \hat{\phi} \end{aligned} \quad (5.4)$$

with amplitude of:

$$\vec{E}_\sigma(r, \theta) = \frac{\mu_0 p_0 \omega^2}{4\pi r} \left(\cos(\theta) \hat{\theta} \pm i \hat{\phi} \right) \quad (5.5)$$

For these emissions, the polarisation quantum state functions are:

$$|\pi\rangle = \sin(\theta)|\hat{\theta}\rangle \quad (5.6)$$

$$|\sigma_{\pm}\rangle = \frac{e^{\pm i\phi}}{\sqrt{2}} (\cos(\theta)|\hat{\theta}\rangle \pm i|\hat{\phi}\rangle) \quad (5.7)$$

Where θ is the polar angle with respect to \hat{z} and ϕ is the azimuthal angle. $\hat{\theta}$ and $\hat{\phi}$ are the unit vectors in spherical coordinates.

For the π polarised light, the probability of emission is proportional to $\sin^2(\theta)$ which means that it is zero along the z direction and maximum perpendicular to the z direction. The polarisation is always linear and along the $\hat{\theta}$.

For the σ transition, the probability of emission along a direction with the polar angle of θ is proportional to $1 + \cos^2(\theta)$. This means that the probability of emission along the z axis is double the probability of emission perpendicular to the z axis. For the limit that θ approaches 0, the wavefunction takes the form $|\hat{\theta}\rangle \pm i|\hat{\phi}\rangle$ which is a circularly polarised light. With a finite θ the polarisation becomes elliptical and at $\theta = \pi/2$ it becomes linear along $\hat{\phi}$ and perpendicular to the polarisation of the π polarised light which is along $\hat{\theta}$.

The absorption pattern is exactly the same as the emission pattern. The higher the probability of emission in a particular direction, the higher is the probability of absorbing a photon along that direction. Therefore to maximise the absorption of σ polarised photons one must align the direction of the laser to the direction of the magnetic field. For the lasers with linear polarisation, the best direction is to have it perpendicular to the magnetic field and set the direction of the polarisation parallel to the magnetic field.

5.2 Single Photon Generation Protocol

The single photon generation protocol is based on the optical pumping of the ion with two 370 nm lasers with σ^+ and σ^- polarisations. Interaction of these lasers with the ion is explained in section 5.1. The σ^- laser prepares the ion and the σ^+ laser generates a single π -photon. The protocol is depicted and explained in Fig. 5.3. The sequence shown in this figure is repeated to generate single photons. Each repetition starts with a cooling cycle. When any of the lasers are on, after a few cycles, the ion goes to the dark state for that laser. Therefore we need to keep both lasers on to have a continuous excitation and emission process to cool the ion. The next step is the preparation step. To prepare the ion, we only keep the σ^- laser on. In this step the ion may emit a σ -photon with probability of $2/3$ and return back to $m_j = +1/2$ ground state but finally it emits a π -photon and falls into the $m_j = -1/2$ ground state. This is a dark state for this laser.

To separate the preparation and generation steps we turn the detection on 750 ns after

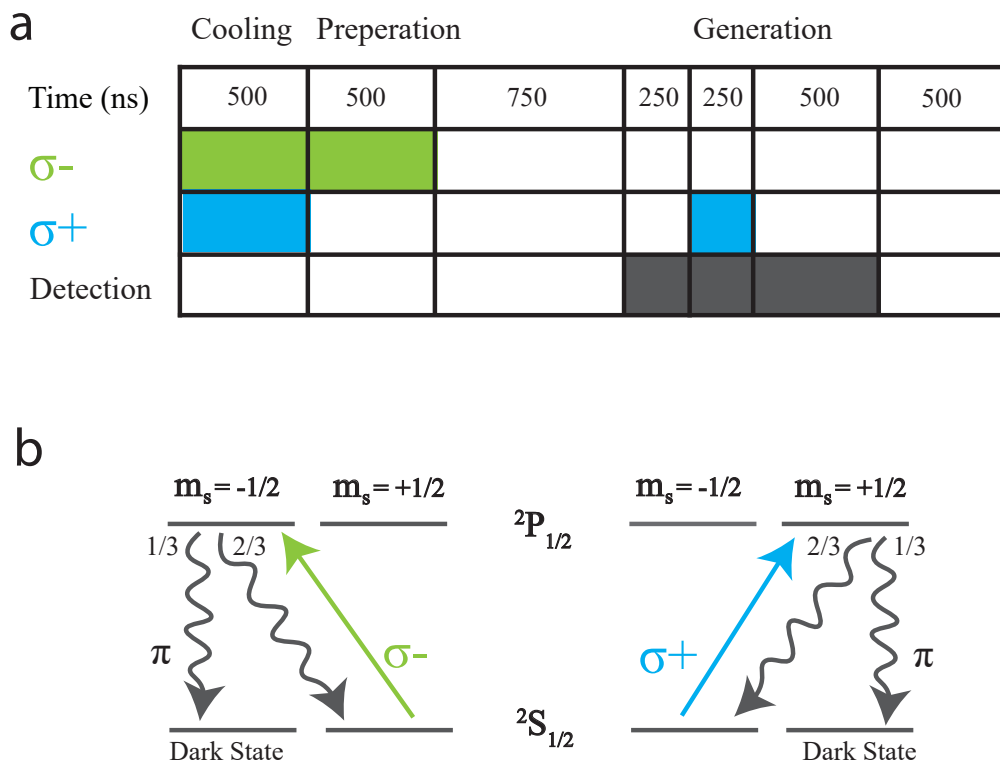


Figure 5.3: a. Single photon generation protocol. 370 nm σ^- and σ^+ lasers are on for 500 ns to generate a continuous excitation cycle to cool the ion. Then only the σ^- laser remains on for another 500 ns to prepare the ion in the $m_j = -1/2$ ground state. For 1000 ns both lasers remain off to separate the preparation process from generation process. Detection is turned on 750 ns after the preparation and remains on for 1000 ns. 1000 ns after preparation, σ^+ generation laser is turned on and remains on for 250 ns. This generates two σ -photons on average and finally the ion emits a π -photon and goes to the dark state. By filtering the σ -photons using a polariser, only one photon is collected during the generation step. b. Relevant transitions for single photon generation protocol. (for details on transitions see section 5.1 and Fig. 5.2)

the preparation. 250 ns after turning on the detection, the generation laser is turned on. For the single photon generation step we use the σ^+ laser. When the ion is excited by this laser, it goes to the ${}^2P_{1/2} m_j = +1/2$ state. From here the ion spontaneously emits a photon and returns back to the ground state. There is a 2/3 chance for the ion to return to $m_j = -1/2$ and emit a σ -photon. If this happens the σ^+ laser excites the ion again to the same excited state. There is also a 1/3 chance for the ion to emit a π -photon and drop to the $m_j = +1/2$ ground state. This is a dark state for the σ^+ laser and no photon will be scattered in this state. On average the ion emits 2 σ -photons and then goes to the dark state by emitting a π -photon. To generate only one photon in each generation step, we need to filter out the σ -photons and only detect the π -photons.

As it is explained in section 5.1, all photons that are emitted perpendicular to the magnetic field direction have linear polarisations. For a π -photon this polarisation is along the magnetic field and for a σ -photon it is perpendicular to the magnetic field. This means that if we set our imaging axis perpendicular to the magnetic field (on the equatorial plane), we can use a polariser to filter the σ photons and collect only π -photons.

Going away from the equatorial plane, photons from σ transition start to have a polarisation component along $\hat{\theta}$ (see section 5.1) and are transmitted by the polariser with probability of $\cos^2(\theta)$; this effect is called polarisation blurring and for the optics with high numerical aperture this effect can be significant.

To estimate the collection efficiency for σ and π -photons and the polarisation blurring, Erik Streed has developed a program in Mathematica(TM). In our experiment, the mirror dimensions are $80 \times 127 \mu\text{m}$ and the ion height is $59.6 \mu\text{m}$. The direction of the magnetic field (and the laser) is parallel to the surface of the mirror and creates a 45° angle with the mirror sides. In this configuration mirror's NA is 0.55×0.73 which is equivalent to circular NA of 0.68. The mirror covers 13.3% of the total solid angle. This mirror collects 17.4% of the π light and 11.3% of the σ light.

In the process of characterising the mirror collection efficiency, we reduced the NA to reduce the polarisation blurring. To do this we used an iris in the cooling mode (both σ^+ and σ^- lasers on) to reduce the counts to 50%. With this configuration the program shows that the expected second order correlation $g^{(2)}$ will be equal to or greater than 0.069 (see section 5.6).

5.3 Automatic Control Of The Lasers and The Detectors Using LabVIEW FPGA

To perform the single photon generation protocol, one important requirement is the ability to turn the lasers and the detectors on and off very accurately in time. To perform this task, I developed a program in LabView(TM) to control the digital and analogue outputs

of the LabView(TM) FPGA RIO0 PCI-7833R card. This program can control the on/off time of the outputs with the accuracy of 25 ns . This accuracy is limited by the device clock cycle and not the program's algorithm. A screenshot of the program's user interface is shown in Fig. 5.4. In this program it is possible to define a sequence of actions, simultaneously on all outputs, then repeat it by the number given in the "Number of Repetitions" input. The input array, "Element Clock Cycles", enables the user to divide each single repetition to a number of elements. The user can determine the length of each element individually and during each element, turn each digital input on or off or change the value of an analogue output. The shortest length for each element is one clock cycle of the FPGA card. The vertical inputs given on the left side of the digital and analogue inputs can be used to determine the default status of the outputs, when the sequence is not running. The rows "DIO 14" and "DIO 15" show the number of detected photons from two photon detectors. These outputs show live accumulation of counts separately for each element, during the repetition of the sequence. When the sequence is not running the counts/s for each detector can be read from "DIO 14 Idle Counts(/s)" and "DIO 15 Idle Counts(/s)".

The underlying algorithm of the program is composed of two main block diagrams (in LabVIEW(TM) programming, a graphical unit of codes is called block diagram). One of them consists of the codes that are executed on the host computer and is called `Host_main`. The other block diagram is the code that is executed on the the FPGA chip and is called `FPGA_main`. The communication between the two is through a set of commands that are called interrupts. `FPGA_main` waits for a command and the corresponding data and executes the command on the FPGA card and after finishing the task waits for the next command.

`Host_main` has two principle modes of operation: the *Idle* mode and the *Sequence* mode. The *Sequence* mode is executed when requested by the user. *Idle* mode is the default mode and is running when the *Sequence* mode is not running. In the *Idle* mode, `Host_main` alternatively sends *Counting* and *Set to Default* commands to the `FPGA_main`. For the *Counting* mode, `Host_main` provides `FPGA_main` with a time window for the detection and `FPGA_main` accumulates the counts on the detectors' inputs for a period defined by the time window and returns a counts/s value for each detector. For the *Set to Default* command, `Host_main` reads the default values for each digital and analogue output from the user interface and creates an array of values and pass it to `FPGA_main`. `FPGA_main` sets the outputs to the requested values and waits for the next command.

In the *sequence* mode `Host_main` provides `FPGA_main` with an array of time elements, values for each output during those time elements and the number of repetitions. `FPGA_main` runs a *single-cycle timed loop* that guarantees the execution of all calculations in one clock cycle (which is 25 ns). In each cycle it calculates the value of each output using the arrays provided and applies that to the outputs. During the execution of the sequence,



Figure 5.4: FPGA control program's user interface screenshot. In the default mode, the program shows counts/s for each detector with "DIO 14 Idle Counts(/s)" and "DIO 15 Idle Counts(/s)" outputs and applies the default values to the digital and analogue outputs. These default values are entered using vertical array inputs on the left side of the interface. The user can also choose to repeat a sequence of events and change the values of outputs during time. The time length of each element is entered in "Element Clock Cycles" field and the corresponding value of digital and analogue outputs can be entered under each element cell in the inputs provided for each output port. After pressing "Start Sequence" the program repeats the commands for the number of times given in "Number of Repetitions". During the execution of the sequence, the DIO14 and DIO15 outputs display the live accumulation of number of detections for each time element.

the program also saves the detection times for each detector. This data is saved in a FIFO in FPGA chip and is transferred to `Host_main` after the end of the sequence. `FPGA_main` also accumulates the number of detections for each time element in the sequence. This data is streamed to `Host_main` to be displayed live on the user interface.

To use FPGA outputs, to turn the lasers on and off, we used AOMs. Each laser goes through an AOM that is controlled by a homebuilt AOM driver. These drivers accept TTL inputs. For TTL 1 they turn the diffraction on and for TTL 0 they turn the diffraction off. Turning the diffraction off, moves the direction of the laser beam and misaligns the coupling to the fibre that goes to the trap and effectively turns the laser off at the trap.

In this protocol we need to turn the detection off for the period of the cooling and the preparation and keep it on only for the period of the generation (see section 5.2). We realised this by using Mini-Circuits(TM) ZYSW-2-50DR RF switches that received an input from FPGA and cut or connected the connection between PMT's and the time-tagger device.

5.4 Experimental Setup

The experimental preparation process for the single photon generation protocol can be divided into four main categories of setting up electronics, optics for the lasers, optics for the photon collection and setting up the magnetic field.

A schematic of the electronic devices that was used for controlling detection and lasers is shown in Fig. 5.5. The FPGA card is controlled by the program explained in section 5.3. One of the digital outputs of this card goes to TTL input of the AOM driver for the σ^+ laser. This driver turns the AOM on for TTL pulse of 1 and turns it off for TTL pulse of 0. Another digital output is connected to the TTL inputs of the AOM driver for the σ^- laser and controls that in the same manner. The third digital output of the FPGA card is split and goes to two RF switches that can switch on or off the PMT acquisition by the time-tagger. The time-tagger box is used to analyse the statistical behaviour of the time of arrival of the photons.

The lasers that we need for this protocol are two 370 nm lasers with circular polarisations of σ^+ and σ^- . The lasers have $7 \mu W$ of power and their $1/e^2$ diameter at the focus is $80 \mu m$. In the normal operation mode we already have two 370 nm lasers that go to the trap but their frequency detunings are different. One of them has a fixed -70 MHz detuning and is used to facilitate the cooling process of the hot ion at the time of trapping. For the single photon generation protocol we need both lasers to have 10 MHz detuning from the resonant frequency. Having 10 MHz detuning instead of 70 MHz, increases the chance of the absorption of the photons and decreases the time for the preparation or generation step.

We combine the 370 nm lasers with a polarising beam splitter (see section 3.10) there-

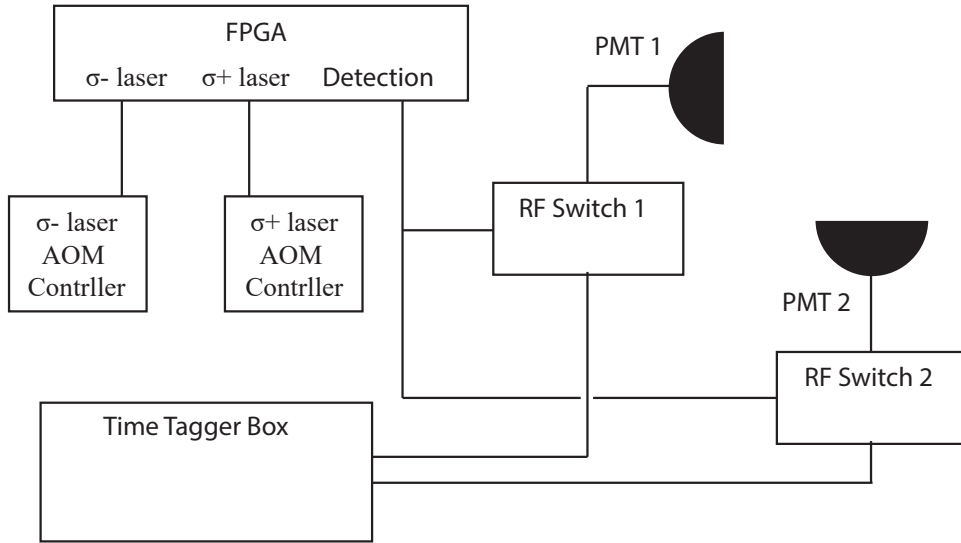


Figure 5.5: Schematics of the electronic setup for the single photon generation protocol. FPGA card controls the lasers and detection. To turn the lasers on and off, we use FPGA digital outputs to send a TTL signal to the AOM drivers. To turn the detection on and off, we use RF switches between PMTs and the time-tagger box.

fore their polarisations are linear and perpendicular to each other. To perform this protocol we add a quarter waveplate to the set-up that turns the polarisation of one of the lasers into σ^+ and the other into σ^- polarisation.

For this protocol the laser polarisation purity is very important. If the polarisations of the lasers deviate from circular, they can excite the ion when it is in the dark state and this leads to the generation of two photons instead of one during the generation step of some of the cycles of the protocol. To prepare a pure polarisation we used a Casix(TM) PN:WPZ1312- λ /4-370 zero order quarter waveplate and replaced the Thorlabs(TM) PBS102 polarising beam splitter in the beam combiner with a Thorlabs(TM) GLB10-UV-Glan-Laser alpha-BBO polarising beam splitter that has the polarisation purity of 100,000:1 for the transmitted port.

The non-trivial 68° angle of the side port of the GlanLaser polarising beam splitter makes the overlapping process hard. Due to internal reflections in this polariser, the input laser to this side port generates two modes and part of the power is lost in the second mode. The polarisation purity of the side port is lower than the through port therefore we use it for the less critical σ^- laser that is used in the preparation step.

During the experiment, the repumper laser, at 935 nm , is always on and is heavily saturating its transition. To make sure that the absorption of the σ -photons is maximised,

we set the direction of the magnetic field parallel to the laser propagation axis. Absorption is maximised in the direction that emission is maximised. Fig. 5.2 and Equation 5.5 show that the emission is maximum along the direction of the magnetic field.

To set the direction of the magnetic field along the laser, parallel to the chip surface and at a 45° angle with RF electrodes, we used three coils for vertical, 45° and -45° directions. To have the magnetic field exactly along the laser we measured earth's magnetic field and roughly set the coils' currents to the values that cancel the earth's magnetic field. Then by scanning near this point we found the Hanle resonance to make sure that magnetic field is zero [86]. The Hanle resonance is the sudden drop of the ion fluorescence when magnetic field is set to zero, and there is no preferred quantisation axis. From this point we swapped the current direction in the 45° coil to have a magnetic field only along this direction. This creates a magnetic field of about 1 G along this direction.

To collect and analyse the generated photons we used the optical set-up shown in Fig. 5.6. A set of five lenses shown in this figure is used to transfer, collimate and resize the beam. The collimated beam is sent to the polariser, shown in Fig. 5.6b, to filter σ -photons and transmit only π -photons. π -photons are sent to two photo multiplier tubes (PMTs) using a non-polarising beam splitter (NPBS) for measuring the $g^{(2)}$ of the collected light. An IDQ TDC id800 time-tagger device is used to analyse the statistics of the time delays between the detections (see section 5.6).

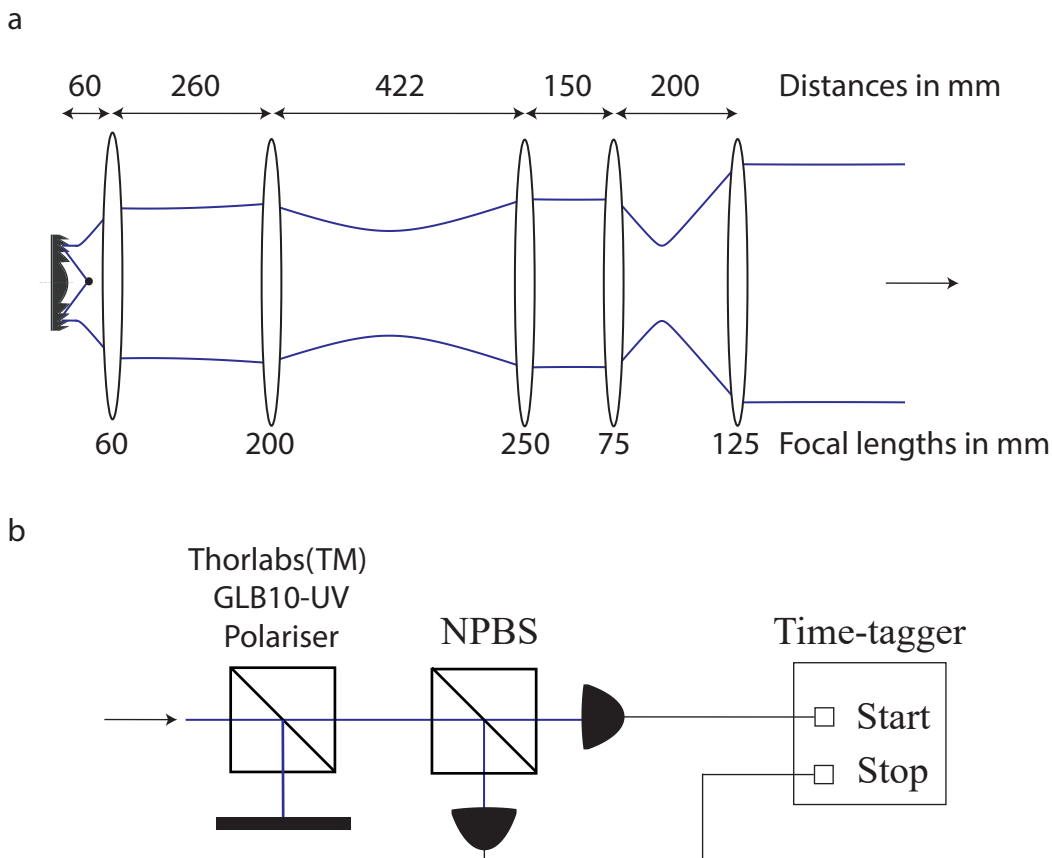


Figure 5.6: Optical set-up for the collection of the single photons. a. The optical set-up used to transfer, collimate and resize the beam to send it to the single photon analyser set-up. The first two lenses are used in the bulk imaging set-up (4.1). We leave this set-up untouched and use a $f=250\text{ mm}$ lens to collimate the light. The next two lenses ($f=75\text{ mm}$ and $f=125\text{ mm}$) act as a telescope to resize the beam. This last telescope is not necessary for this experiment and is used for mode matching for the fibre coupling experiment. b. Single photon analyser set-up. The polariser is mounted on a rotational mount to set its axis to the direction of the polarisation of the π photons and filter the σ -photons. Using a non-polarising 50-50 beam splitter, the π -photons are split and sent to the two photo multiplier tubes (PMTs). A time-tagger device analyses the statistical regime of photon emission (see section 5.6).

5.5 Characterisation Of The Time Scales and Delays

In order to synchronise the generation and the detection processes, It is important to know the delay between executing a command to turn a laser on and detecting it at the detectors. To measure this delay we used continuous fluorescence of the ion and turned the laser on for 250 ns at the start of the sequence and kept it off for 1 μs after that. We divided the off time of the laser to 50 ns elements and saved the counts for each element for 2 seconds of accumulation. The results showed that we start detecting fluorescence 500 ns after sending the command to turn the laser on.

It is also important to know for how long the generation laser needs to stay on in order to efficiently generate a single photon. In the generation step, on average, it takes three absorption and emission processes to emit a final π -photon. These absorptions are probabilistic and the chance of absorption increases exponentially with time. To measure the exponential time constant for the generation of a π photon, we ran the single photon generation sequence shown in Fig. 5.3 but extended the generation step to 10 μs . On the program we divided the generation step into intervals of 1.25 μs . This enabled us to save photons counts for each interval and analyse the time scale of the photon generation. Then we accumulated the counts for 1 minute, saved the counts for each interval and fitted an exponential function to the data. The exponential time scale of the probability of generating a single photon is 0.21 μs . A graph of data acquired and the exponential fit is shown in Fig. 5.7. This plot shows that if we turn on the σ^+ laser for 250 ns, there is a 69% chance to generate a photon.

AOM switching time is not a limitation for the time scales that we are using. The smaller the beam size is the faster is the switching time but the drawback is that the diffraction efficiency is lower for the smaller beam sizes. We use AA Optoelectronic(TM) MQ180-A0.2-UV AOMs. According to the specification [87], the rise/fall time is 110 ns/mm and is 11 ns minimum. The experimental tests of rise/fall time shows that it is smaller than 25 ns (the time resolution of the FPGA that we use for control and photon counting). This is more than 1 order of magnitude smaller than 250 ns generation time and does not have a significant effect on the generation.

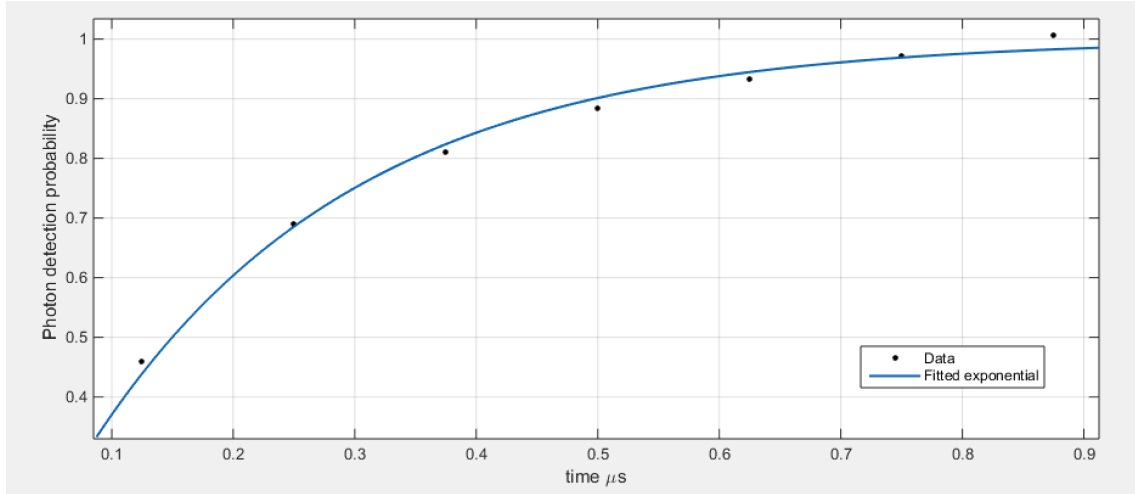


Figure 5.7: Number of photons generated in each step after time t after turning on the generation laser. The data is taken by repeating the sequence for one minute and then normalising the data to one at infinity. The blue fitted graph shows that the exponential time scale of the generation is $0.21\mu\text{s}$. This is equivalent to the average generation of 0.69π photons in 250 ns of generation.

5.6 Measuring Single Photons 2nd Order Correlation $g^{(2)}$

In order to verify that our single photon generation protocol really produces single photons, we measured the $g^{(2)}$ of the light transmitted by the polariser. The second-order correlation function $g^{(2)}(\tau)$ quantifies the intensity fluctuations of a light source. $g^{(2)}(\tau)$ is often called the degree of second-order coherence, in the classical optics books. The definition in terms of intensity is [88]:

$$g^{(2)}(\tau) = \frac{\langle I(t)I(t+\tau) \rangle}{\langle I(t) \rangle^2} \quad (5.8)$$

In an experiment, the data that we have maybe the arrival time of the photons. In this case we use the formula below:

$$g^{(2)}(\tau) = \frac{\langle n(t)n(t+\tau) \rangle}{\langle n(t) \rangle^2} \quad (5.9)$$

$g^{(2)}(\tau)$ answers this question: if we detect a photon at any time t , what is the probability of getting another one after the time delay of τ . For a photon source the average probability of sending a photon is the number of photons per unit time measured for infinitely long period. If $g^{(2)}(\tau)$ is one, the chance of getting a photon, after the time τ , is equal to average photon rate and this means that it is statistically independent of the arrival of the first photon. Lasers show this type of statistical behaviour [88]. If $g^{(2)}(\tau)$ is

smaller than one, the probability of getting the second photon after the time τ is smaller than the average probability and this means that photons are anti-bunched. This is a behaviour seen in a single photon regime. For $g^{(2)}(\tau)$ higher than one the chance is higher than the average and the photons are bunched. Thermal lights usually show bunched statistical behaviour. $g^{(2)}(\tau)$ can be different for the different time delays τ and this means that we can have bunching for some time scales and anti-bunching for the others.

In the case of ideal single photon sources, $g^{(2)}(0) = 0$. The closer to zero the $g^{(2)}(0)$ for a source is the purer is our single photon generation. In the case of analysing experimental photon counting statistics with Equation 5.9, calculating $g^{(2)}(0)$ leads to a problem. In any physical situation, photons do not arrive exactly at the same time and this means that $g^{(2)}(0)$ is always zero. To avoid this problem and get a meaningful number we need to choose a time window and if the two photons arrive within that time window, consider the event a coincidence for delay of zero. Practically this time window must be equal to or greater than the time resolution of the detector or if we are doing a process on the single photons, it must be equal or greater than the time it takes for our devices to change its settings for the next photon. In our case because the generation is deterministic and the generation cycle is $3.75 \mu\text{s}$ we count every arrival within the delays of $\pm 1.875 \mu\text{s}$ a coincidence for the time delay of 0, every arrival within the time window of $3.75 \pm 1.875 \mu\text{s}$ a coincidence for $\tau = 3.75 \mu\text{s}$ and so on.

Using the data that was collected by the time-tagger box in the experimental set-up, we plotted the graph shown in Fig. 5.8. The red peaks and the red axis on the left show the raw number of counts for different delays and the black dots and the black axis on the right show the value of $g^{(2)}$. To calculate $g^{(2)}$, we first integrated the number of counts under each peak to get the un-normalised correlation $G^{(2)}$ for each peak. To normalise the raw coincidence counts, we used the fact that $g^{(2)}(\infty)$ is 1 [89]. This is because for long enough time there will be no correlation between arrival time of the photons. To estimate the $G^{(2)}(\infty)$ we used a decaying exponential fit for the $G^{(2)}(\tau)$ and estimated the value at infinity. Using this technique we measured $g^{(2)}(0)$ of $0.12(2)$. This value is much smaller than 0.5 and this shows that our source is a single photon emitter. Black dots on the graph shows the $g^{(2)}$ for each peak. Except for the middle peak the $g^{(2)}$ is greater than one for all the other peaks. This means that we have slight bunching behaviour for the time delays equal to or greater than one generation cycle. This shows that if we get a photon in one cycle, the chance of getting another photon in the next cycle is higher than average. This is because of the slight power fluctuation of the laser on short time scales. When power is higher, it is more likely to get photons in consecutive cycles and when the power is lower it is more likely to get nothing in a few consecutive cycles.

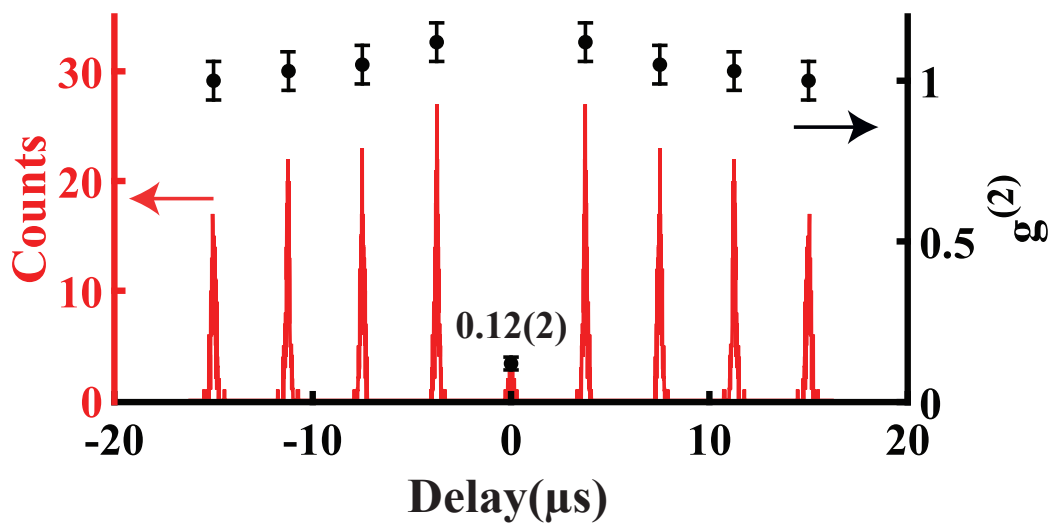


Figure 5.8: Second order correlation $g^{(2)}$ for the single photon generation protocol. The red graph and the red axis show the raw counts. To calculate $g^{(2)}(0)$ we integrated all the counts in each peak to calculate unnormalised $G^{(2)}(\tau)$ and using an exponential decaying fit estimated $G^{(2)}(\infty)$. We used $G^{(2)}(\infty)$ as the normalising factor and calculated $g^{(2)}$ for different delays. These values are shown with the black dots. $g^{(2)}(0)$ is 0.12(2).

CHAPTER 6

Efficient Fluorescence Collection With Diffractive Mirrors

This chapter covers the demonstration of efficient collection of ion fluorescence using diffractive mirrors which was the main goal of this project. Photon collection is important for many applications such as electron shelving which is the most common method of ion qubit state readout. This method is carried out by shining a laser with a specific frequency on the ion and detecting the ion fluorescence. One state produces strong fluorescence but the other state stays dark. The time that one needs to wait to discriminate between these two states is directly proportional to the fraction of the light that an optical system can collect from the ion.

For some applications free space light collection is not enough and single mode fibre coupling is needed. For example in remote entanglement, photons from two ions are collected into two single mode fibres and sent into a Hong-Ou-Mandel interferometer to post selectively entangle the ions. The probability of entangling two ions is proportional to the square of the single mode fibre coupling efficiency.

Single mode fibre coupling efficiency is also important in quantum communication applications where ion plays the role of a single photon source and a memory. Both the generation rate of a single photon source and the success rate of the storage and retrieval of the qubit is proportional to the single mode fibre coupling efficiency.

This chapter reports the demonstration of collection efficiency of the integrated diffractive mirror with free space collection and coupling into a single mode fibre.

6.1 Ion Fluorescence Collection

Conventionally the ion fluorescence is collected with bulk refractive optics. Normally the efficiency of these optics is about 2%. This efficiency can be increased up to 4% with specially designed optics but this increases aberration and an array of aberration correction optics is needed to cancel the aberration [66]. Another problem with these optics is that it is hard to use them to address ions individually, especially when aberration correction is needed. To scale the number of ion qubits, researchers are investigating small, scalable

optical interfaces ([56], [55], [59], and [61]). These small optics need to be placed very close to the ion to cover a large fraction of the total solid angle around the ion. To fulfil this requirement we designed a system with reflective optics, integrated into our chip trap. The ion is held at $\sim 60\mu m$ above the mirrors which are $127 \times 80 \mu m$ and their focal lengths ranges from 56.6 to $62.6 \mu m$ (see section 2.3). These mirrors are made by integrating diffraction rings into the ground electrode of GTRI Microwave I chip traps (see section 2.2). The diffraction pattern applies the same phase shift as a curved mirror to the phase front of the light and collimates the light from a point source that is located at the focal point of the mirror. The maximum depth of the features is only $180 nm$ and has no measured effect on the functioning of the electrode for the purposes of ion trapping. The design is wavelength dependent and is designed for $370 nm$ which is the wavelength of the main cooling transition of Yb^+ ions.

Because the mirrors are integrated into the electrodes there is no need to align them to the ion position which likewise depends on the electrode positions. The maximum misalignment that we may experience is $1 \mu m$ which is the accuracy of the alignment of the e-beam lithography process that is used to fabricate the diffractive features (see section 2.3.3. This is within the $2 \mu m$ tolerance of the optical design (see section 2.3.2).

To collect the photons efficiently, the ion must be positioned at the focus of the mirror. In our design we have four collimators on the chip that have different focal lengths. In this experiment we used the γ design that has collimators with focal lengths of 58.6 , 60.6 , 62.6 and $59.6 \mu m$ (see section 2.3.2). $58.6 \mu m$ is the design ion height in the Microwave I chip trap therefore it is the most preferable option but this collimator is too close the loading zone and the electrical effect of the loading zone makes trapping unstable. Another problem with this collimator is that a wire from the protective mesh on top of the chip is located exactly on top of this collimator and distorts the image when the ion is exactly on top of the collimator (see section 4.4). Our next best option is the 4th collimator with focal length of $59.6 \mu m$.

When the ion is placed at the focal point, the mirror collects and collimates the portion of the light that is within its field of view (FOV). Other optics maybe used to transfer or resize the beam but in principle it is possible to directly send this light to a detector.

To demonstrate the collection efficiency of the mirror we used the single photon generation protocol described in chapter 5. With this method the number of generated photons is known from the repetition rate of the protocol and comparing that with the detected photons gives us a direct measurement of the collection efficiency of the mirror.

6.1.1 Experimental Setup

The first step in preparing an experimental set-up for the measurement of the collection efficiency is to trap an ion and shuttle it to the 4th collimator. The center of this collimator

is located at $871.1 \mu m$ away from the loading point. To laterally position the ion at the focus we applied electric field of $200 V/m$ to the ion along the x direction (see section 4.4). This fine lateral adjustment does not have any effect on the collection efficiency but it improves the mode quality of the beam that increases the single mode coupling efficiency. Based on the characterisation in section 4.4, we set the E_y to $+500 V/m$ corresponding to the ion height of $59.6 \mu m$.

Once the ion is at the focus, the mirror collimates the collected light. We use the optical set-up shown in Fig. 6.1 to collect the light. In order to optimise the optical system, the behaviour of the beam was simulated with the ABCD method explained in section 4.3.1. The output of the simulation is shown in Fig. 4.10. In designing this optical system, we left the bulk optics imaging lenses untouched (see section 4.1). This part consists of two lenses with focal length of $60 mm$ and $200 mm$, placed $260 mm$ away from each other. The reason for leaving these lenses in their place is that we need to switch to bulk mode every time that we need to trap a new ion or shuttle the ion. These two lenses create a focus $172 mm$ away from the second lens and we need to use $f = 250mm$ lens $422 mm$ after the second lens to collimate the light. The extra telescope consists of $f = 75 mm$ and $f = 125 mm$ lenses is only necessary for the mode matching of the single mode fibre coupling experiment (see section 6.2).

To generate the single photons we used the protocol shown in Fig. 5.3. A compatible optical set-up needs a polariser to filter unwanted σ photons generated by the protocol. This protocol also needs an iris to reduce the effect of polarisation blurring of the σ photons for the high NA optics.

To prepare the lasers for this experiment we need to have two near resonance lasers(-10 MHz detuned) with circular polarisation of σ^+ and σ^- (see section 5.4) therefore we need to add a quarter waveplate to the beam combiner set-up, to transform the polarisations of the lasers from linear into circular.

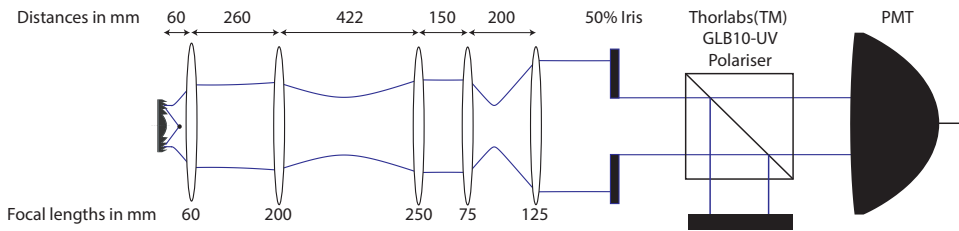


Figure 6.1: The optical set-up for the demonstration of the collection efficiency of the 4th collimator on the γ chip. The focal length of this collimator is $59.6 \mu m$. This collimator collects and collimates the light from the ion. Because of the short Rayleigh range of 8.7 and $5.1 mm$ (see section 4.3), this beam becomes divergent before exiting the vacuum chamber. The first 2 lenses are the lenses that are used for external bulk optics imaging. This part focuses the beam $172 mm$ after the second lens. A $f = 250 mm$ lens is used to collimate the light again. A final telescope consisting of a $f = 75mm$ and $f = 125mm$ resizes the beam and sends that to a PMT. In principle this complex optical set-up is not necessary for this experiment. The only reason that we used this set-up was that we wanted to use the same optical system for this experiment and the single mode fibre coupling experiment. The iris is used to decrease the counts to 50% and reduce the polarisation blurring effect. The polariser is mounted on a rotational mount and its axis is set to the direction of the magnetic field to let through the π photons and filter unwanted σ photons. This is necessary for the single photon generation protocol (see section 5.2).

6.1.2 Theoretical Estimation Of Collection Efficiency

The collection efficiency of the diffractive mirrors depends on three parameters: reflectivity of the material, diffraction efficiency of the design and solid angle coverage.

The electrodes and hence the integrated mirrors are made of aluminium. Reflectivity of the aluminium in the ultra violet range is 92%. The diffraction efficiency of the design depends on the number of levels used in diffraction profile approximation. The γ design that we use is a hybrid design. For the larger inner features($> 200 nm$), the design uses four level approximation. For this part, each step is $45 nm$ high. For the features smaller than $200 nm$ two level approximation is used and each level is $90 nm$ high. Simulation with Gsolver and GD-calc programs predict the diffraction efficiency of about 50% for this design. This number includes the reflectivity of the aluminium (see section 2.3.2).

If the ion was an isotropic emitter, the percentage of the photons that reach the mirror would be the same as the geometrical solid angle coverage. For the 4th collimator the focal length is $59.6 \mu m$ and the mirror is $80 \mu m$ wide and $127 \mu m$ long. Using the solid angle coverage formula for a rectangle we calculate 13.3% coverage:

$$\frac{\Omega}{4\pi} = \frac{1}{\pi} \arcsin \frac{ab}{\sqrt{(a^2+h^2)(b^2+h^2)}} = 0.131 \quad (6.1)$$

where $a = 40 \mu m$ is half the rectangle's width, $b = 63.5 \mu m$ is half the rectangle's length and $h = 59.6 \mu m$ is the height of the ion.

From section 5.1 we know that the emission pattern of the ions is not isotropic and has different patterns for different transitions. Here we collect π photons and our optical axis is perpendicular to the magnetic field. Fig. 5.2 shows that the probability of emission of the π photon, in this direction, is higher than the average. To calculate the probability of collecting of the π photons, we used Mathematica(TM) to numerically integrate the emission pattern (Fig. 5.2) over the area of the mirror. This calculation predicts 17.4% collection efficiency for the π photons. Together with 50% diffraction efficiency, we expect collection efficiency of 8.7%.

6.1.3 Measuring Collection Efficiency

To measure the collection efficiency of the mirror, we generate single photons according to the protocol explained in Fig. 5.3. Performing this protocol generates an average of 0.69 photons per cycle (see section 5.5) and repeating the protocol continuously is equivalent to having 2.66×10^5 cycles per second. This results in generation of 1.84×10^5 photons per second. These photons go through the optics shown in Fig. 6.1 before reaching the detector. Knowing the number of generated photons (NGP), total transmission of the optics (TR), PMT quantum efficiency ($PMTQE$), and the number of detected photons (NDP) we can calculate the collection efficiency of the mirror (CE):

$$CE = \frac{NDP}{NGP \times TR \times PMTQE} \quad (6.2)$$

We measured $NDP = 770(27)$ for the number of detected photons. The quantum efficiency of the Hamamatsu(TM) H10682-210 PMT, $PMTQE$, was measured to be 0.190(6). A list of optical transmissions for the different optical components is shown in table 6.1. The total transmission of these components is $TR = 0.38$. According to equation 6.2 this results in measured collection efficiency of 5.8(8)% for the π photons. This collection efficiency is higher compared to what has been reported for other integrated methods [59] and multimode fibre methods [58]. The efficiency is lower than the 25% obtained with the micro-mirror method [55]. The advantage over this method is that the collected light with micro-mirrors is aberrated and without aberration correction most of the light will be lost when coupling into a single mode fibre. The light collected with the diffractive mirrors has a low aberration (average M^2 of 1.45) and we demonstrate that we can couple most of the power into a single mode fibre (see section 6.2.3).

The collection efficiency is smaller than the expected 8.7% (see section 6.1.2). This

Optical Component	Transmission Rate
AR-coated vacuum window	0.995
5 AR-coated UV lenses	0.975
5 UV mirrors	0.95
Iris to limit the NA	0.5
Polariser	0.82
Total Transmission	0.38

Table 6.1: Table of the transmission rates of the optical components in experimental set-up for demonstration of the collection efficiency of the integrated mirror.

indicates that the actual diffraction efficiency of the mirror is 33% not 50%. This is most likely due to fabrication imperfections.

The collection efficiency for mixed polarisation is different from the collection efficiency for the π photons. Because of the branching ratios, on average 1/3 of the emitted photons are π photons and 2/3 of them are σ photons (see section 5.1). Numerical calculation shows that the area that the mirror covers, collects 17.4% of the π photons and 11.3% of the σ photons. If we suppose that the diffraction efficiency is the same for both polarisations, the ratio of the collection efficiencies will be the ratio of these coverages therefore:

$$CE_{\sigma} = CE_{\pi} \times 11.3/17.4 = 3.8(5)\% \quad (6.3)$$

and the mixed polarisation collection efficiency is:

$$CE_{mixed} = \frac{1}{3}CE_{\pi} + \frac{2}{3}CE_{\sigma} = 4.5(6)\% \quad (6.4)$$

To improve the collection efficiency in future projects, one option is to use a trap that has a middle electrode with a width larger than $80 \mu m$ to increase the covered area. Increasing the $127 \mu m$ side is not preferable because it is selected to match the industry standard $127 \mu m$ pitch of V-groove fibre arrays. Reducing the ion height increases the NA and collection efficiency but cannot be used due to the heating effect of the pushing of the ion away from the RF node. The other option is to use more steps in approximating the smooth profile of the diffraction rings. This option needs a fabrication method that has better accuracy comparing to electron beam lithography. Nano-imprinting is one technology that can overcome the feature size limitation imposed by electron beam lithography. One problem with this method is that the procedure applies pressure of $1 GPa$ and this is on the order of the stress fracture for the silicon wafers. Another alternative approach is to use Multi-layer gratings that can reach diffraction efficiency of 99% [90]. The only problem is that the dielectric layer used in this method can be charged. One solution to this problem can be using a transparent conducting film such as Indium Tin Oxide on top of the dielectric layer to prevent charging.

6.2 Single Mode Fibre Coupling of the Ion Fluorescence

In many applications like remote entanglement, modular quantum computing with ions, ion quantum memory and ion photon sources for quantum communication, single mode fibre coupling plays a crucial role. All of the scalable solutions for the fluorescence collection from multiple ions, like micromirrors [55], suffer from poor mode quality which limits their coupling efficiency into single mode fibre. This means that single mode fibre coupling the light collected needs aberration correction and without correction most of the light will be lost [55]. The design of the diffractive mirrors is aberration free and even though we lose part of the light due to diffraction efficiency, most of the light collected in free space can be coupled into a single mode fibre.

6.2.1 Experimental Setup

In this experiment we use the continuous fluorescence of the ion being illuminated by a $7 \mu W$ $370 nm$ laser with the spot size of $80 \mu m$ $1/e^2$ diameter, $-10 MHz$ detuned from the resonance. We compare the photon counts before the coupling lens and after the fibre to measure the fibre coupling efficiency. A schematic of the optical set-up is shown in Fig. 6.2.

For this experiment, it is very important to place the ion at the center of the mirror and set the ion height equal to the focal length of the mirror. A $2 \mu m$ offset in lateral positioning or $1 \mu m$ offset in height, increases the aberration by a large amount to the extent that it decreases the coupling efficiency by a factor of two. We set the ion position and height according to the procedure that was used for the near diffraction limited imaging experiment (section 4.4). The ion position along the z direction was set to $871.1 \mu m$. This position was chosen because it was at the middle of the range 869.1 - $873.1 \mu m$. In

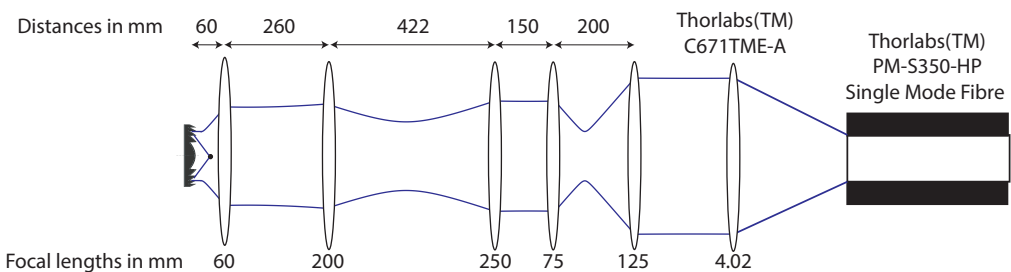


Figure 6.2: Optical set-up used for coupling ion fluorescence into the single mode fibre. The optical set-up collimates the ion light and resizes the beam to match it with the mode size of the fibre. An aspheric lens couples the light into the single mode fibre.

this range, the ion image is round and close to the diffraction limit but outside this range the image becomes visibly aberrated and skewed. The lateral position was set by applying an E_x field weight of 0.2 which is equivalent to applying electric field of 200 V/m to the ion. Again this value is in the middle of the range for which we can have a non-aberrated image. To set the ion height to 59.6 μm , which is equal to the focal length of the 4th collimator, we used upward E_y field of 500 V/m (see section 4.4). Setting the ion height is the most sensitive part of the ion positioning and mismatch of 1 μm in this direction can notably increase the aberration.

To make the beam ready for the fibre coupling set-up, we need to match the mode of the beam to that of the fibre. The coupling lens (Thorlabs(TM) C671TME-A), has a focal length of 4.02 mm. The single mode fibre (Thorlabs(TM) PM-S350-HP) has $1/e^2$ mode field diameter of 2.3 μm . Using the formula for the size of a focused Gaussian beam, we have:

$$D = \frac{\lambda f}{\pi d} \quad (6.5)$$

where D is the beam diameter before the lens, λ is the wavelength of the light, f is the focal length of the lens and d is the mode field diameter at the focus. This shows that to match the mode we need to create a collimated beam with $1/e^2$ mode field diameter of 1.03 mm before the coupling lens. In practice, because of the astigmatism, due to asymmetric dimensions of the mirror, we cannot match the size of the both axes. We tried to match the linear mean size to 1.03 mm. The simulation of the optical set-up of Fig. 6.2, shown in Fig. 4.10, predicts the size of the beam to be 0.88 mm by 1.14 mm. The measured beam size on the camera was 0.93(3) mm by 1.07(4) mm. Most probably the slight discrepancy between the predicted and measured size is due to inaccuracy in measuring the distance between the lenses and setting the ion height to the focal length of the mirror.

The next step after preparing the beam size, was to align the position and angle of the beam to the fibre. The light from the ion is of the order of fW and cannot be seen on the detection card. This makes it practically challenging to even roughly set the position of the beam to the fibre tip to get an initial signal on the PMT. To overcome this problem we used an axillary tracer laser beam. We used a flipper mirror to be able to switch between sending this laser beam or the ion light through the optical set-up. Using a neutral density filter we were able to switch between the low power (of the order of a few nW) and high power (of the order of a few μW). This laser was equipped with two adjustable mirrors to enable us to set the position and angle of this beam. We first used the low power tracer beam and overlapped it with the ion light beam. This was accomplished by marking the positions of the ion light beam on the camera at two different camera positions and iteratively changing the position and angle of the tracer beam to match both of those positions. Then we switched to high power and set our fibre coupling translator to couple

it into a multimode fibre. After maximizing the coupling into the multimode fibre we switched to the singlemode fibre and maximized it again. At this stage we switched to the light from the ion and maximized the coupling for the light from the ion. There are times that after switching to the light from the ion, no signal can be detected. If this happens the tracer beam overlapping and coupling steps must be repeated.

6.2.2 Theoretical Estimation Of Fibre Coupling Efficiency

To estimate the coupling efficiency into the single mode fibre two factors are important: Mode size matching and the quality of the beam. The mode size matching efficiency is equal to the overlap of the Gaussian profile of the beam with Gaussian profile of the fibre mode (see appendix A):

$$\eta_{size} = \frac{4w_{fibre}^2 w_x w_y}{(w_x^2 + w_{fibre}^2)(w_y^2 + w_{fibre}^2)} \quad (6.6)$$

where w_{fibre} is the $1/e^2$ radius of the fibre mode, w_x is the $1/e^2$ radius of the x axis of the beam and w_y is the $1/e^2$ radius of the y axis of the beam. In our case with $w_{fibre} = 1.15\mu m$, $w_x = 1.03\mu m$ and $w_y = 1.19\mu m$, we have $\eta_{size} = 0.99$. This shows that the slight astigmatism of the beam is not an important factor in losing the power in fibre coupling.

A rough estimate for the effect of the mode quality is to divide η_{size} by the mode quality factor M^2 :

$$\eta_{SM} = \frac{\eta_{size}}{M^2} \quad (6.7)$$

As it was measured in section 4.4, The M^2 of the beam is 1.36 (x) and 1.54 (y). This amounts to average M^2 of 1.45. Therefore the total expected collection efficiency, η_{SM} , is 0.68. This number is with the assumption that the alignment and optical quality of our coupling lens is ideal but practically even with a perfect beam in the UV range we have 80(3)% coupling efficiency. A photo of the fibre coupling stage is shown in Fig. 6.4. To measured the maximum coupling efficiency possible, we coupled the direct output of one of these coupling stages into another identical stage. One of the reasons for this loss is that in the UV range the diameter of the fibre is only $2.5\mu m$ and perfect alignment with the accuracy of our translation stages is difficult. The other reason is that the coupling lens adds some aberration to the beam.

Moreover the fibre tip is not coated and we lose some fraction of the light due to Fresnel reflection:

$$R_s = \left| \frac{n_1 \cos \theta_i - n_2 \cos \theta_t}{n_1 \cos \theta_i + n_2 \cos \theta_t} \right|^2 \quad (6.8)$$

$$R_p = \left| \frac{n_1 \cos \theta_t - n_2 \cos \theta_i}{n_1 \cos \theta_t + n_2 \cos \theta_i} \right|^2 \quad (6.9)$$

where n_1 and n_2 are the refraction indexes of the two mediums, θ_i is the angle of incidence and θ_t is the angle of the transmitted beam. Air has a refraction index of 1 and fibre core which is made of pure silica has a refractive of 1.458. For the part of the beam that passes through the center of the lens, the angle of incidence is 0, therefore $R_s = R_p = 0.035$. To roughly estimate the maximum angle of incidence we can use the ratio of the $1/e^2$ radius of the beam which is 0.51 mm and the focal length of the lens which is 4.02 mm. This is equal to 0.127 rad. For this angle of incidence we have $R_s = 0.033$ and $R_p = 0.036$. Since the intensity is much higher at the center of the beam and the change in R_s and R_p is very small even with highest angle of incidence, $R_s = R_p = 0.035$ is a good estimate for the Fresnel reflection. Therefore in total we lose 7% of the power at the two tips of the fibre due to Fresnel reflection. This does not include any losses from surface roughness or other factors.

Another source of loss is the propagation loss in Thorlabs PM-S350-HP fibres. Thorlabs does not specify the loss for this fibre and we did not measure this loss individually.

The combined effect of unmeasured coupling inaccuracy, added aberration by the coupling lens, propagation loss in fibre and 7% Fresnel reflection, leads to the measured total transmission of 80(3)%. By taking into account this transmission rate, the practical coupling efficiency that we expect is:

$$\eta_{Pr} = \eta_{SM} \times 0.80 = 0.54 \quad (6.10)$$

To find the best magnification for the resizing telescope I developed a Matlab routine (appendix E) that calculates and plots η_{size} and η_{SM} for different magnifications at the tip of the fibre (Fig. 6.3). To practically find the best magnification, we started from the top coupling point in the graph and tried the magnifications close to this value. The best telescope that we found used the $f = 125\text{mm}$ and $f = 75\text{mm}$ with magnification of 1.67 which is equivalent to magnification of 0.60 at the tip of the fibre. This leads to $\eta_{size} = 0.99$, $\eta_{SM} = 0.68$ and $\eta_{Pr} = 0.54$

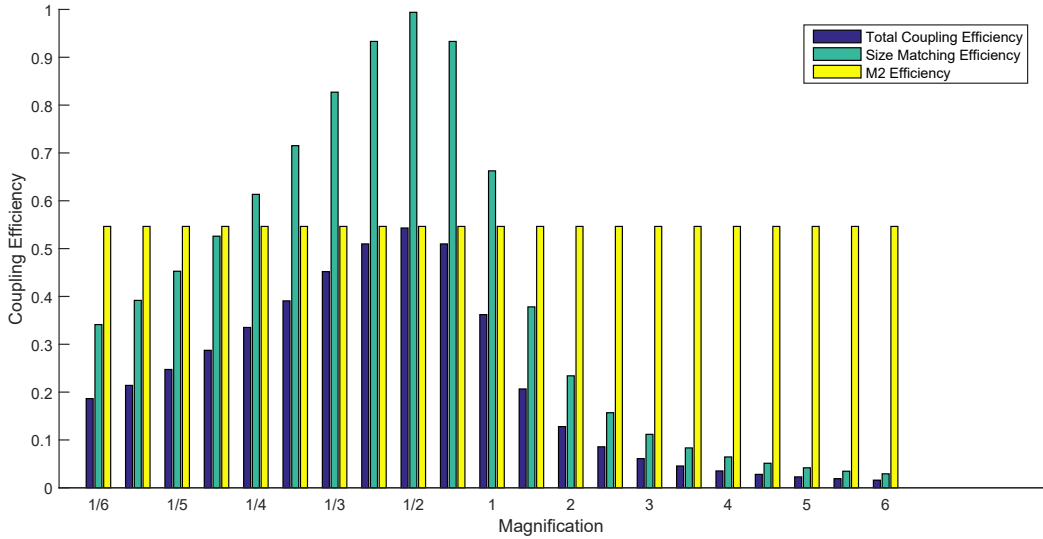


Figure 6.3: Theoretical simulation of single mode coupling efficiency. Mode size matching efficiency, effect of mode quality M^2 and total coupling efficiency is plotted for different magnifications.

6.2.3 Measuring Single Mode Fibre Coupling Efficiency

Using continuous fluorescence of the ion and a PMT we measured number of photons per second before the coupling lens and after the fibre. The background corrected counts before the fibre was 42400 ± 2200 per second and after the fibre was 23900 ± 500 per second. Therefore $\eta_{Pr} = 0.57(4)$. Taking into account the 80% transmission of the coupler and the fibre we have single mode coupling efficiency of $\eta_{SM} = 0.71(5)$. This number is close to the predicted value of 68%.

To calculate the maximum achievable total collections efficiency into a single mode fibre we have:

$$SMCE = \eta_{SM} \times CE \quad (6.11)$$

where $SMCE$ is the single mode fibre collection efficiency, η_{SM} is the single mode coupling efficiency and CE is the diffractive mirror collection efficiency. With $\eta_{SM} = 71(5)\%$ and $CE = 5.8(8)\%$ this amounts to $SMCE = 4.1(6)\%$. This is almost three times better than the previous number of 1.4% using conventional lenses [68] and can significantly increase the efficiency of quantum communication and remote entanglement of the ions.

The methods that I mentioned to improve the collection efficiency of the mirrors, also improves the fibre coupling efficiency. Improving mode quality can also improve the

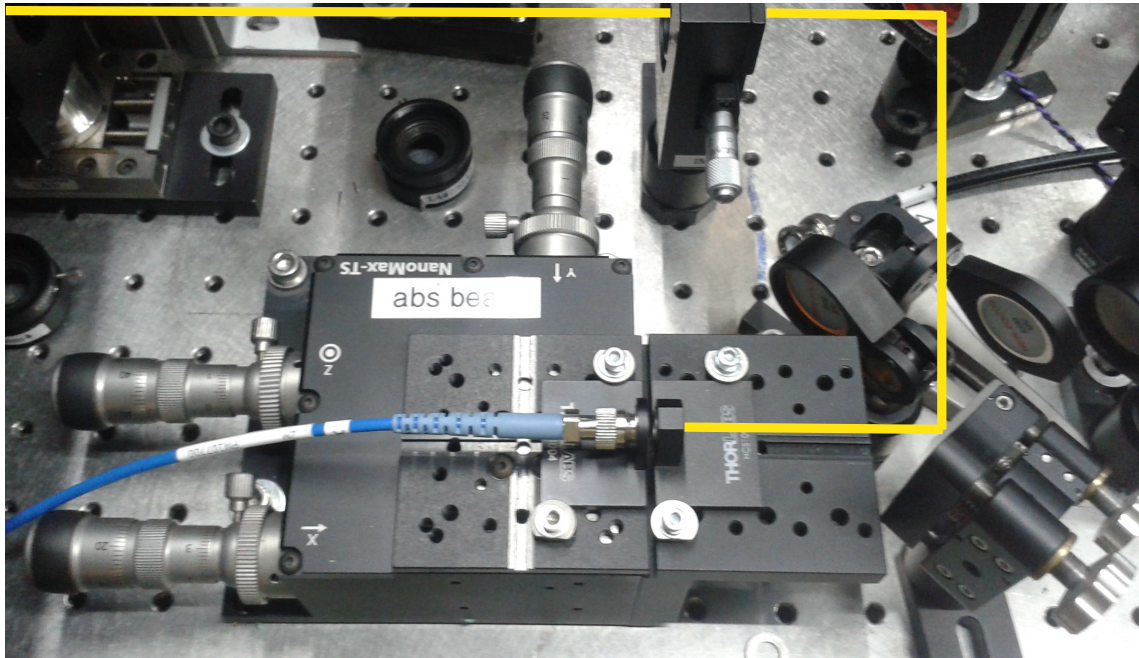


Figure 6.4: The fibre coupling stage used to couple ion light. A Thorlabs(TM) MAX313D 3-axis stage is used to mount the Thorlabs(TM) PM-S350-HP fibre and Thorlabs(TM) C671TME-A lens with focal length of 4.02 mm.

coupling efficiency.

Our design of diffraction rings is aberration free but the average M^2 of 1.45 shows that the beam is aberrated. This is partly because the ion is not a Gaussian emitter and probably partly because of the fabrication defects. Since the measured diffraction efficiency is 33% instead of the predicted 50%, it is likely that the fabrication is not ideal and is contributing to the non-ideal beam quality. To measure the contribution of the fabrication defects the mirror must be tested with a Gaussian beam. If the fabrication defects have a large contribution to this aberration, using fabrication methods that can reproduce the design with a better accuracy can improve the mode quality and the fibre coupling efficiency.

CHAPTER 7

Conclusion

We have demonstrated an integrated, scalable optical interface for efficient free space ion fluorescence collection and single mode fibre coupling. The optic is a diffractive mirror monolithic with the trap electrode. The pitch of the mirrors is $127\ \mu m$ to be compatible with V-groove fibre arrays. The mirror can be placed within tens of micrometers from the ion without distorting the trapping potential. It can cover 13.3% of the total solid angle around the ion and collect 5.8(8)% of the ion fluorescence in free space. The efficiency is higher than the maximum efficiency reported for the conventional bulk optics, other integrated methods [59], and multi mode fibre methods [58]. The small size and high collection efficiency make them an ideal platform for implementation of scalable quantum computing and communication.

We measured 4.1(6)% of the total ion light single mode fibre coupling efficiency which is nearly three times better than the coupling efficiency of the conventional optics [68]. This can improve the speed of remote quantum entanglement and efficiency of the quantum repeaters by almost nine times. This can also be used in realisation of the modular quantum computing proposal [40], since the proposal uses remote entanglement.

We developed a single photon generation protocol based on optical pumping with measured $g^{(2)}$ of 0.12(2). We used the protocol in measurement of the collection efficiency of the diffractive mirrors. This protocol can be used as a single photon source for quantum networking applications and for remote entanglement of the ions.

To demonstrate the mode quality of the light collected by the diffractive mirrors, we captured a near diffraction limited image of the ion with FWHM diameter of $338.0(7)\ nm \times 268.0(6)\ nm$. The diffraction limited size for our NAs are $336\ nm \times 257\ nm$ and the image deviates from this ideal by 0.6% and 4% respectively.

7.1 Future Work

There are several options to improve the collection efficiency of the mirrors in future fabrications. One is to increase the width of the mirror either by extending the design to the surrounding electrodes or implementing it in a different trap with a wider middle electrode.

Another option is to use an alternative fabrication method such as nano-imprinting [74] that has a better accuracy compared to electron beam lithography. The new method can manufacture features that are closer to our design, therefore have a diffraction efficiency and mode quality closer to the theoretical prediction. With the more accurate methods, it is also possible to use more steps in fabricating mirror features and improve the diffraction efficiency even further. Using more complicated multilayer diffractive mirrors is also an option that has been shown to have 99% diffraction efficiency [90].

There are uninvestigated optics on the chip including a self-imager, a laser addresser and a cross imager. The self-imager focuses the ion light back to the ion itself. This is a half cavity and quasi-cavity effects such as the effect of a cavity on transition lifetime can be investigated on this mirror. The laser addresser is another diffractive mirror that can be used to focus the laser light, coming in normal to the chip's surface, on an ion at a specific position. As opposed to laser addressing parallel to the chip surface, the normal addressing is area efficient and can increase the ion density for scaling up the number of qubits. The last optic is a cross-imager that focuses the light from two ions onto each other. Ion interactions mediated by photons can be investigated by this mirror.

The generation rate of the single photon generation protocol can be improved by optimising the time length and delays for different steps. If after optimising, step times close to 25 ns AOM switching time is needed, faster switching AOMs must be used. Since all the lasers use the same AOM and have the same control cable length, the lag time is the same for them and does not create a problem. However the delay time between turning on a laser and detecting the resulting photons is crucial to determine the detection time and must be measured accurately. The improved protocol can be used as a photon source for many applications such as quantum communication.

Two projects have already been started to use the diffractive mirrors for quantum computing and communication applications.

The first project is using parametric down conversion in $LiNbO_3$ non-linear crystals in a planar waveguide circuit to change the frequency of emitted single photons from UV to the telecom frequencies which has lower losses in fibre. Interfacing this converter with the Integrated Diffractive Mirror chip will offer a scalable quantum light source for long rang quantum communications. This is part of a more extensive project to use planar waveguide circuits together with integrated diffractive mirrors to implement parallel optical operations on the ion light [8] (see Fig. 7.1).

The second project is to use one diffractive mirror as both input and output port to implement fast quantum-logic gates with an ultrafast, high repetition rate, fibre-based laser that has been built in our group [91]. A polarising beam splitter is used to send laser light with vertical polarisation to the diffractive mirror and branch out the collected photons with horizontal polarisation. This provides both high laser delivering efficiency and ion light collection efficiency. The goal is to demonstrate a fast phase gate with the

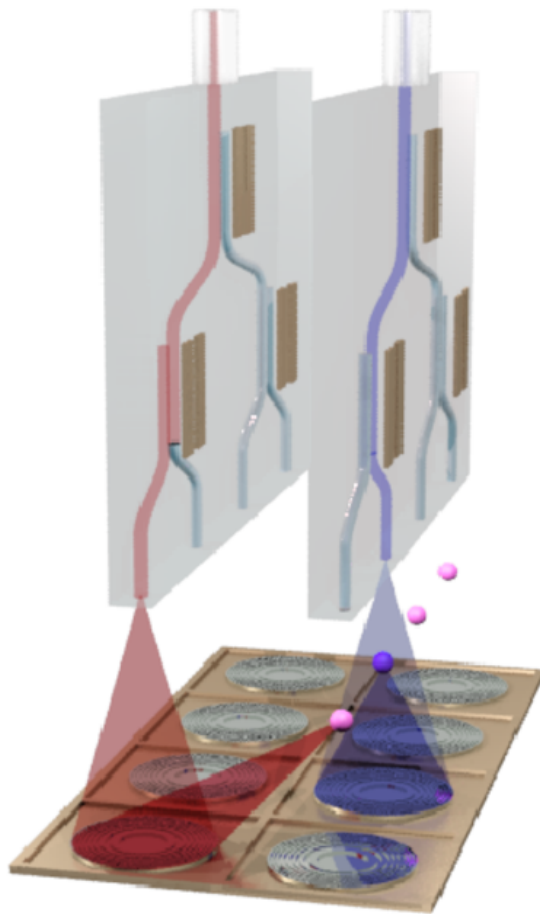


Figure 7.1: A schematic of parallel integrated optics architecture. One array of planar waveguide circuits are used to deliver excitation light to the ions and the other array collects the fluorescence. Mode matching is achieved by the design of the integrated diffractive mirrors. (image from [8])

trapped ions.

APPENDIX A

Gaussian overlap calculation

In calculation of the coupling efficiency of an ideal Gaussian beam into a single mode fibre, when the position and angle of the light is aligned to the fibre, only the mode sizes of the fibre and the light play a role. The coupling efficiency in this case is the Gaussian overlap of the amplitude of the electric field of the two modes.

For a Gaussian beam the lateral profile of the amplitude of the electric field along the x axis has the form[84]:

$$E_1(x) = C_1 e^{-(\frac{x}{w_1})^2} \quad (\text{A.1})$$

where C_1 is a constant that does not depend on x . If we have a second beam with different size:

$$E_2(x) = C_2 e^{-(\frac{x}{w_2})^2} \quad (\text{A.2})$$

the overlap integral of the two beam is:

$$O = A \int_{-\infty}^{+\infty} e^{-(\frac{x}{w_1})^2} e^{-(\frac{x}{w_2})^2} dx \quad (\text{A.3})$$

where A is a normalisation factor that contain C_1 and C_2 . The value of A is to be determined with applying the condition that the overlap is 1 when the two functions are the same, *i.e.* $w_1 = w_2$. With rearranging we have:

$$O = A \int_{-\infty}^{+\infty} e^{-(\frac{w_1^2 + w_2^2}{w_1^2 w_2^2})x^2} dx \quad (\text{A.4})$$

since:

$$\int_{-\infty}^{+\infty} e^{-ax^2} dx = \sqrt{\pi} \frac{1}{\sqrt{a}} \quad (\text{A.5})$$

we have:

$$O = A \sqrt{\pi} \sqrt{\frac{w_1^2 w_2^2}{w_1^2 + w_2^2}} \quad (\text{A.6})$$

with the condition that O must become 1 both when we replace w_1 with w_2 or w_2 with w_1 we have:

$$A = \frac{2}{\sqrt{\pi} \sqrt{w_1^2 + w_2^2}} \quad (\text{A.7})$$

therefore:

$$O = \frac{2}{\sqrt{\pi} \sqrt{w_1^2 + w_2^2}} \sqrt{\pi} \sqrt{\frac{w_1^2 w_2^2}{w_1^2 + w_2^2}} \quad (\text{A.8})$$

$$O = \frac{2w_2 w_1}{w_2^2 + w_1^2} \quad (\text{A.9})$$

If $1/e^2$ radius of the fibre mode is w_{fibre} and the $1/e^2$ radius of the beam along the x axis is w_x , from equation A.9, the value of the overlap integral for the x axis is:

$$O_x = \frac{2w_{fibre} w_x}{w_x^2 + w_{fibre}^2} \quad (\text{A.10})$$

and similarly for the y axis:

$$O_y = \frac{2w_{fibre} w_y}{w_y^2 + w_{fibre}^2} \quad (\text{A.11})$$

and the total coupling efficiency is:

$$\eta_{size} = O_x \times O_y = \frac{4w_{fibre}^2 w_x w_y}{(w_x^2 + w_{fibre}^2)(w_y^2 + w_{fibre}^2)} \quad (\text{A.12})$$

APPENDIX B

Ion Size MATLAB Routine

This Matlab program gets an ion image in ASC format, finds the ion position, cuts the image around the ion and fits a 2D Gaussian function to the image to measure the size of the image.

```
z1=importdata ('C:\Users\Moji\Desktop\All\Reports\Paper\ion
    profile\ion_data\2015-12-04\ion4.asc'); %imports data from
    XYasci export file from the camera
xs=(1:1:512);
ys=(1:1:512);
Mag=1;

z2 = z1(1:512,2:513); %removes the first columns because it is
    the index column
M = max(max(z2));
[MMz,MMzI] = max(z2); % finds maximum number in z2 (ion position)
[Mz,Iy] = max(MMz); %finds y index for maximum value
Ix=MMzI(Iy); %finds x index for maximum value

RadiusOfInterest = 15; % the radius around the ion that you are
    interested in
zz = z2(Ix-RadiusOfInterest:Ix+RadiusOfInterest,Iy-
    RadiusOfInterest:Iy+RadiusOfInterest); %picks only the data
    around the ion within the radius of interest

x = xs(Ix-RadiusOfInterest:Ix+RadiusOfInterest); %picks x
    indexes within the radius of interest
y = ys(Iy-RadiusOfInterest:Iy+RadiusOfInterest); %picks y
    indexes within the radius of interest
```

```

[xx ,yy]=meshgrid(x ,y) ;
%surf(x ,y' ,zz) ; %plot

xr = reshape( xx.' ,1 ,numel(xx)) ;
yr = reshape( yy.' ,1 ,numel(yy)) ;
zr = reshape( zz.' ,1 ,numel(zz)) ;

%surf(x ,y ,zz) ;

s =fitoptions('Method' , 'NonlinearLeastSquares' , 'Startpoint
' ,[0 ,0 ,0 ,0 ,0] , 'Lower' ,[1 ,1 ,1 ,1 ,1] , 'Upper
' ,[20000 ,512 ,512 ,512 ,512] , 'TolFun' ,1E-10) ;
myfittype = fittype('a*exp(-(y-y0)^2/wy^2-(x-x0)^2/wx^2)' ,
'dependent' ,{ 'zn' } , 'independent' ,{ 'x' , 'y' } , 'coefficients' ,{ 'a
' , 'y0' , 'wy' , 'x0' , 'wx' } , 'options' ,s) ;

[xData , yData , zData] = prepareSurfaceData(xr ,yr ,zr) ;

myfit = fit([xData ,yData] ,zData ,myfittype)
%cftool([xData ,yData] ,zData)
plot(myfit ,[xData ,yData] ,zData)
MyCoeffs = coeffvalues(myfit) ;
wy = MyCoeffs(3)*0.86*13*2/Mag %FWHM diameter um
wx = MyCoeffs(5)*0.86*13*2/Mag %FWHM diameter um

```

APPENDIX C

Calculating M^2 MATLAB Routine

This program measures the M^2 of the beam by receiving at least 5 images of the ion around the focus.

```
%[wx1,wxerr1,wy1,wyerr1] = ionsize_func_m2( 'C:\ Users\Moji\
Desktop\All\Reports\Paper\ion profile\ion_data\2015-12-04\
ion0.asc') ;
%[wx2,wxerr2,wy2,wyerr2] = ionsize_func_m2( 'C:\ Users\Moji\
Desktop\All\Reports\Paper\ion profile\ion_data\2015-12-04\
ion1.asc') ;
%[wx3,wxerr3,wy3,wyerr3] = ionsize_func_m2( 'C:\ Users\Moji\
Desktop\All\Reports\Paper\ion profile\ion_data\2015-12-04\
ion2.asc') ;
%[wx4,wxerr4,wy4,wyerr4] = ionsize_func_m2( 'C:\ Users\Moji\
Desktop\All\Reports\Paper\ion profile\ion_data\2015-12-04\
ion3.asc') ;
%[wx5,wxerr5,wy5,wyerr5] = ionsize_func_m2( 'C:\ Users\Moji\
Desktop\All\Reports\Paper\ion profile\ion_data\2015-12-04\
ion4.asc') ;

%[wx1,wy1,x1,y1,x01,y01,I1] = image_analysis_mirko_func( 'C:\ \
Users\Moji\Desktop\All\Reports\Paper\ion profile\ion_data
\2015-11-04 4th coll\ion0.asc') ;
%[wx2,wy2,x2,y2,x02,y02,I2] = image_analysis_mirko_func( 'C:\ \
Users\Moji\Desktop\All\Reports\Paper\ion profile\ion_data
\2015-11-04 4th coll\ion1.asc') ;
%[wx3,wy3,x3,y3,x03,y03,I3] = image_analysis_mirko_func( 'C:\ \
Users\Moji\Desktop\All\Reports\Paper\ion profile\ion_data
\2015-11-04 4th coll\ion2.asc') ;
```

```

%[wx4 ,wy4 ,x4 ,y4 ,x04 ,y04 ,I4 ] = image_analysis_mirko_func( 'C:\\
Users\Moji\Desktop\All\Reports\Paper\ion profile\ion_data
\2015-11-04 4th coll\ion3.asc') ;
%[wx5 ,wy5 ,x5 ,y5 ,x05 ,y05 ,I5 ] = image_analysis_mirko_func( 'C:\\
Users\Moji\Desktop\All\Reports\Paper\ion profile\ion_data
\2015-11-04 4th coll\ion4.asc') ;

wx(1) = 52.8384E-6; %wx1;
wx(2) = 41.9591E-6; %wx2;
wx(3) = 34.0293E-6; %wx3;
wx(4) = 26.4131E-6; %wx4;
wx(5) = 19.1023E-6; %wx5;
wx(6) = 27.9591E-6; %wx6;
%wx(7) = 43.6476E-6; %wx7;

wy(1) = 43.7782E-6; %wy1;
wy(2) = 35.3363E-6; %wy2;
wy(3) = 29.011E-6; %wy3;
wy(4) = 27.761E-6; %wy4;
wy(5) = 27.3803E-6; %wy5;
wy(6) = 36.0794E-6; %wy6;
%wy(7) = 66.0239E-6; %wy7;

z(1) = 14E-3;
z(2) = 16E-3;
z(3) = 18E-3;
z(4) = 20E-3;
z(5) = 22E-3;
z(6) = 24E-3;

%[wx1 ,wy1 ,x1 ,y1 ,x01 ,y01 ,I1 ] = image_analysis('ion data
\2015-06-12 no lens second coll\ion07.asc') ;
%[wx2 ,wy2 ,x2 ,y2 ,x02 ,y02 ,I2 ] = image_analysis('ion data
\2015-06-12 no lens second coll\ion10.asc') ;
%[wx3 ,wy3 ,x3 ,y3 ,x03 ,y03 ,I3 ] = image_analysis('ion data
\2015-06-12 no lens second coll\ion14.asc') ;

```

```

%[wx4 ,wy4 ,x4 ,y4 ,x04 ,y04 ,I4] = image_analysis( 'ion data
\2015-06-12 no lens second coll\ion18.asc' );
%[wx5 ,wy5 ,x5 ,y5 ,x05 ,y05 ,I5] = image_analysis( 'ion data
\2015-06-12 no lens second coll\ion22.asc' );
%z(1) = 07E-3;
%z(2) = 10E-3;
%z(3) = 14E-3;
%z(4) = 18E-3;
%z(5) = 22E-3;

%wx(1)=39E-6*sqrt(1+((z(1)-20E-3)*370E-9*1.5/3.14/39E-6^2)^2);
%wx(2)=39E-6*sqrt(1+((z(2)-20E-3)*370E-9*1.5/3.14/39E-6^2)^2);
%wx(3)=39E-6*sqrt(1+((z(3)-20E-3)*370E-9*1.5/3.14/39E-6^2)^2);
%wx(4)=39E-6*sqrt(1+((z(4)-20E-3)*370E-9*1.5/3.14/39E-6^2)^2);
%wx(5)=39E-6*sqrt(1+((z(5)-20E-3)*370E-9*1.5/3.14/39E-6^2)^2);

%plot(z,wy)

s = fitoptions( 'Method' , 'NonlinearLeastSquares' , 'Startpoint
',[2 ,70E-6,15E-3] , 'Lower' ,[1 ,20E-6 ,0] , 'Upper' ,[5 ,100E-6,20E
-3] , 'TolFun' ,1E-10 , 'MaxFunEval' ,60000 , 'MaxIter' ,40000 );
myfittype = fittype( 'w0*sqrt(1+((z-z0)*370E-9*m2/3.14/w0^2)^2)
', 'dependent' ,{ 'w' } , 'independent' ,{ 'z' } , 'coefficients' ,{ 'm2
', 'w0' , 'z0' } , 'options' ,s );

%cftool(z',wx')
myfitx = fit( z' ,wx' ,myfittype );
hold all
p1 = plot( myfitx ,z ,wx,'^-');
MyCoeffsx = coeffvalues( myfitx );

```

```

m2x=MyCoeffsx(1);
w0x=MyCoeffsx(2);
z0x=MyCoeffsx(3);

m2xstr=num2str(m2x);
w0xstr=num2str(w0x); %FWHM
z0xstr=num2str(z0x);
tstr=[{'M{^2x} = ',m2xstr,' | {1/e^2} Radius (\{\um\}) = ',,
      w0xstr}];

tx=z(3);
ty=(3*wx(3)+wy(3))/4;

text(tx,ty,tstr,'HorizontalAlignment','center');

myfity = fit(z',wy',myfittype);

p2 = plot(myfity,'blue',z,wy,'b-o');

%legend([xfitplot,yfitplot],'ion image x waist','ion image y
%waist');

MyCoeffsy = coeffvalues(myfity);
m2y=MyCoeffsy(1);
w0y=MyCoeffsy(2);
z0y=MyCoeffsy(3);

m2ystr=num2str(m2y);
w0ystr=num2str(w0y); %
z0ystr=num2str(z0y);
tstr=[{'M{^2y} = ',m2ystr,' | {1/e^2} Radius (\{\um\}) = ',,
      w0ystr}];
```

```
tx=z(3)*1.1;  
ty=(wx(3)+3*wy(3))/3;  
  
text(tx,ty,tstr,'HorizontalAlignment','center');  
  
 xlabel('z(m)');  
 ylabel('w(m)');
```

APPENDIX D

Gaussian Beam Propagation Simulation MATLAB Routine

This Matlab routine receives the optical setup after the diffractive mirror as input and simulates the Gaussian beam propagation.

```
clear all
clc
close all
lambda=370E-9; % wavelength m
dd=1E-5; %steps for plotting in m
rmy=40E-6; %mirror size y m
rmx=63.5E-6; %mirror size x m

h=59.6E-6; %ion distance to mirror m

%Add all the lenses and free space after those to the list and
%it will automatically will be added to the calculation

f(1)=59.6E-6; %mirror focal length m
d(1)=60E-3; %distance between mirror and 60mm lens

f(2)=60E-3; %60mm lens focal length m
d(2)=255E-3; %distance between 60mm and 200mm lens in m

%%%
%bottom setup
f(3)=200E-3; %200 mm lens focal length m
d(3)=422E-3 ; %distance between 200mm and 250mm lens in m
```

124 APPENDIX D. GAUSSIAN BEAM PROPAGATION SIMULATION MATLAB ROUTINE

```
f(4)=250E-3; % 250mm lens focal length in m  
d(4)=151E-3 ; %camera
```

```
f(5)=75E-3; %500 mm lens focal length m  
d(5)=200E-3; %distance after 75mm lens
```

```
f(6)=125E-3; %focal length m  
d(6)=286E-3; %distance after lens
```

```
f(7)=100E-3; %focal length m  
d(7)=100E-3; %distance after lens
```

```
%f(8)=1000000000E-3; %focal length m  
%d(8)=100E-3; %distance after lens
```

```
%f(9)=1000000E-3; %focal length m  
%d(9)=300E-3; %distance after lens
```

```
%f(6)=4.02E-3; %4 mm lens focal length m  
%d(6)=5E-3; %distance after 4mm lens  
%}
```

```
%{  
%setup top  
f(3)=200E-3; %200 mm lens focal length m  
d(3)=133E-3; %distance between 200mm and 75mm lens in m
```

```
f(4)=100E-3; %75 mm lens focal length m  
d(4)=67E-3; %distance after 75mm lens
```

```
f(5)=50000E-3; %75 mm lens focal length mm  
d(5)=100E-3; %distance after 75mm lens
```

```
%}
```

```

%x calculation
%Before mirror (assuming it is spherical centered at ion with
the size of mirror)
NAx=rmx/sqrt(rmx^2+h^2);
wix=0.43*lambda/NAx;
qxbinv=complex(0,-lambda/pi/wix^2);
qxb=1/qxbinv;
qx = qxb+h;

NAy=rmy/sqrt(rmy^2+h^2);
wiy=0.43*lambda/NAy;
qybinv=complex(0,-lambda/pi/wiy^2);
qyb=1/qybinv;
qy = qyb+h;

%loop on all the lenses and free spaces
for i = 1:size(f,2)

%lens x
qx(size(qx,2))=qlens(qx(size(qx,2)),f(i));
%free space x
qx = cat(2, qx, qfree(d(i),dd, qx(size(qx,2))) );
qy(size(qy,2))=qlens(qy(size(qy,2)),f(i));
%free space y
qy = cat(2, qy, qfree(d(i),dd, qy(size(qy,2))) );
end

%plot

%get sizez and radiuses in diffrent positions x
for i = 1:size(qx,2)
[rrx(i),wwx(i)] = rw(qx(i),lambda);
end

```

```
%get sizez and radiuses in diffrent positions y
for i = 1:size(qy,2)
[rry(i),wwy(i)] = rw(qy(i),lambda);
end

%creating positions for plot x
for i = 1:size(qx,2)
zz(i)=(i*dd-dd)*1000;
end

hold all

ylim([-max(wwy)*2500 max(wwy)*2500]);
xlim([-250 max(zz)+200]);
title('All numbers are in mm')
xlabel('z: distance from mirror (mm)');
ylabel('w: beam waist (mm)');

plot(zz,wwx*1000,'b-',zz,-wwx*1000,'b-',zz,wwy*1000,'r-',zz,-wwy
*1000,'r-');

ax = gca;
set(ax,'YTick',[ -1 (-0.5) 0 (0.5) 1]);

text(-100,0,strcat('Diff. Lim. rx(1/e2)=',num2str(round(wix*1E9))
),'nm'), 'color','b', 'rotation',90, 'HorizontalAlignment','
center');

text(-150,0,strcat('Diff. Lim. ry(1/e2)=',num2str(round(wiy*1E9))
),'nm'), 'color','r', 'rotation',90, 'HorizontalAlignment','
center');

text(-200,0,strcat('ion height=',num2str(round(h*1E6)), 'um'), '
color','k', 'rotation',90, 'HorizontalAlignment',' center');

%y finding minimums (focuses) and label positions and sizes and
Reileigh
```

```

% rang

for i = 2:( size(wwy,2)-1)
if (wwy(i)<wwy(i-1) && wwy(i)<wwy(i+1))
    line([zz(i),zz(i)],[wwy(i)*1000,-wwy(i)*1000], 'Color' , 'r
    , 'LineWidth' ,0.5);
text(zz(i)-30,0,strcat('z=',num2str(zz(i)), ' wy=',
num2str((1000*wwy(i))), ' Magy=',num2str((wwy(i)/wiy)
) ), 'rotation' ,90 , 'HorizontalAlignment' , 'center' ,
'color' , 'r');

end
end

% finding minimums (focuses) and label positions and sizes and
Reileigh
% range

for i = 2:( size(wwx,2)-1)
if (wwx(i)<wwx(i-1) && wwx(i)<wwx(i+1))
    line([zz(i),zz(i)],[wwx(i)*1000,-wwx(i)*1000], 'Color' , 'b
    , 'LineWidth' ,0.5);
text(zz(i)+30,0,strcat('z=',num2str(zz(i)), ' wx=',
num2str(1000*wwx(i)) , ' Magx=',num2str((wwx(i)/wix))
), 'rotation' ,90 , 'HorizontalAlignment' , 'center' , 'color
' , 'b');

end
end

%labels lenses focal length and position and beam size at the
lens
l=dd;
wl=max(wwy);%ww(round(1/dd/1000));
for i = 1:( size(f,2))

```

```

text(l*1000,(-wl*1650)*(-1)^i ,strcat('f=',num2str(f(i)
*1000)), 'HorizontalAlignment' , 'center') ;
text(l*1000,(-wl*1800)*(-1)^i ,strcat('z=',num2str((l-dd)
*1000)), 'HorizontalAlignment' , 'center') ;

text(l*1000,(-wl*1950)*(-1)^i ,strcat(' w=',num2str(1000*
wwx(round((l/dd)+5)))), 'color' , 'b') ;
text(l*1000,(-wl*2100)*(-1)^i ,strcat(' zr=',num2str
((1000*imag(qx(round((l/dd)+5))))), 'color' , 'b') ;
text(l*1000,(-wl*2250)*(-1)^i ,strcat(' r=',num2str
((1000*rrx(round((l/dd)+5)))), 'color' , 'b') ;

text(l*1000,(-wl*1950)*(-1)^i ,strcat('w=',num2str(1000*
wwy(round((l/dd)+5))), ' | ') , 'color' , 'r' , ,
'HorizontalAlignment' , 'right') ;
text(l*1000,(-wl*2100)*(-1)^i ,strcat(' zr=',num2str
((1000*imag(qy(round((l/dd)+5))))), 'color' , 'r' , ,
'HorizontalAlignment' , 'right') ;
text(l*1000,(-wl*2250)*(-1)^i ,strcat(' r=',num2str((1000*
rry((round((l/dd)+5)))), ' | ') , 'color' , 'r' , ,
'HorizontalAlignment' , 'right') ;

line([l*1000,l*1000],[1500*wl,-1500*wl] , 'Color' , 'k' , ,
LineWidth' ,0.5)

l=l+d(i);

end

```

APPENDIX E

Coupling Efficiency Estimation MATLAB Routine

This Matlab program estimates the single mode fibre coupling efficiency by calculating mode overlap and deviding it by M^2 .

```
%%%
%real Values
```

```
ASM2= 1.26;           %M2 associated with 4.02mm asphere
IonM2x=1.5446;       %M2 of ion image before asphere in the x
                      direction
IonM2y=1.3605;       %M2 of ion image before asphere in the y
                      direction
IonSizex=24.703*2;    %1/e2 um radius at camera
IonSizey=28.453*2;    %1/e2 um radius at camera
```

```
%}
```

```
%%
%ideal Values
```

```
ASM2= 1;           %M2 associated with 4.02mm asphere
IonM2x=1;           %M2 of ion image before asphere in the x
                      direction
IonM2y=1;           %M2 of ion image before asphere in the y
                      direction
IonSizex=13.69;     %1/e2 um radius at camera
IonSizey=13.69;     %1/e2 um radius at camera
```

```
%}
```

```
M2x=ASM2*IonM2x;      %total M2x after asphere
M2y=ASM2*IonM2y;      %total M2y after asphere

FiberModeR=27.38;    %1/e2 um fiber beam radius at camera
%FiberModeR=sqrt ((M2x+M2y)/2)*FiberModeR;  %1/e2 um fiber beam
radius at camera considering best coupling is when ion beam
is M times bigger than fiber size
%check fresnel losses
for i=-10:10
if i>=1
CurMag=1+i/2;
else
CurMag=1/(1-i/2);
end

magarr(i+11)=CurMag;

ElipEff(i+11)= 4*FiberModeR^2*(IonSizex*CurMag)*(IonSizey*CurMag)
/(FiberModeR^2+(IonSizex*CurMag)^2)/(FiberModeR^2+(IonSizey*
CurMag)^2);

%total coupling efficiency
Mag(i+11)=i/2;
M2Eff(i+11) = 2/(M2x+M2y);
TotEff(i+11)= M2Eff(i+11)*ElipEff(i+11);

end

%plot
X=Mag;
Y=TotEff;

hold on;
```

```

%plot(X,Y, 'b*' );
%bar(X,Y);
strValues = strcat( num2str( round(100*Y(:))/100) );
YY=Y-0.1;
%text(X,YY,strValues , ' rotation ',90);
xlabel(' Magnification ') ; % x-axis label
ylabel(' Coupling Efficiency ') ; % y-axis label

Z=ElipEff;
%plot(X,Z, 'ko' );

strValues = strcat( num2str( round(Z(:,2))) );
%text(X,Z,strValues , ' rotation ',90);

%plot(X,M2Eff , 'r^' );

P=[Y ;Z ; M2Eff ];
PT=transpose(P);
bar(PT);
legend(' Total Coupling Efficiency ', ' Size Matching Efficiency ', ,
      ' M2 Efficiency ');
%set(gca , 'XTick' , 1:4 , 'XTickLabel' , X);

ax = gca;
set(gca , 'XTick' ,[1:size(X,2)])
ax.XTickLabel = { '1/6' ' ' '1/5' ' ' '1/4' ' ' '1/3' ' ' '1/2' ' '
                 '1' ' ' '2' ' ' '3' ' ' '4' ' ' '5' ' ' '6' };
%axis([-5 5 -0.2 1.2])
%XTick = { '1/6' '1/5.5' '1/5' '1/4.5' '1/4' '1/3.5' '1/3'
%           '1/2.5' '1/2' '1/1.5' '1' '1.5' '2' '2.5' '3' '3.5' '4' '4.5'
%           '5' '5.5' '6' };


```

References

- [1] F. Splatt *et al.*, *Deterministic reordering of $^{40}\text{Ca}^+$ ions in a linear segmented Paul trap*, New J. Phys. **11**, 103008 (2009).
- [2] D. Kielpinski, *Entanglement and Decoherence in a Trapped-Ion Quantum Register*, PhD thesis, University of Colorado, 2001.
- [3] J. Chiaverini *et al.*, *Surface-Electrode Architecture for Ion-Trap Quantum Information Processing*, arXiv **quant-ph**, 0501147 (2005).
- [4] G. T. R. I. Q. S. Group, *GTRI Microwave Ion traps for QIP applications*.
- [5] A.-M. Martensson-Pendrill and D. S. G. P. Hannaford, *Isotope shifts and hyperfine structure in the 369.4-nm $6s-6p_{1/2}$ resonance line of single) ionized ytterbium*, Phys. Rev. A **49**, 3351 (1994).
- [6] H. M. Meyer, M. Steiner, L. Ratschbacher, C. Zipkes, and M. K02hl, *Laser spectroscopy and cooling of Yb^+ ions on a deep-UV transition*, Phys Rev. A **85**, 012502 (2012).
- [7] V. R. Blums, *Ion Fluorescence Collection And Diffraction Limited Imaging From A Microfabricated Ion Trap With Integrated Diffractive Mirrors*, Master's thesis, Griffith University, 2012.
- [8] D. Kielpinski, C. Volin, E. W. Streed, R. Blatt, and M. Lobino, *Integrated optics architecture for trapped-ion quantum information processing*, Quantum Inf. Process. **1**, 1 (2015).
- [9] J. P. Dowling and G. J. Milburn, *Quantum Technology: The Second Quantum Revolution*, Arxive , 0206091 (2002).
- [10] T. H. Maiman, *Stimulated Optical Emission in Fluorescent Solids. I. Theoretical Considerations*, Pys. Rev. Lett. **123**, 1145 (1961).
- [11] R. P. Feynman, *Simulating Physics with Computers*, Int. J. Theor. Phys. **21**, 467 (1982).

- [12] M. A. Nielsen and I. L. Chuang, *Atomic Physics* (Cambridge University Press, 2000).
- [13] *Algorithms for quantum computation: discrete logarithms and factoring*, Santa Fe, NM, USA, 1994, IEEE.
- [14] D. Bes, *Quantum Mechanics: A Modern and Concise Introductory Course* (Springer, 2012).
- [15] C. Bennett and G. Brassard, *Quantum Cryptography: Public Key Distribution and Coin Tossing*, Proc Intl Conf Comp Sys Sig Proc,(IEEE Bangalore India) , 175 (1984).
- [16] P. Kok *et al.*, *Linear optical quantum computing with photonic qubits*, REVIEWS OF MODERN PHYSICS **79**, 135 (2007).
- [17] D. M. H and M. J. M, *Implementing qubits with superconducting integrated circuits*, Quantum Inform. Process **3**, 163C203 (2007).
- [18] D. Loss and D. P. DiVincenzo, *Quantum computation with quantum dots*, Quantum Inform. Process **57**, 120 (1998).
- [19] J. L. O'Brien, G. J. Pryde1, A. G. White1, T. C. Ralph1, and D. Branning, *Demonstration of an all-optical quantum controlled-NOT gate*, Nature **426**, 264 (2003).
- [20] D. P. DiVincenzo, *The Physical Implementation of Quantum Computation*, Fortschritte der Physik **48**, 771 (2000).
- [21] T. P. Harty *et al.*, *High-Fidelity Preparation, Gates, Memory, and Readout of a Trapped-Ion Quantum Bit*, Phys. Rev. Lett. **113**, 220501 (2014).
- [22] R. Blatt, H. H. C. F. Roos, C. Becher, and F. Schmidt-Kaler, *Ion Trap Quantum Computing with Ca+ Ions*, Quant. Inf. Proc. **3**, 1 (2004).
- [23] B. E. King *et al.*, *Cooling the Collective Motion of Trapped Ions to Initialize a Quantum Register*, Phys. Rev. Lett. **81**, 1528 (1998).
- [24] C. Roos *et al.*, *Quantum State Engineering on an Optical Transition and Decoherence in a Paul Trap*, Phys. Rev. Lett. **83**, 4713 (1998).
- [25] C. Monroe, D. M. Meekhof, B. E. King, W. M. Itano, and D. J. Wineland, *Demonstration of a Fundamental Quantum Logic Gate*, Phys. Rev. Lett. **75**, 4714 (1995).
- [26] M. A. Rowe *et al.*, *Experimental violation of a Bell's inequality with efficient detection*, Nature **409**, 791 (2000).

- [27] K. R. Brown *et al.*, *Single-qubit-gate error below 10^{-4} in a trapped ion*, Phys. Rev. A **84**, 030303 (2011).
- [28] J. Benhelm, G. Kirchmair, C. F. Roos, and R. Blatt, *Towards fault-tolerant quantum computing with trapped ions*, **174**, 1 (2008).
- [29] J. Chiaverini *et al.*, *Realization of quantum error correction*, Nature **432**, 602 (2004).
- [30] J. F. Goodwin *et al.*, *Trapped-ion quantum error-correcting protocols using only global operations*, Phys. Rev. A **92**, 032314 (2015).
- [31] S. Debnath *et al.*, *Demonstration of a programmable quantum computer module*, arXiv (2016).
- [32] T. Monz, I. L. Chuang, and R. Blatt, *Realization of a scalable Shor algorithm*, Science **351**, 1068 (2016).
- [33] K.-A. Brickman *et al.*, *Implementation of Grover's quantum search algorithm in a scalable system*, Phys. Rev. A **72**, 050306(R) (2005).
- [34] D. L. Moehring *et al.*, *Entanglement of single-atom quantum bits at a distance*, Nature **449**, 68 (2007).
- [35] J. Cirac and P. Zoller, *Quantum Computations with Cold Trapped Ions*, Pys. Rev. Lett. **74**, 4091 (1994).
- [36] A. S03rensen and K. M03lmer, *Entanglement and quantum computation with ions in thermal motion*, Phys. Rev. A **62**, 022311 (2000).
- [37] D. J. Wineland *et al.*, *Experimental Issues in Coherent Quantum-State Manipulation of Trapped Atomic Ions*, J. Res. NIST. **103**, 259 (1998).
- [38] R. J. Hughes, D. F. V. James, E. H. Knill, R. Laflamme, and A. G. Petschek, *Decoherence Bounds on Quantum Computation with Trapped Ions*, Pys. Rev. Lett. **77**, 3240 (1996).
- [39] T. Monz *et al.*, *14-Qubit Entanglement: Creation and Coherence*, Phys. Rev. Lett. **106**, 13050 (2011).
- [40] C. Monroe *et al.*, *Large-scale modular quantum-computer architecture with atomic memory and photonic interconnects*, Phys. Rev. A **89**, 022317 (2014).
- [41] L.-M. Duan and C. Monroe, *Colloquium: Quantum networks with trapped ions*, Rev. Mod. Phys. **82**, 1209 (2010).

- [42] D. Kielpinski, C. Monroe, and D. Wineland, *Architecture for a large-scale ion-trap quantum computer*, Nature **417**, 709 (2002).
- [43] S. Seidelin *et al.*, *Microfabricated Surface-Electrode Ion Trap for Scalable Quantum Information Processing*, Phys. Rev. Lett. **96**, 253003 (2006).
- [44] J. M. Amini *et al.*, *Towards scalable ion traps for quantum information processing*, New J. Phys. **12**, 033031 (2010).
- [45] W. K. Hensinger *et al.*, *T-junction ion trap array for two-dimensional ion shuttling, storage, and manipulation*, 60Appl. Phys. Lett. **88**, 034101 (2006).
- [46] D. Hucul, M. Yeo, W. Hensinger, J. Rabchuk, and S. O. andsa C. Monroe, *On the transport of atomic ions in linear and multidimensinal ion trap arrays*, Quantum Inf. Comput. **8**, 501 (2008).
- [47] R. B. Blakestad *et al.*, *High-Fidelity Transport of Trapped-Ion Qubits through an X-Junction Trap Array*, Phys. Rev. Lett. **102**, 153002 (2009).
- [48] H. C. Nägerl *et al.*, *Laser addressing of individual ions in a linear ion trap*, Phys. Rev. A **60**, 145 (1999).
- [49] S. Crain, E. Mount, S. Baek, and J. Kim, *Individual addressing of trapped $^{171}\text{Yb}^+$ ion qubits using a microelectromechanical systems-based beam steering system*, APPLIED PHYSICS LETTERS **105**, 181115 (2014).
- [50] K. K. Mehta *et al.*, *Integrated optical addressing of an ion qubit*, arXiv (2015).
- [51] S. Olmschenk *et al.*, *Quantum Teleportation Between Distant Matter Qubits*, Science **323**, 486 (2009).
- [52] G. R. Guthöhrlein, M. Keller, K. Hayasaka, W. Lange, and H. Walther, *A single ion as a nanoscopic probe of an optical field*, Nature **414**, 49 (2001).
- [53] A. B. Mundt *et al.*, *Coupling a Single Atomic Quantum Bit to a High Finesse Optical Cavity*, Phys. Rev. Lett. **89**, 103001 (2002).
- [54] D. R. Leibrandt, J. Labaziewicz, V. Vuletic, and I. L. Chuang, *Cavity Sideband Cooling of a Single Trapped Ion*, Phys. Rev. Lett. **103**, 103001 (2009).
- [55] G. Shu, N. Kurz, M. R. Dietrich, and B. B. Blinov, *Efficient fluorescence collection from trapped ions with an integrated spherical mirror*, Phys Rev A **81**, 042321 (2010).
- [56] R. Maiwald *et al.*, *Stylus ion trap for enhanced access and sensing*, Nature Physics **5**, 551 (2009).

- [57] J. T. Merrill *et al.*, *Demonstration of integrated microscale optics in surface-electrode ion traps*, New J Phys **13**, 103005 (2011).
- [58] A. P. Vandevender, Y. Colombe, J. Amini, D. Leibfried, and D. J. Wineland, *Efficient Fiber Optic Detection of Trapped Ion Fluorescence*, Phys. Rev. Lett. **105**, 023001 (2010).
- [59] C. R. Clark *et al.*, *Characterization of Fluorescence Collection Optics Integrated with a Microfabricated Surface Electrode Ion Trap*, Phys. Rev. Applied **1**, 024004 (2014).
- [60] A. Wilson *et al.*, *Fiber-coupled single ion as an efficient quantum light source*, Arxive **1**, 1101.5877 (2011).
- [61] E. W. Streed, B. G. Norton, A. Jechow, T. J. Weinhold, and D. Kielpinski, *Imaging of Trapped Ions with a Microfabricated Optic for Quantum Information Processing*, Phys. Rev. Lett. **106**, 010502 (2011).
- [62] A. Jechow, E. W. Streed, B. G. Norton, M. J. Petrasius, and D. Kielpinski, *Wavelength-scale imaging of trapped ions using a phase Fresnel lens*, Opt. Lett. **36**, 1371 (2011).
- [63] E. W. Streed, A. Jechow, B. G. Norton, and D. Kielpinski, *Absorption imaging of a single atoms*, Nat. Commun. **3**, 933 (2012).
- [64] P. M. nad S. Olmschenk, D. Hayes, D. N. Matsukevich, L.-M. Duan, and C. Monroe, *Heralded Quantum Gate between Remote Quantum Memories*, Phys. Rev. Lett. **109**, 250502 (2009).
- [65] D. N. Matsukevich, P. Maunz, D. L. Moehring, S. Olmschenk, and C. Monroe, *Bell Inequality Violation with Two Remote Atomic Qubits*, Phys. Rev. Lett. **100**, 150404 (2004).
- [66] S. Gerber *et al.*, *Quantum interference from remotely trapped ions*, New Journal of Physics **11**, 013032 (2009).
- [67] B. B. Blinov, D. L. Moehring, L.-M. Duan, and C. Monroe, *Observation of entanglement between a single trapped atom and a single photon*, Nature **428**, 153 (2004).
- [68] D. Hucul *et al.*, *Modular entanglement of atomic qubits using photons and phonons.*, Nature **11**, 37 (2015).
- [69] L. S. Brown and G. Gabrielse, *Geonium theory: Physics of a single electron or ion in a Penning trap*, REVIEWS OF MODERN PHYSICS **58**, 233 (1986).

- [70] L. Deslauriers, *Cooling and Heating of the Quantum Motion of Trapped Cd+ Ions*, PhD thesis, University of Michigan, 2006.
- [71] D. W. Macalpine and R. O. Schildknecht, *Coaxial resonators with helical inner conductor*, Proc. of the IRE **47** (2010).
- [72] T. Shiono, M. Kitagawa, K. Setsune, and T. Mitsuyu, *Reflection micro-Fresnel lenses and their use in an integrated focus sensor*, Appl. Opt. **28**, 3434 (1989).
- [73] A. Kreuter *et al.*, *Spontaneous Emission Lifetime of a Single Trapped Ca+ Ion in a High Finesse Cavity*, Phys. Rev. Lett. **92**, 203002 (2004).
- [74] L. X *et al.*, *Direct imprint of nanostructures in metals using porous anodic alumina stamps*, Nanotechnology **24**, 2553036 (2013).
- [75] H. J. Metcalf and P. van der Straten, *Laser Cooling and Trapping* (Springer, 1999).
- [76] J. B02hlke *et al.*, *Isotopic Compositions of the Elements, 2001*, Journal of Physical and Chemical Reference Data **34**, 57 (2005).
- [77] D. Das, S. Barthwal, A. Banerjee, and V. Natarajan, *Absolute frequency measurements in Yb with 0.08 ppb uncertainty: Isotope shifts and hyperfine structure in the 399-nm 1S0-1P1 line*, Pys. Rev. A **72**, 032506 (2005).
- [78] S. Olmschenk *et al.*, *Manipulation and detection of a trapped Yb+ hyperfine qubit*, Phys. Rev. A **76**, 052314 (2007).
- [79] N. Poli, C. W. Oates, P. Gill, and G. M. Tino, *Optical atomic clocks*, Arxiv , 1401.2378v2 (2014).
- [80] B. G. Norton, E. W. Streed, M. J. Petrasius, A. Jechow, and D. Kielpinski, *Milikelvin Spatial Thermometry of Trapped Ions*, arXiv:1106.1708v1 [quant-ph] (2011).
- [81] M. L. P. Ltd., *External Cavity Diode Laser Model ECD003*.
- [82] P. Kumar *et al.*, *Studies on the Optogalvanic Effect and Isotope-Selective Excitation of Ytterbium in a Hollow Cathode Discharge Lamp Using a Pulsed Dye Laser*, Applied Spectroscopy **67**, 9 1036 (2013).
- [83] P. Meystre and M. Sargent III, *Elements of Quantum Optics* (Springer-Verlag, Berlin, 1990).
- [84] B. E. A. Saleh and M. C. Teich, *Fundamentals of Photonics* (John Wiley and Sons Ltd, 2007).

- [85] ISO, International Organization for Standardization Report No. ISO 11146-2:2005, 2005 (unpublished).
- [86] W. Hanle, *Physik* **30**, 93 (1924).
- [87] A. Optoelectronic, *MQ180-A0.2-266.300 MQ180-A0.2-UV MQ180-A0.25-VIS AO MODULATOR/SHIFTER/PULSE PICKER.*
- [88] M. Fox, *Quantum Optics: An Introduction* (Oxford University Press, 2006).
- [89] J. Vu00kovi04, D. Fattal, C. Santori, G. S. Solomon1, and Y. Yamamoto, *Enhanced single-photon emission from a quantum dot in a micropost microcavity*, *Appl. Phys. Lett.* **82**, 3596 (2003).
- [90] N. Destouches, J. C. P. A. V. Tishchenko, S. Reynaud, and O. Parriaux, *99% efficiency measured in the 1st order of a resonant grating*, *Opt. Express* **13**, 3231 (2005).
- [91] M. I. Hussain *et al.*, *Ultrafast, high repetition rate, ultraviolet, fiber-laser-based source: application towards Yb+ fast quantum-logic*, *Optics Express* **24**, 16638 (2016).